IMPROVING THE PERFORMACE OF PROFILED GRINDING WHEELS WITH A NOVEL SURFACE TEXTURING ROBOT

by

Cameron Forbrigger

Submitted in partial fulfillment of the requirements
for the degree of Master of Applied Science

at

Dalhousie University
Halifax, Nova Scotia
August 2017

Table of Contents

List of Tables

List of Figures

Abstract

This work explores the improvement of a profile grinding process by creating grooves on the surface of a grinding wheel. Grooved grinding wheels have been shown by many authors to reduce the process forces, process temperatures and specific energy of the grooving process, thereby allowing higher grinding productivity. However, the use of grooved grinding wheels has never been explored for profile grinding applications, which differ in several ways from flat grinding processes. The main objectives of this work are to (1) investigate the state-of-the-art of grinding wheel grooving methods; (2) design, build and validate a method to produce helical grooves on profile grinding wheels; and (3) demonstrate the effects of helical grooves on the performance of a profile grinding operation and compare the performance to a conventional profile grinding wheel. An in-depth review of grinding wheel grooving technology literature was conducted. Using information from the literature review, a device capable of grooving grinding wheels was designed, built and validated. This device was found to be capable of producing groove geometries to within an accuracy of ± 10 µm. To achieve the desired accuracy, a novel kinematic error compensation method was developed as a part of the design of the grooving device. The device was then used to groove a profile grinding wheel. A grooved profile grinding process was found to have a 50% lower specific energy than a non-grooved process and significantly lower process forces. Furthermore, the grooved profile grinding wheel was capable of taking a depth of cut four times deeper than a non-grooved profile grinding wheel before process failure occurred. The grooved profile grinding wheel was found to produce a surface roughness approximately 80% larger than the non-grooved profile grinding wheel.

List of Symbols

α_g – Helix angle of a helical groove.

A_o – Total cutting surface area of the grinding wheel.

A_g – Surface area of the wheel removed by grooving.

a_g – Groove depth in the radial direction of the grinding wheel.

b_g – Maximum width of a groove cross-section normal to the groove direction.

b_s – Grinding wheel width.

d_e – Equivalent grinding wheel diameter for cylindrical grinding.

d_s – Grinding wheel diameter.

η_g – Groove factor/intermittent ratio.

F_a – Cutting force component along the grinding wheel spindle axis.

F_n – Cutting force component normal to the grinding wheel.

F_t – Cutting force component tangential to the grinding wheel.

L_g – Lead of a helical groove.

N_g – Number of equally-spaced starts of a helical groove.

$\vec{q}$ – Vector containing the joint values (stage positions) of the grooving device..

r_s – Radial distance from the grinding wheel center to the origin of the local Cartesian coordinate system..

$\vec{r}_t$ – Position of the cutting edge of the single-point tool in cartesian coordinates.

$R_{t,g}$ – Additional workpiece surface roughness introduced by groove texture.

$\hat{v}$ – Unit vector describing the orientation of the vertical grooving device stage.

v_s – Tangential velocity of the grinding wheel.

v_w – Feed rate of the workpiece during grinding.

v_z – Feed rate of the dressing tool during grooving.

$\hat{w}$ – Unit vector describing the orientation of the horizontal grooving device stage.

w_g – Groove width in the circumferential direction of the wheel.

ω_s – Angular velocity of the grinding wheel.

Acknowledgements

I would like to thank the people who made this work possible.

I would like to thank my family, especially my mother and father, for their love and support throughout my life, and their constant encouragement in my academic studies. My entire family is the foundation upon which I have built my life. Words cannot express my thanks for what they have done for me.

Thank you to my supervisors Robert Bauer and Andrew Warkentin for their guidance, patience and constructive criticisms throughout my degree, grinding down the rough edges of my work, so to speak. I have learned so much in my time as their student, and I greatly appreciated their mentorship. They have equipped me with the tools to succeed as I move forwards in my academic career.

Thank you to my committee members, Ya-Jun Pan and Zoheir Farhat, for their time and energy reviewing my thesis and challenging me in my defence.

Thank you to Al-Mokhtar Omran Mohamed for his assistance and advice in the lab and in my work. I really enjoyed our conversations together, and his work served as the starting point of my own.

Thank you to all the lab technicians and support staff in the Dalhousie Mechanical Engineering Department for their time and expertise, especially Kate Hide, Jon MacDonald and Angus MacPherson.

Chapter 1

Introduction

Grinding is an important manufacturing process that allows more precise dimensional tolerances and finer surface finishes, and can machine a wider variety of materials than conventional machining processes. While the basic principles behind abrasive machining have been used for thousands of years, manufacturers continue to innovate and improve the grinding process [1].

1.1 Motivation

In a survey paper describing challenges facing the grinding industry, Oliveira *et al.* [2] note that manufacturers are constantly seeking ways to push their productivity to the limit: higher material removal rates, deeper depths of cut, higher spindle speeds. As a result, some manufacturers are finding their processes are exceeding the limits of their machine tools: poor dimensional tolerances due to static deflections of the machine tool, spindle power requirements exceeding the machine tool capabilities, and inadequate coolant delivery. Furthermore, energy efficiency is becoming an increasing concern for manufacturers [2].

Grooved grinding wheels have been shown by many authors to improve coolant flow and reduce process forces, process temperatures, and specific energies along with a minor increase in workpiece surface roughness [3]. Grooved grinding wheels have the potential to meet the needs of manufacturers striving for higher production rates without needing to purchase larger more expensive machine tools. Many authors have demonstrated the capabilities of grooved grinding wheels for a variety of grinding operations: surface grinding, creep feed grinding, and cylindrical grinding. The most effective groove geometry investigated in the literature is the "circumferential" groove geometry, which is a helical groove with a helix angle between approximately 80° and 90°. The effect of grooves on a profile grinding process have not yet been investigated, as currently no methods of creating grooves on a profile grinding wheel

have been demonstrated. [3] Profile grinding of asymmetrical profiles produces additional axial forces that are not present in other grinding processes, with the potential to cause additional static deflections and reduce workpiece dimensional tolerances [4]. Furthermore, profile grinding can cause temperature concentrations in the workpiece, leading to thermal damage of the workpiece at a lower spindle power than flat grinding processes [4]. Profile grinding operations could stand to benefit greatly from the application of grooved grinding wheels, assuming that the improvements seen in other grinding operations hold true.

1.2 Objectives

The main objectives of this work are to:

- Investigate the state-of-the art of grinding wheel grooving methods.
- Design, build and validate a method to produce helical grooves on profile grinding wheels.
- Demonstrate the effects of helical grooves on the performance of a profile grinding operation and compare the performance to a conventional profile grinding wheel.

1.3 Thesis Outline

The content in this thesis is arranged in the following order. In Chapter 2, the background information regarding the grinding process, grooved grinding wheels and grooving processes is presented. In Chapter 3, an extensive survey of grooved grinding wheel research is presented, along with a comparison of the strengths and weaknesses of several state-of-the-art grooving methods. In Chapter 4, the design, construction and validation of a multi-axis computer-numerical-control (CNC) grinding wheel grooving device is presented. In Chapter 5, the kinematics of the grooving device are described in detail. Finally, in Chapter 6, the performance of a profile grinding wheel grooved by the grooving device is presented and compared to the performance of a non-grooved profile grinding wheel.

Chapter 2

Background

The purpose of this chapter is to provide the reader with the background necessary to understand the work presented in this manuscript. A more detailed analysis of the current trends in the literature of grinding wheel grooving that are not fundamentally necessary to the understanding of the work is presented in Chapter 3.

First a brief overview of the grinding process and the basics of abrasive cutting are presented. Then the structure and composition of grinding wheels and the nature of grinding wheel wear is described. Profile grinding operations are then described and the challenges posed by profile grinding processes are discussed. Next, grooved grinding wheels are defined, along with a formal definition of helical grooves. The geometry and nomenclature of helical grooves is presented followed by descriptions of different methods of producing grooves on a particular type of grinding wheels called "vitrified bond" grinding wheels.

2.1 Grinding

Grinding is an abrasive machining process, in which a wheel of bonded abrasive grits (or grains) removes material from a workpiece. Grinding processes have several advantages over conventional machining processes, such as milling and turning. Grinding processes can produce much finer workpiece surface finishes (lower surface roughness) than conventional machining processes. For example, a milling process can be expected to produce a surface roughness between 1 µm and 6 µm, whereas a grinding process can be expected to produce surface roughness between 0.1 µm and 2 µm. Another advantage of grinding processes is that they can produce very accurate surface tolerances. For example, the Blohm Planomat 408 grinding machine used for the experiments in this work has a positioning resolution of 0.254 µm. Finally, grinding wheels are capable of machining very hard materials, such as ceramics and

aerospace alloys. The disadvantages of grinding processes are that they tend to require significantly more energy per unit volume of material removed (higher specific energy) than conventional machining processes and they tend to generate significant amounts of heat that can lead to workpiece damage [1].

During the grinding process, individual abrasive grits remove a tiny amount of material, with thousands of grits contributing to the overall material removal of the process; however, not all of the grits contribute to the material removal. Grits that make contact with the workpiece can make contact in three different ways: rubbing, ploughing, and cutting. Rubbing grains generate force and heat through frictional contact with the workpiece, but do not remove any material. Ploughing grains penetrate the workpiece, but they only deform the workpiece material instead of removing it. Finally, cutting grains penetrate the workpiece and remove material from the workpiece [1, 5].

There are many different types of grinding processes, including but not limited to surface grinding, cylindrical grinding, and creep-feed grinding. Surface and cylindrical grinding are common grinding processes, characterized by high feed rates (tens of $\mathrm{mm\,s^{-1}}$) and low depths of cut (on the order of micrometers), and are generally used to create the most smooth flat or cylindrical surfaces. Creep-feed grinding is characterized by low feed rates (less than ten $\mathrm{mm\,s^{-1}}$) and high depths of cut (on the order of millimeters) [1].

2.1.1 Grinding Wheels

There are three substances that make up the composition of a grinding wheel: the abrasive grits, the bond material, and the "pores" (air pockets). The relative quantities of these components can change the performance of a grinding wheel, allowing wheels to be designed for different applications by modifying the composition. [1]

The abrasive grits are the part of the grinding wheel that perform the actual cutting. Different materials can be used for the abrasive grits and bond material. The most common materials used for abrasive grits, in order of increasing hardness, are aluminum oxide Al_2O_3, silicon carbide SiC, cubic boron nitride cBN, and diamond. Abrasive grains also come in different sizes, with larger grains intended for higher material removal rates with poorer surface roughness and smaller grains intended for

lower material removal rates with fine surface roughness. [1]

The bond material is what gives the wheel its structure. Without the bond material, the abrasive grits would be a coarse powder that would not hold any particular shape. The bond material comes in many different varieties with differing amounts of strength and temperature resistance. Broadly speaking, the main categories of bond material are vitrified bonds, silicate bonds, rubber bonds, resinoid bonds, shellac bonds, and metallic bonds. [1]

All of the wheel specification information is summarized using the ANSI Standard B74.13–1977 grinding wheel marking system. For example, the grinding wheel used in the experiments in this work is marked with WR–A–60–J–5–V.

- WR – The manufacturer's symbol for the abrasive. In this case, the wheel was manufactured by Radiac Abrasives.
- A – The abrasive material of the wheel. In this case, the abrasive material was aluminum oxide.
- 60 – The grain size, which is a number from 8 to 600 with larger numbers indicating smaller grains. In this case, the grain size was 60, which is at the upper range of a medium grit size.
- J – The wheel grade, which is a letter from A (soft) to Z (hard).
- 5 – The wheel structure, which is a number from 1 to 15. Higher numbers indicate more porosity in the wheel.
- V – The bond type. In this case, a vitrified bond type.

As a grinding wheel is used, it experiences wear. There are three main modes through which wear occurs. The first mode is called "attritious wear", which is the slow dulling of the abrasive grits. Cutting grits can wear until they become dull and flat, which will cause them to start rubbing or ploughing instead of cutting. As attritious wear progresses the grinding process becomes less efficient and the power tends to increase. The second mode is "grain fracture", which is where pieces of the grits break off, exposing new cutting edges. The third mode is "bond fracture", sometimes called "grain pull-out". Bond fracture normally occurs after attritious

wear. Dull grits experience more cutting force than sharp grits, which can cause the bond material holding the grit to break. If a large amount of bond fracture occurs it is referred to as "wheel breakdown", which is generally characterized by a decrease in the cutting power due to the reduction in the number of grits contacting the workpiece [1].

2.1.2 Profile Grinding Processes

Profile grinding is a type of grinding process where a grinding wheel formed to a specific shape imparts that shape to a workpiece by slowly plunge feeding into the workpiece. An example of a profile grinding application is the grinding of gas turbine compressor blade roots. The blades inside of a gas turbine compressor connect to a central rotating hub by a structure called a "root". An example compressor blade is pictured in Figure 2.1. The root starts with a roughly trapezoidal shape and the ridges shown in Figure 2.1 are ground into the workpiece.

A recent area of development in gas turbine blades is creating fine ridges or "riblets" that run along the surface of the blade. The purpose of the riblets is to reduce the drag on the compressor blades by limiting the formation of turbulent flow, thereby

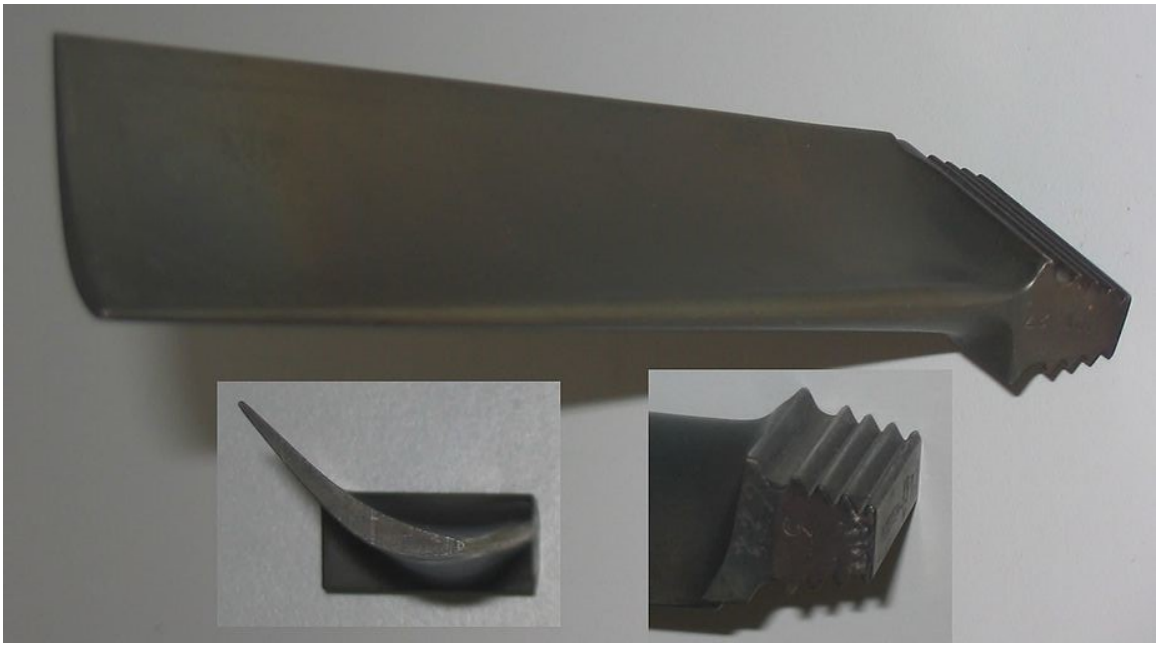

Figure 2.1: An example of a gas turbine compressor blade. The insert on the bottom right shows the turbine root. Image source: Wikimedia Commons [6].

improving the turbine efficiency. The formation of these riblets can be accomplished by profile grinding, as was demonstrated by Denkena *et al.* [7]. Grinding is well-suited to this application because turbine blades are generally made of hard aerospace materials and require precise tolerances [7].

Despite the importance of profile grinding for aerospace and energy applications described above, profile grinding is not as well studied as surface grinding and other flat grinding processes. The temperature distributions in profile grinding tend to be very complex due to the complex shape of the wheel-workpiece interface and temperature concentrations can appear in the corners of the profile. Furthermore, a non-symmetrical profile can produce cutting forces that act along the axis of the grinding wheel, causing static deflection errors and poorer dimensional tolerances. These axial forces are not present for flat grinding [4].

2.2 Grooved Grinding Wheels

Grooved grinding wheels are a subset of a growing field of "textured grinding wheels". Li and Axinte [8] define textured grinding wheels as having "both specially-designed active and passive grinding areas on their geometrically active surface." In other words, sections of the grinding wheel have been modified such that the grinding wheel is not continuously making contact with the workpiece. The term "textured grinding wheel" covers a large variety of wheel types, including some grinding wheels where abrasive grains are individually and manually mounted in patterns on a metal rim. [8]

Grooved grinding wheels are a subset of textured grinding wheels, defined by Forbrigger *et al.* [3] as "a subcategory of macroscopic textured grinding wheels where the pattern can be described by a set of space curves on the wheel surface that define the trajectory of a groove profile." Essentially, a grooved grinding wheel is a wheel with a pattern scribed onto the surface that can be described by a collection of continuous or discontinuous lines. Grooved grinding wheels are most commonly made with aluminum oxide or silicon carbide abrasive material. The most common groove type is a helical groove, although different authors use different names for this type of groove, including spiral groove, circumferential groove, and slotted groove. [3]

Figure 2.2 shows a photograph of the surfaces of a conventional (ungrooved) flat

grinding wheel and a grooved flat grinding wheel. There are many different varieties of sizes and shapes of grooves in the literature. The groove pictured in Figure 2.2 is a shallow helical groove with a helix angle between 89° and 90°, which is often referred to in the literature as a "circumferential groove". This groove type has been shown to have improved performance over grooves with lower helix angles.

A complete review of grooved grinding wheels and their performance is covered in Chapter 3. In brief, the benefit of grooved wheels is that they reduce the process forces, specific energy and process temperatures during grinding [3]. They may also produce a texture on the workpiece surface, which can be considered a feature [10] or a disadvantage depending on the application.

2.2.1 Definition of a Helical Groove

Figure 2.3 shows a cylindrical coordinate system that can be used to describe the geometry of a grinding wheel.

In the literature, many different groove geometries are reported with various names: slotted grooves, helical grooves, circumferential grooves, spiral grooves, etc.

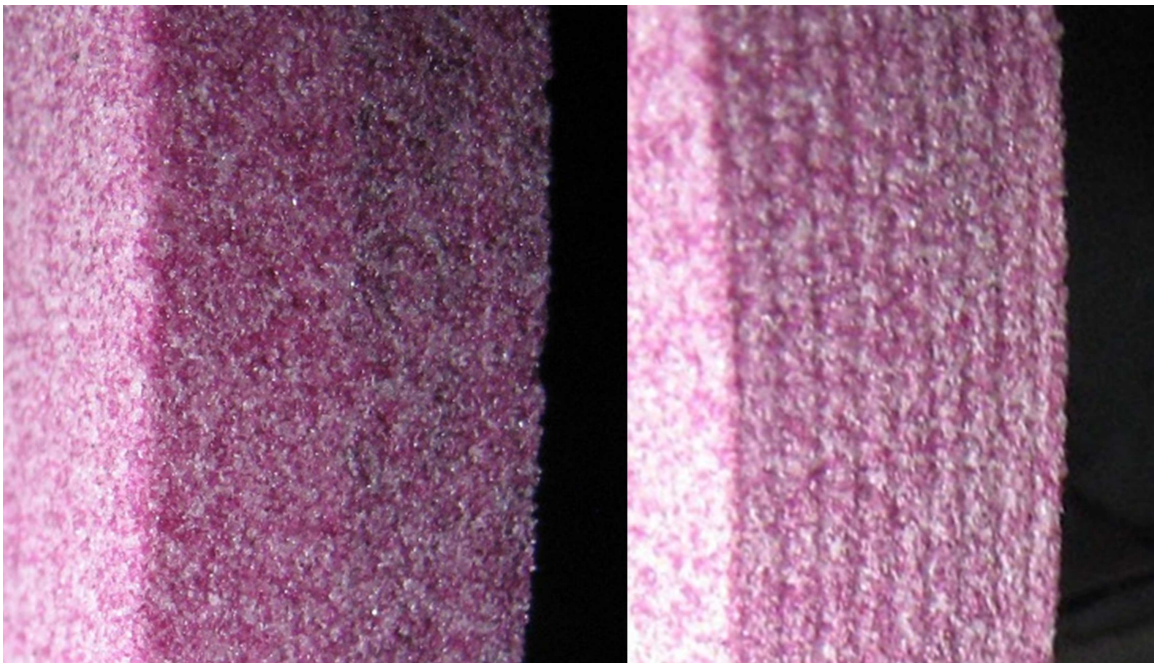

Figure 2.2: Photographs of the surfaces of grooved (right) and conventional/un-grooved (left) grinding wheels. Used with permission from [9].

All of these groove types can be described with only two parameters: the groove helix angle α_g and the number of starts N_g, assuming that the starts are equally spaced. Figure 2.4 shows a diagram describing the geometry of a groove on the surface of a flat grinding wheel.

The diagram in Figure 2.4 is a mapping of the wheel surface onto the φ–z plane,

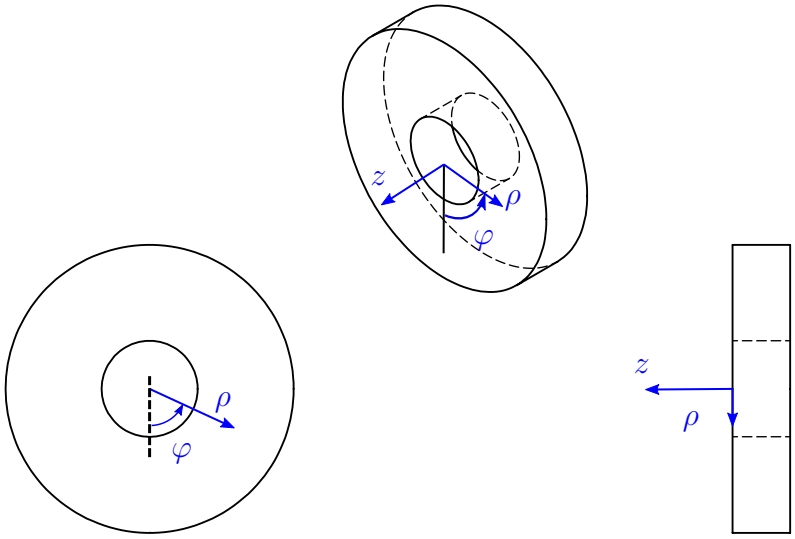

Figure 2.3: Diagram showing the cylindrical local coordinate system used to describe the geometry of a grinding wheel.

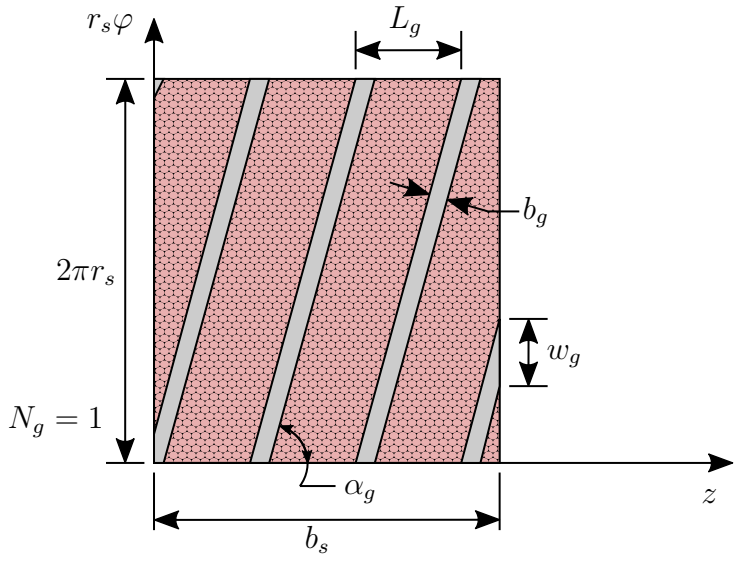

Figure 2.4: Diagram describing the geometry of helical grooves (Not to scale).

with the φ axis scaled by the radius of the grinding wheel r_s. Imagine covering the surface of a flat grinding wheel in ink and then rolling the grinding wheel across a long piece of paper for one full revolution. The grinding wheel would leave ink on the paper everywhere it touched the paper (dark patterned areas in the figure). The grooved sections of the wheel would not touch the paper and leave blank marks (light shaded areas in the figure). For most grinding wheels, the circumference of the wheel $2\pi r_s$ is significantly larger than the wheel width b_s; therefore, the scale of Figure 2.4 is greatly exaggerated for illustrative purposes.

From Figure 2.4, the groove helix angle can be calculated from the other groove parameters using

$$\alpha_g = \arctan\left(\frac{2\pi r_s}{L_g}\right), \tag{2.1}$$

where L_g is the lead of the grinding wheel in units of $\mathrm{mm\,rev^{-1}}$.

It was proposed by Forbrigger *et al.* [3] that a large number of the groove types demonstrated in the literature can be described by a helix, and therefore should be referred to as helical grooves. The general parametric equations describing a helix in Cartesian coordinates are

$$x = r\cos t\,, \tag{2.2}$$

$$y = r\sin t\,, \tag{2.3}$$

$$z = ct\,. \tag{2.4}$$

The curvature κ and torsion τ of a helix are defined as

$$\kappa = \frac{r}{r^2 + c^2}\,, \tag{2.5}$$

$$\tau = \frac{c}{r^2 + c^2}\,. \tag{2.6}$$

According to Lancret's theorem [11], a space curve is a helix if the ratio of its torsion τ and curvature κ is a constant, or:

$$\frac{\kappa}{\tau} = m\,,$$

for some real number m. This condition is both necessary and sufficient to classify a curve as a helix.

For the grooves described in the literature, the ratio of torsion divided by curvature can be defined by

$$\frac{\kappa}{\tau} = \frac{2\pi r_s}{L_g} = \tan \alpha_g \,. \tag{2.7}$$

Therefore, let a groove be defined as a helical groove if the helix angle of the groove is constant. For a flat grinding wheel, the radius of the wheel r_s is constant. Therefore, a groove on a flat wheel with a constant lead can also be classified as a helical groove. However, for a profile grinding wheel, the radius r_s is not constant over z; therefore, the groove lead L_g must also be a function of z to maintain a constant helix angle in order for the groove to be referred to as a helical groove.

2.2.2 Geometry of Helical Grooves

The groove width can be defined in two different ways, b_g and w_g, shown in Figure 2.4. The most commonly reported groove width is perpendicular to the groove trajectory, b_g. The reason for the popularity of this particular width is that it can be determined directly from the geometry of the tool used to create the grooves and it is independent of the rest of the groove geometry. The other way that groove width can be reported is by the groove width in the circumferential direction of the grinding wheel, w_g.

The circumferential groove width w_g can be calculated using (2.8).

$$w_g = \frac{b_g}{\cos \alpha_g} \tag{2.8}$$

The circumferential width has been shown to be important for determining the texture created on a workpiece by a grinding wheel [12, 13] as well as the temperature reduction properties of the groove [14].

The number of groove starts N_g is the number of separate groove paths. Figure 2.4 depicts a groove with a single start, $N_g = 1$. In the literature, grooves with low helix angles tend to have multiple starts and grooves with helix angles approaching $\alpha_g = 90°$ tend to have a single start. Grooves with a large helix angle and a single start have historically been referred to as "circumferential grooves". [3]

In 1979 Verkerk [12] introduced a parameter called the "groove factor" η_g, represented by the symbol η, as a non-dimensional way to describe the geometry of a grooved grinding wheel and allow comparisons between different groove geometries.

The groove factor is defined as the percentage of non-grooved wheel surface area:

$$\eta_g = \frac{A_o - A_g}{A_o}\,, \tag{2.9}$$

where A_o is the total cutting surface area of a non-grooved grinding wheel (entire shaded and patterned area in Figure 2.4) and A_g is the surface area removed by the grooving operation (light shaded area in Figure 2.4). Both areas can be calculated as follows for a flat grinding wheel with helical grooves:

$$A_o = 2\pi r_s b_s\,, \tag{2.10}$$

$$A_g = \frac{N_g b_s b_g}{\cos\alpha_g} = N_g b_s w_g\,. \tag{2.11}$$

Inserting (2.10) and (2.11) into (2.9) gives

$$\eta_g = 1 - \frac{N_g w_g}{2\pi r_s}\,. \tag{2.12}$$

This equation can be found in a paper by Mohamed *et al.* [13], rearranged to solve for w_g given a wheel radius and a desired groove factor. For a flat wheel with a helical groove, all of the terms on the right hand side of (2.12) are constants.

The definition of the groove factor is straightforward for grooves on a flat grinding wheel; however, there are several issues with the way the groove factor is defined. Firstly, the groove factor is a global measurement of the grinding wheel that does not account for local changes in performance that might be caused by a groove geometry that varies across the wheel width. Secondly, the definition uses grooved and un-grooved *areas* on the grinding wheel. Profile grinding wheels have significantly more surface area than flat wheels of the same width due to their changing radii. No author has discussed whether the areas to be measured for the groove factor are the surface areas of the grinding wheel or the areas projected to a cylindrical surface $r_s\varphi$–z (such as in Figure 2.4). The distinction between the two measurements is meaningless for a flat grinding wheel, but it becomes significant for a profile grinding wheel, especially for sections of the wheel with a large slope.

Later authors defined terms similar to the groove ratio: the "slotting factor" was defined by Suto in 1990 [15], and the "intermittent ratio" by Kim in 1997 [16]. Both of these authors also used the symbol η, but they defined the term using the

circumferential width of the grooves and the circumference of the grinding wheel instead of the area of the grooves and the total area of the grinding wheel. For helical grooves with constant depth on a flat grinding wheel the groove ratio and intermittent ratio are equal. However, the definition of the intermittent ratio is much simpler to extend to grooved profile.

Let the definition of the intermittent ratio for a grooved profile grinding wheel be the percentage of ungrooved wheel arc length at a given z position on the grinding wheel. Therefore the general expression for the intermittent ratio of any type of grooved wheel is

$$\eta_g(z) = \frac{2\pi r_s(z) - N_g w_g(z)}{2\pi r_s(z)} \,. \tag{2.13}$$

For a helical groove, the expression for the intermittent ratio becomes:

$$\eta_g(z) = 1 - \frac{N_g b_g(z)}{2\pi r_s(z)\cos\alpha_g} \,. \tag{2.14}$$

Equation (2.14) could be expressed as

$$\eta_g(z) = 1 - N_g \hat{w}_g(z) \,. \tag{2.15}$$

where $\hat{w}_g$ could be referred to as the normalized groove width.

2.3 Grinding Wheel Grooving Processes

Several authors have developed a variety of ways to produce grooves on a grinding wheel. Some methods involve modifying existing conventional grinding wheels while other methods involve manufacturing the grooves as a part of the grinding wheel manufacturing process. Each method has its own advantages and disadvantages that are discussed in detail in Chapter 3. The methods described in this section are grooving methods for vitrified bond grinding wheels. Other types of grinding wheels, such as metal bonded wheels, have used electroplating and electrochemical methods [8] but those types of grinding wheels are outside of the scope of this work.

The simplest method to groove a flat grinding wheel is to run a single-point diamond dressing tool along the grinding wheel width at a high feed rate and a low wheel angular velocity. This operation can be performed on any grinding machine and can produce single grooves with a small groove depth a_g (around 0.1 mm) and width.

This method is referred to as the *single-point grooving method* and has been used by several authors [14, 17]. Other authors developed more advanced versions of this method where the dressing tool is actuated independently of the grinding machine using servo motors [18] or an electromagnetic (EM) shaker [10]. Both the *single-point servo grooving* and *single-point EM shaker grooving* methods use feedback from the spindle encoder of the grinding machine to synchronize the grooving motion. This synchonization allows existing grooves to be deepened or sharpened and allows the creation of grooves with multiple starts. The single-point EM shaker method is highly versatile and can be used to create wheel textures as well as grooves [3].

Historically, the first method used in the academic literature to produce grooves on a grinding wheel was the *crushing roll grooving method* by Nakayama *et al.* in 1977 [19]. Patents for this grooving method have been found as far back as 1938 [20]. A specially-formed crushing roll dressing tool was manufactured with helical ridges that would produce shallow grooves on the grinding wheel. The geometry of the grooves could be modified by varying the relative rotation speeds of the crushing roll dressing tool and the grinding wheel [3].

A less popular grooving method is the *laser grooving method* which involves irradiating the surface of the grinding wheel with a high-intensity Nd:YAG (neodymium-doped yttrium aluminum garnet) laser. The method was demonstrated by mounting the grinding machine on an spindle outside of the grinding machine and slowly rotating the wheel while feeding the laser along the wheel width. [21, 22] Laser conditioning methods exist that can be used inside of the grinding machine, but none have been used to demonstrate grinding wheel grooving [3, 23].

Another grooving method, called the *machined groove method*, involves cutting deep grooves or "slots" in a conventional grinding wheel with a grinding machine or a milling machine [24–26].

The *moulded groove method* involves incorporating the groove geometry in the mould of the grinding wheel as the wheel itself is being manufactured. These grooves cannot be regenerated once the wheel is finished, so they extend the entire working radius of the grinding wheel. Kim *et al.* [16] used this method to create grooves filled with a solid lubricant [3].

Finally, the *segmented groove method* involves adhering abrasive segments on a

metal structural wheel rim. The grooves are created by leaving gaps between adjacent segments. An interesting feature of this method is that it was developed as part of a novel coolant distribution system [27–32]. Instead of supplying the coolant from outside of the wheel, the coolant was injected into the wheel rim and it would be forced out by centrifugal force through small holes in the rim between the abrasive segments. These holes allowed the coolant to be injected directly into the grinding contact zone [3].

One capability that every grooving method developed thus far lacks is the capability to create helical grooves on profile grinding wheels [3]. Grooves would likely be very useful for profile grinding wheels since they tend to reduce process temperatures and forces. Reduced process temperatures would help reduce the temperature concentrations in the corners of the profile and could help prevent workpiece thermal damage. Reduced process forces would help reduce static deflections and improve dimensional tolerances.

2.4 Conclusions

In this chapter the background information surrounding grinding processes and grooving processes was presented.

The advantages and disadvantages of grinding processes were presented. Grinding processes are useful for applications requiring hard materials to be machined, or applications where fine surface finish or dimensional tolerances are needed. The nature of abrasive cutting was described, where grains can either cut, plough or rub the surface of the workpiece.

The basics of grinding wheel composition was discussed. Grinding wheels are composed of abrasive grits, bond material and pores. The relative proportions of the three components can be adjusted to design grinding wheels for different applications. The abrasive grits and bond material come in many different varieties for different applications. The process of grinding wheel wear and the three different modes by which wear occurs were described.

The application of grinding wheels to profile grinding was then presented. Some example applications of profile grinding were discussed, demonstrating the importance of profile grinding to the aerospace and energy sectors.

Next grooved grinding wheels and their geometry were described. The definition of a helical groove was formalized and the advantages of using the intermittent ratio instead of the the groove factor were discussed.

Finally, the methods of creating grooves on vitrified bond grinding wheels were presented. It was concluded that none of the existing grooving methods are capable of producing grooves on a profile grinding wheel. It was proposed that grooves would likely be highly beneficial to a profile grooving process. This conclusion is what lead to the motivations behind the work presented in this manuscript.

Chapter 3

Literature Review

The material in this chapter has been published as a survey article "A review of state-of-the-art vitrified bond grinding wheel grooving processes" by the current author in the *International Journal of Advanced Manufacturing Technology* with co-authors Robert Bauer and Andrew Warkentin [3]. As such, permission notes and citations have been provided where necessary.

Interest in grinding wheels with slots or grooves can be traced back to patents in the early 20^{th} century for a slotted abrasive wheel [33] and a method of grooving abrasive wheels with a roller dresser [20]. However, it was several decades later before academic interest in grooved grinding wheels appeared. The earliest journal article on grooved wheels was written by Nakayama *et al.* in 1977 [19] which described a method of creating grooves on the surface of grinding wheel with a crushing roll dresser and listing the potential benefits of grooved wheels. The topic of grooved wheels has become more popular since then, with two-thirds of all articles on the topic published since 2000 [3].

In this chapter, a summary of experimental results from the literature on grooved grinding wheels is presented. The contributions of various authors are then discussed in more detail. Finally, the state-of-the-art of several grooving methods are compared and ranked on a set of performance criteria. The scope of this review extends to the grooving vitrified bond grinding wheels only. Textured grinding wheels and grinding wheels with other bond materials are not relevant to the work presented in this manuscript.

3.1 A Summary of Experimental Results

Tables 3.1, 3.2 and 3.3 summarize the experimental conditions, groove geometries and results of experimental investigations into grinding wheel grooves. These tables allow several conclusions to be drawn about the scope of the research into grooved

grinding wheels.

From Table 3.1, it can be seen that most grinding wheel grooving experiments have been performed with aluminum oxide abrasive wheels and steel workpieces. This is likely due to their availability and relatively low cost. Grooved grinding wheels have been tested on relatively soft materials such as copper, brass and aluminum, as well as harder materials such as ceramics and Inconel 175C. Surface grinding experiments have been the most popular method of investigating grooved wheel performance, although several authors have investigated cylindrical and creep-feed grinding conditions as well.

From Table 3.2, it can be seen that the most popular method of producing grooves has been the machining method. Single-point methods, both servo-actuated and electromagnetically actuated, have been developed relatively recently, starting with Oliveira *et al.* [10] in 2010. Laser grooving methods were investigated by Babu and Radhakrishnan [21] in 1989, but no authors have investigated that method since that time. Most of the literature has focused on wheels with large numbers of grooves and low helix angles (less than 45°). The groove widths investigated have been generally on the order of several millimeters. Groove depths vary, and are mostly unreported, but tend to be on the order of tenths of millimeters to several millimeters.

Table 3.3 clearly shows consensus throughout the literature as to the benefits of grooved grinding wheels. All authors who investigated specific energy, process forces and process temperatures of grooved wheels versus conventional wheels during grinding reported lower forces, lower specific energy, and lower process temperatures for grooved wheels. Few authors investigated the effect of grooves on wheel wear. Of the authors that did investigate this property, it was found that grooved wheels were either negligibly different or experienced slightly more wear when compared to conventional grinding wheels. The most contentious effect of grinding wheel grooves is their effect on workpiece surface roughness. Seven out of the fourteen authors summarized in Table 3.3 agreed that grooved wheels produced increased surface roughness on the workpiece. Three authors reported decreased workpiece surface roughness for grooved grinding wheels and two authors reported negligible differences or that the roughness varied with groove geometry.

Author and year		Grinding process	Workpiece material	Abrasive material/wheel type
Nakayama *et al.* [19]	1977	Surface	Steel	Al_2O_3/A-46-J-6-V
Verkerk [12]	1979	Surface	Steel	Al_2O_3/A-100-K-7-V
Babu & Radhakrishnan [21]	1989	Plunge	Steel	Al_2O_3/A-60-K-5-V
Suto *et al.* [15]	1990	Creep-feed	Nickel-base alloys	cBN/B-(140/170)-P-_-V-_-2
Waida *et al.* [27]	1991	Creep-feed	Ceramics, cermets, Inconel	Diamond/D-(170/200)-Q-100-V
Kim *et al.* [16]	1997	Surface	Cu, brass, Al, steel	Al_2O_3/A-60-L-7-V
Kwak & Ha [24]	2001	Surface	Steel	Al_2O_3/A-100-L-_-V
Fu *et al.* [34]	2002	Surface	Cast-iron	cBN/(80/100) grit, electroplate
Nguyen & Zhang [32]	2009	Plunge	Steel	cBN/B-100-P-120-V-_-_
Oliveira *et al.*	2010	Cylindrical	Steel	Al_2O_3/A-80-K-_-V
Köklü [25]	2012	Cylindrical	Steel	Al_2O_3/A-60-K-6-V
Uhlmann & Hochschild [26]	2013	Cylindrical	Steel	cBN/B-126-X-150-V-_-_
Mohamed *et al.* [17]	2013	Creep-feed	Steel	Al_2O_3/A-60-J-5-V
Aslan & Budak [14]	2015	Surface	Steel	SiC/C-80-J-5-V

Table 3.1: Summary of experimental conditions for each author. Grinding wheel specifications are given according to ANSI Standard B74.13-1977, where possible. Properties not provided by the authors are indicated by "_". Reproduced with permission from [3].

Author and year		Number	α_g	b_g [mm]	Depth [mm]	Grooving Method
Nakayama *et al.* [19]	1977	>20	60°	2	–	Crushing roll
Verkerk [12]	1979	225–545	22°–67°	1–1.2	>10	Machined
Babu & Radhakrishnan [21]	1989	1	$\sim$ 89.9°	$\sim$ 0.5	$\sim$ 0.1	Laser
Suto *et al.* [15]	1990	120	0°	2.6	–	Segmented
Waida *et al.* [27]	1991	120	0°	2	2–5	Segmented
Kim *et al.* [16]	1997	18–32	0°–45°	6–18	>10	Molded and machined
Kwak & Ha [24]	2001	6–24	0°	6	–	Machined
Fu *et al.* [34]	2002	37–75	0°	2–4	–	Machined
Nguyen & Zhang [32]	2009	144	0°	3.27	–	Segmented
Oliveira *et al.*	2010	4	–	–	0.002–0.025	S-P, shaker
Köklü [25]	2012	24	15°–45°	2.6	3	Machined
Uhlmann & Hochschild [26]	2013	70	32°	1–5	5	Machined
Mohamed *et al.* [17]	2013	1	85°–90°	0.5–1.08	0.2–0.5	S-P, servo
Aslan & Budak [14]	2015	1	89°–90°	1.1	0.1	S-P, servo

Table 3.2: Summary of groove geometries for each author. Some values are expressed as a range (#–#), while others are approximated from other values given by each author ($\sim$#). Reproduced with permission from [3].

Author and year		Specific Energy	Process Forces	Process Temperatures	Wheel Wear	W.P. surface roughness
Nakayama *et al.* [19]	1977	–	▼	▼	•	Varies
Verkerk [12]	1979	–	–	▼	▲	▲
Babu & Radhakrishnan [21]	1989	–	▼	–	–	▲
Suto *et al.* [15]	1990	▼	–	▼	–	•
Waida *et al.* [27]	1991	▼	–	–	–	▲
Kim *et al.* [16]	1997	–	–	▼	–	▼
Kwak & Ha [24]	2001	–	▼	▼	–	▲
Fu *et al.* [34]	2002	▼	–	▼	–	–
Nguyen & Zhang [32]	2009	▼	▼	–	–	–
Oliveira *et al.*	2010	▼	–	–	–	▲
Köklü [25]	2012	–	▼	–	–	▼
Uhlmann & Hochschild [26]	2013	▼	▼	▼	▲	▼
Mohamed *et al.* [17]	2013	▼	▼	▼	•	▲
Aslan & Budak [14]	2015	–	▼	–	•	▲

Table 3.3: Summary of grooved wheel performance. The symbols used indicate whether the given properties were observed to have increased (▲), decreased (▼), or were negligibly affected (•) by grinding with grooved wheels versus grinding with conventional wheels. Properties indicated with (–) were not commented upon by that author. Reproduced with permission from [3].

3.2 Explanations for the Improved Performance of Grooved Wheels

Several authors have put forward explanations for why grooved grinding wheels show improved grinding performance compared to conventional wheels: 1) grooved wheels improve coolant delivery to the contact zone, and 2) grooved wheels increase the uncut chip thickness.

Some grooved wheels were designed specifically with the intention of improving the coolant delivery to the contact zone between the wheel and the workpiece. Nguyen and Zhang [30] modelled the effects of a novel coolant delivery system where the coolant is injected through holes directly between the abrasive segments. This system was later implemented by the same authors [29, 31, 32] and was shown to greatly improve the coolant delivery, allowing less coolant to be used to obtain similar cooling performance. Similarly, Kim *et al.* [16] designed a grooved grinding wheel where the grooves were filled with solid lubricant. However, even without incorporating special coolant delivery systems, grooved wheels show improved coolant delivery compared to conventional wheels. Mohamed *et al.* [35] showed that grooved wheels can deliver at least 56.5% more coolant to the contact zone than conventional wheels.

Aslan and Budak [14] developed a model to investigate the uncut chip thickness of grooved grinding wheels. According to their model, grooved grinding wheels should produce larger chip sizes. Mohamed *et al.* [35] used an electron microscope to measure chips from conventional and grooved wheels. Chips from grooved wheels were found to be approximately seven times larger than chips from conventional wheels, resulting in a lower specific energy of machining.

3.3 The Effects of Groove Geometry on Grinding Performance

While grooved grinding wheels show improvements over conventional wheels, the exact effects of changing the groove geometry of a grooved wheel are still being investigated.

Köklü [25] concluded that the residual stress in workpieces ground with helically grooved wheels was reduced compared to those ground by conventional wheels. Furthermore, the performance of the grooved wheels was shown to vary with the helix

angle. Grooves with helix angles from $\alpha_g = 15^\circ$ to 45° were investigated. In general, higher helix angles correlated to lower workpiece roughness and reduced residual stress.

Mohamed *et al.* [17, 18] concluded that grooved wheels with lower groove factors reduce the specific energy of machining. The authors used wheels with a helix angle significantly higher than previous authors, approaching $\alpha_g = 90^\circ$, and found that this groove geometry resulted in a lower rate of wheel wear. Furthermore, Mohamed *et al.* showed that groove width had a significant effect on grinding performance independent of the groove factor of the grinding wheel.

Oliveira *et al.* [10] used wheels with several different groove patterns including helical grooves, triangular wave groove patterns, and diamond-shaped patterns for cylindrical grinding. The authors determined that helical grooves resulted in the lowest specific energy of machining, but a higher surface roughness, out of the various patterns that they tested.

3.4 Helical Grooves and Workpiece Surface Roughness

It was noted previously from Table 3.3 that many authors found grooved grinding wheels produced worse workpiece surface finish (increased surface roughness) than conventional wheels. Verkerk [12] was the first author to propose an explanation for the increase in surface roughness. Verkerk noted the similarity between a milling process and a grinding process with a helically grooved wheel with a helix angle of $\alpha_g = 0^\circ$. Gaps in the wheel would lead to a series of regular peaks present on the workpiece surface after grinding. In other words, grooved wheels produce a regular and predictable *surface texture*. Using this analogy, Verkerk developed the following equation to describe the equivalent surface roughness introduced to the workpiece surface by the surface texture:

$$R_{t,g} = \frac{{w_g}^2}{4d_e \left(1 \pm v_s/v_w\right)^2} \,. \tag{3.1}$$

The sign in the denominator is positive for up-grinding (wheel velocity and workpiece velocity are in opposite directions in the grinding area) and negative for down-grinding (wheel velocity and workpiece velocity are in the same direction in the grinding area). Using this formula, Verkerk concluded that the groove geometry and grinding conditions could be chosen to reduce the surface texture such that a grooved wheel would produce a comparable surface roughness to a conventional grinding wheel [12].

Verkerk demonstrated the effects of (3.1) experimentally. Verkerk showed that reducing the groove width and increasing the velocity ratio improved the surface roughness of a grooved wheel [12]. Verkerk's conclusions are further supported by earlier work by Nakayama *et al.* [19]. Nakayama *et al.* found that, for a helically grooved wheel with constant wheel velocity, low workpiece feeds v_w resulted in comparable workpiece surface roughness between grooved wheels and conventional wheels. Furthermore, higher workpiece feeds resulted in significantly worse workpiece surface roughness for the grooved wheel but had no discernible effect on the conventional wheel surface roughness.

The surface texture produced by helically grooved grinding wheels was further investigated by Mohamed *et al.* [13]. Mohamed *et al.* performed a kinematic analysis of the cutting edges of a helically grooved wheel and used a model to predict the surface texture resulting from surface grinding with a grooved wheel. It was demonstrated that the surface texture could be controlled by modifying the groove geometry and the grinding conditions.

Kwak and Ha [24] performed surface grinding experiments with helically grooved wheels with a helix angle of $\alpha_g = 0°$. The surface roughness of the workpiece was found to increase with increasing numbers of grooves. The width of the grooves and the grinding conditions were held constant for the experiments; therefore the resulting increase in surface roughness is not explained by (3.1). The authors proposed instead that the increase in surface roughness was due to chatter introduced by the intermittent contact between the workpiece and the grinding wheel.

Oliveira *et al.* [10] and da Silva *et al.* proposed that the textures produced by grooved wheels on workpieces could be exploited for practical purposes such as retaining lubricant on bearing surfaces.

Grooving Method	Process Speed	Groove Depth	Groove Complexity	Flexibility
Laser	1	2	3	3
Crushing roll	2	2	2	1
S-P, shaker	2	1	3	3
S-P, servo	2	2	2	3
Segmented	3	3	1	1
Machined	1	3	1	3
Molded	3	3	1	1

Table 3.4: Summary of scores from 1 to 3 for each grooving method in each category. Reproduced with permission from [3].

3.5 Comparison of Grooving Processes

In Chapter 2, several methods of producing grooves on grinding wheels were described. Each method has its own strengths and weaknesses relative to the other methods. In this section the relative strengths and weaknesses of each method are quantified using a score from one to three in several categories. A score of one indicates a relative weakness of the method while a score of three indicates a relative strength. A summary of the scores for each method are presented in Table 3.4.

The ranking categories are defined as follows.

- *Process speed*: This category refers to the amount of time taken for a groove to be produced on a grinding wheel for each method. A manufacturer would want to maximize the time spent grinding and therefore minimize the time spent conditioning/grooving the wheel. If the grooving method produces grooves that do not need to be regenerated or sharpened, the method receives a score of 3. If the grinding wheel has to be removed from the grinding machine to be grooved, the grooving method is given a score of 1. Any method for which neither of the previous statements is true receives a score of 2 [3].

- *Groove depth*: This category refers to the maximum possible groove depth achievable by each method. Larger groove depths are considered beneficial because they require regrooving less often. Any other effects of groove depth on wheel performance are currently unknown. Therefore, methods that can produce grooves that extend the entire working radius of the wheel are given

a score of 3. Methods that can produce grooves that are only fractions of a millimeter deep are given a score of 1. Methods in between those two extremes are given a score of 2 [3].

- *Groove complexity*: This category refers to the variety of geometries that each method is capable of producing. The capability to produce a large variety of groove geometries is considered desirable, especially considering the potential applications for engineered workpiece surface textures. A method that can produce any desired geometry is given a score of 3. A method that can produce only a limited number of simple groove geometries (e.g. helical grooves only) receives a score of 1 [3].

- *Flexibility*: This category refers to the capability of each grooving method to produce different groove geometries without reconfiguring or rebuilding the device used to create the grooves. Methods that can simply be programmed to produce a different groove geometry receive a score of 3. Methods that require new equipment to be created or purchased for each different groove geometry receive a score of 1 [3].

The justification for the scores given to each grooving method is detailed in the following sections. These scores reflect the performance of the grooving methods as shown in literature. While some grooving methods clearly have the potential for improved performance in some categories, Forbrigger *et al.* [3] preferred to speculate as little as possible to better represent the current state-of-the-art.

Laser Dressed

The solid line in Figure 3.1 presents the scores for the laser grooving method.

- *Process speed*: (score = 1) This method requires the wheel to be removed from the grinding machine and to rotate at very low speeds, around 0.25 rpm [21].

- *Groove depth*: (score = 2) Groove depths up to 0.3 mm have been demonstrated with this method [21].

- *Groove complexity*: (score = 3) In literature, the method has only been shown to produce helical grooves with helix angles approaching $\alpha_g = 90°$. However,

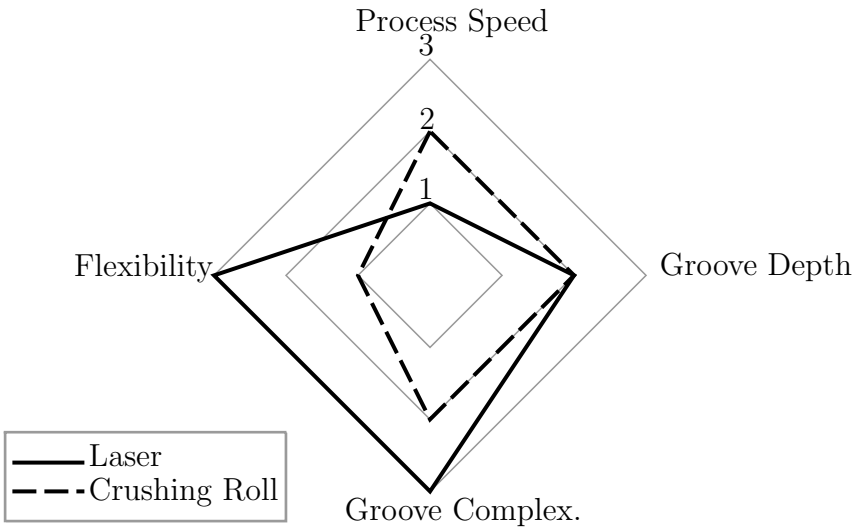

Figure 3.1: Radar chart comparison of laser and crushing roll grooving methods. Reproduced with permission from [3].

based on the nature of the method, it is a reasonable assumption that a wide variety of groove geometries could be produced.

- *Flexibility*: (score = 3) The method is controlled electronically and can be reprogrammed to produce different groove geometries.

There are additional advantages and disadvantages to the laser dressed grooving method that are not covered by these categories. Laser conditioning methods tend to produce a smooth melted surface layer on the grinding wheel which greatly increases grinding forces and reduces material removal until the melted surface is worn away [21–23, 36]. One advantage is that it does not suffer from tool wear, and therefore can create a consistent groove cross-section even after extended use.

Crushing Roll Dressed

The dashed line in Figure 3.1 presents the scores for the crushing roll grooving method.

- *Process speed*: (score = 2) This method has been shown to be able to be implemented inside of the grinding machine.

- *Groove depth*: (score = 2) This method is limited to groove depths up to 3 mm. Larger depths may damage the structure of the grinding wheel [12].

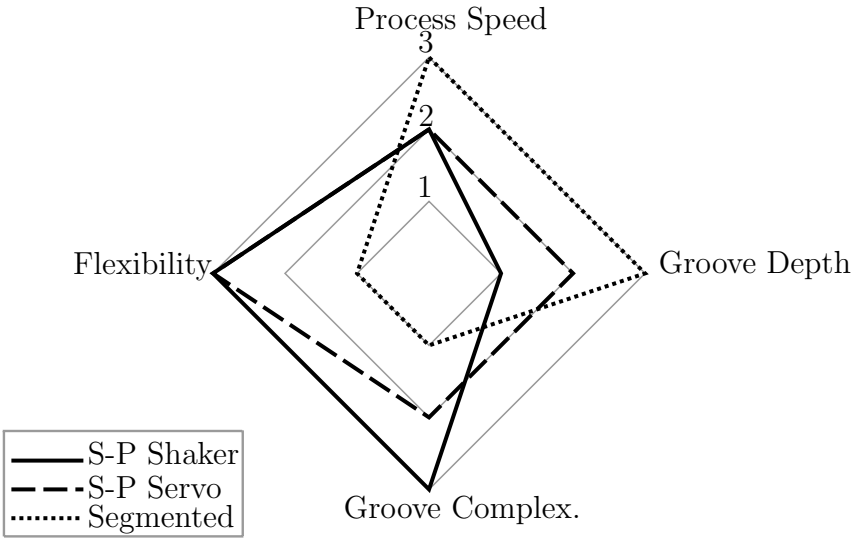

Figure 3.2: Radar chart comparison of single-point shaker, single-point servo and segmented grooving methods. Reproduced with permission from [3].

- *Groove complexity*: (score = 2) This method has been shown to be able to produce a variety of helical grooves.

- *Flexibility*: (score = 1) This method can produce a variety of helical grooves on a grinding wheel by varying the relative speeds of the crusing roll and grinding wheel and the angle between the axes of the crushing roll and grinding wheel. This method has been shown to be capable of producing helical grooves only [37].

Single-point, EM Shaker Dressed

The solid line in Figure 3.2 presents the scores for the single-point electromagnetic shaker grooving method.

- *Process speed*: (score = 2) This method has been shown to be able to be implemented inside of the grinding machine [10].

- *Groove depth*: (score = 1) This method is limited to the amplitude of the EM shaker which decreases at higher frequencies. The method has been shown to produce grooves with a maximum depth of 25 µm [10].

- *Groove complexity*: (score = 3) This method has been shown to be capable of grooving almost any pattern.

- *Flexibility*: (score = 3) The method is controlled electronically and can be reprogrammed to produce different groove geometries.

Single-point, Servo Dressed

The dashed line in Figure 3.2 presents the scores for the single-point servo grooving method.

- *Process speed*: (score = 2) This method has been implemented inside of the grinding machine [18].

- *Groove depth*: (score = 2) This method has been shown to be capable of producing grooves serval millimeters deep depending on the tool used.

- *Groove complexity*: (score = 2) This method is not capable of producing groove paths with discontinuities and it is limited by the maximum speed of its actuators. This method cannot create helical grooves with a helix angle of $\alpha_g = 0°$ — which would require an infinite feed rate. Otherwise, this method has been shown to be capable of a variety of groove geometries.

- *Flexibility*: (score = 3) The method is controlled electronically and can be reprogrammed to produce different groove geometries [18].

Some single-point grooving devices can retrace an existing known groove geometry by synchronizing their motion with the spindle encoder of the grinding machine. Without the encoder synchronization, this method is similar to other grooving methods, which require the grooves to first be removed by dressing and then re-grooved.

Segmented

The dotted line in Figure 3.2 presents the scores for the segmented grooving method.

- *Process speed*: (score = 3) This method can be used for its entire working radius without needing the groove to be regenerated. The abrasive segments can be

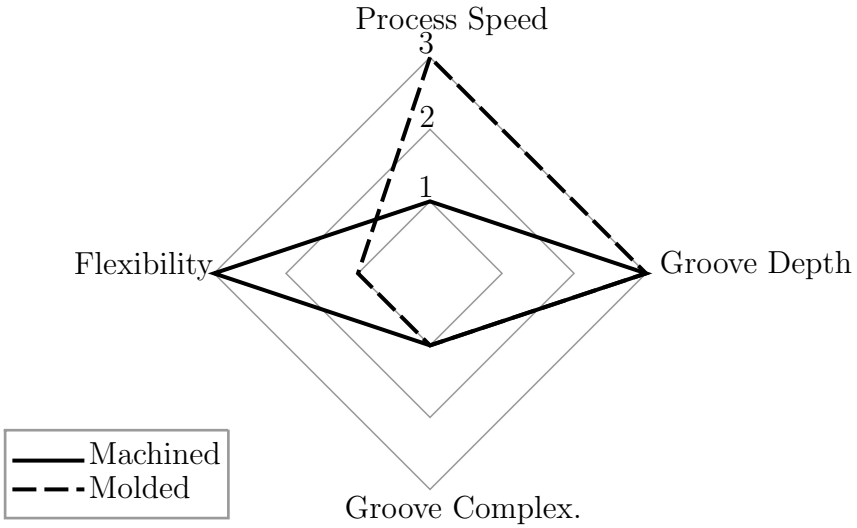

Figure 3.3: Radar chart comparison of machined and molded grooving methods. Reproduced with permission from [3].

replaced on the metal wheel rim once they have been worn down to an unusable size.

- *Groove depth*: (score = 3) This method can be used for its entire working radius without needing the groove to be regenerated, although the size of the abrasive segments (on the order of tens of millimeters) is smaller than the working radius of some conventional grinding wheels (around 100 mm).

- *Groove complexity*: (score = 1) This method has only been demonstrated with helical grooves with a helix angle of $\alpha_g = 0°$.

- *Flexibility*: (score = 1) New segment geometries would need to be machined or purchased any time a different groove geometry is desired.

Machined

The solid line in Figure 3.3 presents the scores for the machined grooving method.

- *Process speed*: (score = 1) This method has been used to produce both shallow grooves [25] that would need to be reproduced several times over the life of the wheel and grooves extending the working radius of the wheel [16]. In order

to produce the grooves the grinding wheel must be removed from the grinding machine.

- *Groove depth*: (score = 3) The groove depth for this method has been shown in the literature to be able to extend the entire working radius of the grinding wheel.

- *Groove complexity*: (score = 1) The geometry of this method is limited by the tool used to machine the grooves. In the literature a cut-off disc was used to create the grooves, which is not capable of intricate geometries [25].

- *Flexibility*: (score = 3) This method is capable of producing different groove geometries without requiring modification of the machine tools used.

Molded

The dashed line in Figure 3.3 presents the scores for the molded grooving method.

- *Process speed*: (score = 3) This method can be used for its entire working radius without needing the groove to be regenerated.

- *Groove depth*: (score = 3) The grooves can have a depth that extends the entire working radius of the wheel.

- *Groove complexity*: (score = 1) The only grooves produced by this method shown in literature were helical grooves with a helix angle of $\alpha_g = 0°$ [16].

- *Flexibility*: (score = 1) A completely new wheel must be ordered every time a new geometry is desired.

One advantage to this method that is not covered by the above categories is that the grooves can be filled with solid lubricant when the wheel is manufactured [16].

3.6 Conclusions

In this chapter a literature review of grooving vitrified bond grinding wheels was presented. From this review, several conclusions can be made about grinding wheel grooving research.

Grooving research has been performed with a variety of grinding processes, workpiece materials and groove geometries. The majority of authors used grooves with helix angles α_g less than 45° and large numbers of grooves (more than 10). Recently, authors have begun investigating single grooves with large helix angles.

Grooved grinding wheels have consistently shown reduced forces, reduced specific energy of machining and reduced temperatures compared to conventional grinding wheels. Two explanations for these performance improvements have been proposed and validated experimentally: grooves improve coolant flow to the contact zone and grooves increase the uncut chip thickness. Most authors have also shown a trade-off between reduced cutting forces and increased workpiece surface roughness.

A significant amount of research has been conducted improving the understanding of the surface texture or surface roughness generated by grooved wheels. However, the effects of groove geometry on grinding wheel performance parameters such as cutting forces and specific energy are still not well understood. Several authors have demonstrated trends in forces and specific energy with individual parameters, and there is evidence to suggest that higher helix angles and lower groove factors result in improved performance (reduced forces). This review of groove geometry influenced the choice of helix angle and groove width for the experimental investigation presented in Chapter 6.

There are still many areas of grooved grinding wheel research with significant potential for investigation. The the economics of implementing grooving in an industrial setting are completely unexplored, including grooving process times, and the material and energy consumed in grooving processes. The relative importance of each helical groove geometry component (helix angle, groove width, groove depth, groove factor) on the cutting forces and power could also be investigated. Furthermore, groove geometries other than helical and their relative performance could be explored.

Finally, no authors have investigated the use of helical grooves for profile grinding operations. In fact, none of the existing grooving methods, in their current state, are capable of creating helical grooves on a profiled grinding wheel. The review and comparison of grinding wheel grooving technology in this Chapter was used to inform the design of the multi-axis grooving robot in Chapter 4.

Chapter 4

Design of a Multi-Axis Grooving Device

From the literature review it was determined that no methods of creating a helical groove on a profile grinding wheel have been demonstrated in the literature. It was decided that a device should be designed and constructed that can create grooves on a profile grinding wheel.

The single-point servo method, as described in Chapter 2, was determined to be the most suitable method to be extended to the application of producing grooves on profile grinding wheels for several reasons. Firstly, a single-axis single-point grooving device has already been used extensively in the author's research group, therefore the new grooving device could be constructed using knowledge and components from the older design. Secondly, the re-grooving capability demonstrated by this method, as well as its flexibility in programming and executing many different trajectories, makes the method well suited to grooving research purposes. Finally, the single-point servo method can be implemented inside the grinding machine, allowing rapid production of different groove geometries without needing to remove the grinding wheel from the machine.

In this chapter, a summary of the design process of a multi-axis grooving device is presented. First an experiment to determine the forces present on a single-point dressing tool during grooving is presented. Then the design requirements are described, followed by an overview of the final design including details of equipment selection and subsystems. Finally the design is validated experimentally to show that it meets the design requirements.

4.1 Forces on a Single-Point Diamond Dressing Tool

There is a lack of information in the literature regarding the forces present on single-point dressing tools during operation. Regular dressing operations use small depths of cut (less than 0.025 mm) and low feed rates, so the forces on the tools are generally

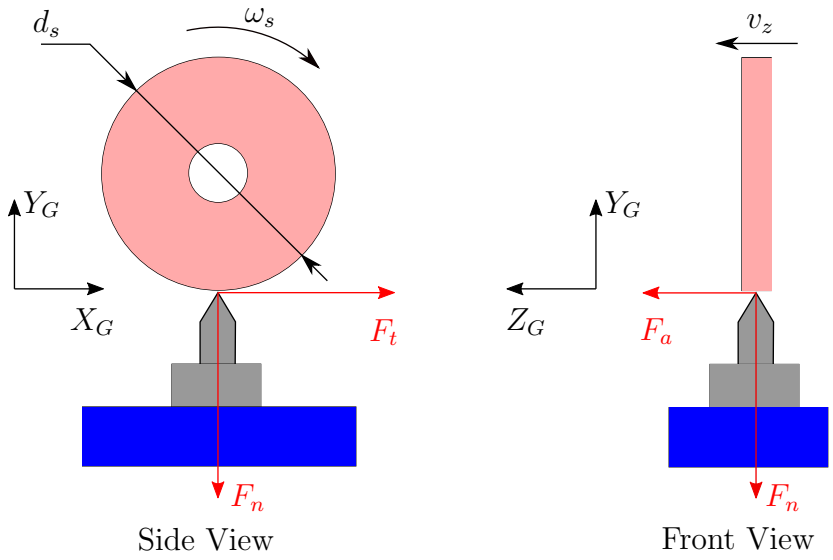

Figure 4.1: Diagram of the experimental setup to measure dressing tool forces, showing the directions of the tangential F_t, normal F_n and axial F_a forces experienced by the dressing tool.

small. From Table 3.2, the maximum single-point servo groove depth investigated in the literature was 0.5 mm. The only reported values found for dressing tool forces in the literature were given in a paper by Mohamed *et al.* [18], showing maximum magnitudes of around 100 N. A brief summary of this experiment was presented showing increasing groove forces with increased grinding wheel speed. However, the depth of the grooves was not reported. Therefore it was necessary to conduct a separate investigation into the grooving forces experienced by a single-point diamond tool at different depths of cut in order to size the actuators needed for a multi-axis grinding wheel grooving device.

4.1.1 Experimental Setup

For this experiment, a single-point diamond dressing tool with a nose radius of 0.508 mm and a cone angle of 60° was mounted on a Kistler 9257B Multicomponent Dynamometer. The signals from the dynamometer were amplified using a Kistler 5019B Charge Amplifier and the amplified signals were measured by a National Instruments PCI-MIO-16XE-10 data acquisition board at 250 Hz. A diagram of the experimental setup is shown in Figure 4.1.

In Figure 4.1, the force on the tool is divided into three components: the component tangential to the wheel surface F_t, which acts in the direction of the grinding machine x-axis; the component normal to the wheel surface F_n, which acts in the negative direction of the grinding machine y-axis; and the component acting along the axis of the wheel F_a, which acts parallel to the z-axis of the grinding machine. Each component can be measured separately by the dynamometer. The most important forces for sizing the actuators of the grooving device are the F_n and F_a components.

All grooving experiments were performed using an alumnimum oxide, vitrified bond grinding wheel (Radiac Abrasives WR–A–60–J–5–V). The angular velocity of the wheel was 155 rpm (16.23 rad/s) and the dressing tool feed was 5.08 mm/rev for all trials. These parameters produced grooves with a helix angle of 89.76° and a groove factor of 78.7%. Coolant was not used during the grooving process because the force exerted on the tool by the coolant jet was non-negligible. The lack of coolant will also give a good approximation of "worst-case-scenario" grooving forces on a profiled wheel, where the coolant conditions may vary across the wheel. The groove geometry was chosen to reflect similar values used in [17, 18].

4.1.2 Results and Discussion

Nine separate trials were performed, with three trials at each groove depth a_g of 0.1016 mm, 0.2032 mm and 0.5080 mm. The wheel was dressed between each trial with the same tool at a dressing depth of 0.0127 mm, a feed rate of 25.4 $\mathrm{mm\,min^{-1}}$ and a wheel surface speed of 20.3 $\mathrm{m\,s^{-1}}$. The grinding wheel diameter was 402 mm for the first trial and 398 mm for the last trial. The results are presented in Figure 4.2, Figure 4.3 and Figure 4.4.

Figure 4.2 presents the average forces measured by the dynamometer during the grooving process. The maximum average forces in the normal, tangential and axial directions were 71.9 N, 66.8 N and 9.4 N, respectively. There is a clear increasing trend in the tangential and normal forces with increasing groove depth. There was no detectable increase in the axial force with increasing groove depth. A probable reason for the lack of an increasing trend in the axial forces is that the forces were too small to be accurately measured by the force dynamometer.

It is reasonable to assume that the average axial and tangential forces are similar

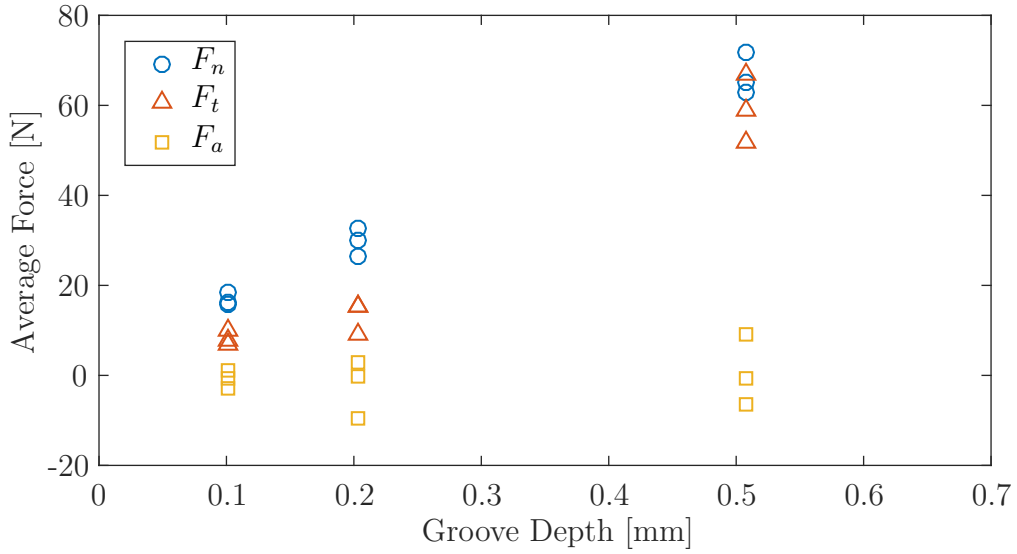

Figure 4.2: Average forces measured during grooving for several depths of cut.

in relative proportion to the axial and tangential tool speeds, that is

$$\frac{\bar{F}_a}{\bar{F}_t} \approx \frac{v_z}{v_s},$$

where v_z is the tool feed rate along the axial direction of the wheel and v_s is the surface speed of the grinding wheel. The feed of the tool was previously stated as 5 mm/rev, which gives a feed rate of $v_z = 0.013\ \mathrm{m\,s^{-1}}$. The wheel velocity, based on the previously stated angular velocity and wheel diameter, was $v_s = 3.230\ \mathrm{m\,s^{-1}}$. These values yield a ratio of $\frac{v_f}{v_s} = 0.004$. Therefore, given the highest measured average tangential force of 66.8 N, the largest expected axial forces would be on the order of several tenths of a newton. It is also important to consider the accuracy of the force dynamometer which, for the calibration range that was used for the experiments, was ± 5 N. Therefore it is reasonable to conclude that, while there may have been increasing axial forces with increasing depth of cut, the difference between these forces could not be accurately measured with the equipment used.

The force signal during the grooving process was highly dynamic in nature, with significant noise superimposed on the signal average. The noise in the force signals is likely due in part to the wheel structure itself. As the tool cuts through the wheel it encounters randomly distributed grains, voids, and bond material within the wheel structure, each presenting different amounts of resistance to the tool. The

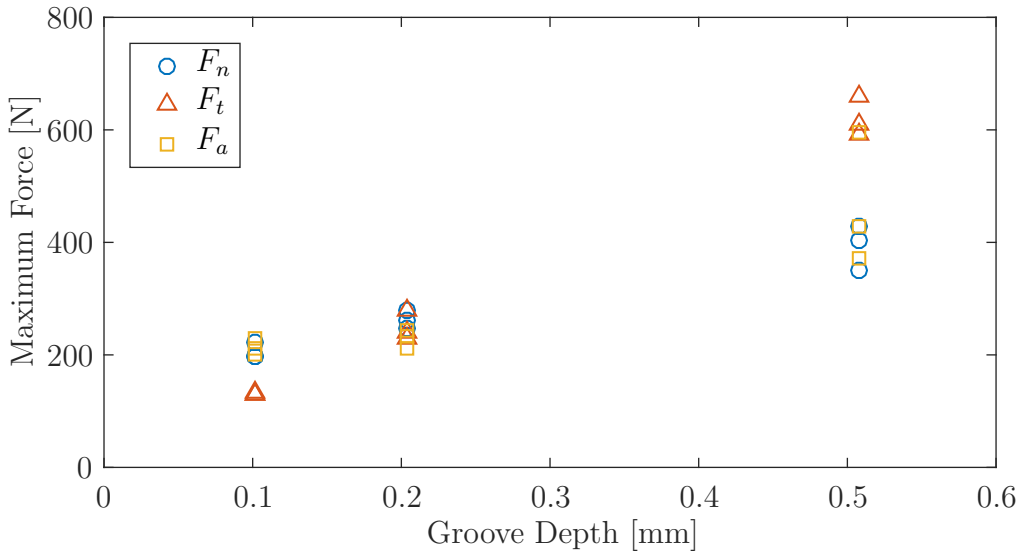

Figure 4.3: Peak forces measured during grooving for several depths of cut.

random nature of the wheel structure would cause the measured grooving forces to be composed of many impacts as the tool makes and leaves contact with the grains or bond material. It is possible that the noise could be due to chatter in the tool; however, a frequency spectrum analysis of the force signals showed uniform frequency content. In other words, the noise present in the force signals was Gaussian white noise; therefore it is unlikely that the noise is being caused by chatter and more likely that it is due to the random nature of the wheel structure.

In order to represent the dynamic components of the force signals, the peak forces during grooving are presented in Figure 4.3 and the root-mean-squared (RMS) amplitudes of the force signals during grooving are presented in Figure 4.4.

In Figure 4.4, the RMS amplitudes during grooving are larger than the average forces by approximately a factor of two. The maximum RMS amplitudes in the normal, tangential and axial directions were 110.1 N, 179.2 N, and 126.8 N respectively. Of particular note is the fact that the axial force RMS amplitude increased with increasing depth of cut. This increase further supports the idea that the axial forces are increasing with increasing depth of cut, but that the average force is still too small to measure.

Furthermore, the peak forces shown in Figure 4.3 are larger than the average grooving forces by approximately a factor of ten. The magnitude of the maximum

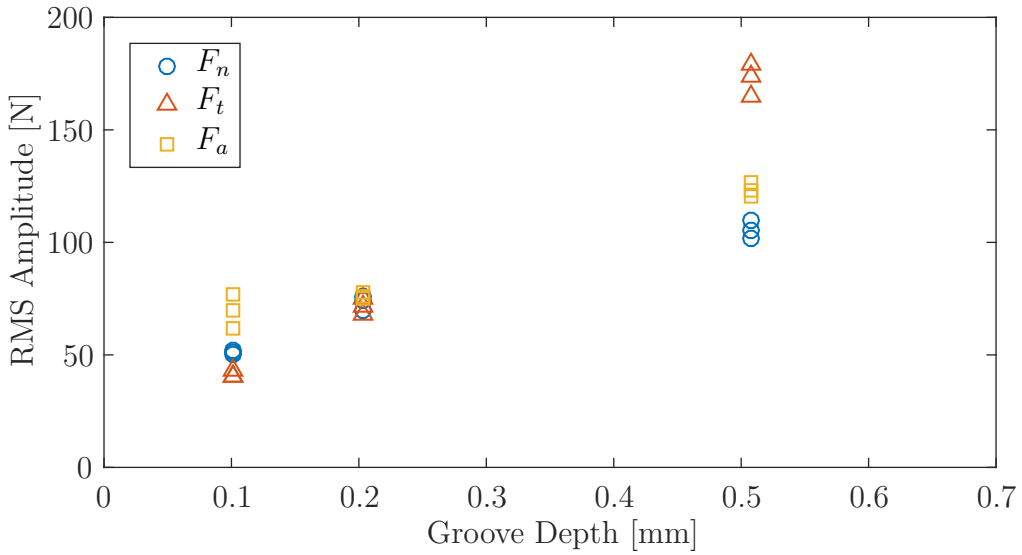

Figure 4.4: Root-mean-squared amplitude of the forces measured during grooving for several depths of cut.

forces relative to the average forces further supports the idea that the grooving force is composed of many random impacts, as opposed to a continuous force resisting the cutting. The maximum peak forces during grooving in the normal, tangential and axial directions were 427 N, 660 N, and 427 N respectively. Any actuator sizing will need to take the significant vibration magnitudes into consideration.

4.1.3 Conclusions

In this section, an experimental investigation of the forces on a single-point diamond dressing tool during a grooving operation was presented. The purpose of the investigation was to determine the loads for sizing the actuators of a multi-axis grooving device.

The average forces measured during a worst-case-scenario grooving process with no coolant and an aggressive depth of cut were 71.9 N, 66.8 N and 9.4 N in the normal, tangential and axial directions, respectively. The normal and tangential average forces increased with increasing groove depth, but the average axial force did not show a similar trend, likely because it was not accurately measurable with the equipment used.

The force signals during grooving were highly dynamic; therefore, it was concluded

that any actuator sizing should take the RMS amplitudes of the forces into account. Furthermore some vibration-damping components may be necessary. The dynamic nature of the force signals was found to have no dominant frequencies, instead the signal was best described as Gaussian white noise. A likely explanation for the random noise in the force signals is that it is due to the random structure of the grinding wheel causing many randomly distributed impacts between the tool and the wheel material. The maximum RMS amplitudes were 110.1 N, 179.2 N, and 126.8 N in the normal, tangential and axial directions, respectively. The RMS amplitudes in all three directions were shown to increase with increasing groove depth.

A significant conclusion that can be drawn from these experiments is that it is beneficial for a grooving device to be capable of creating grooves using multiple shallow cuts at an increasing depth into the surface of the wheel instead of removing the entire groove depth in a single cut. A device with this re-grooving capability could use smaller actuators and lighter components, resulting in a more cost-effective and compact device. Furthermore, creating grooves using multiple shallow cuts could reduce the static deflection during the grooving process due to the decreased process forces, thereby reducing potential geometric errors introduced by the static deflection of the device.

Some additional research could be performed to investigate whether the geometry of the cutting tool affects the grooving forces independently of the groove cross-sectional area. The effect of higher wheel velocities on grooving forces could also be investigated. The wheel velocities used in the experiments in this section were an order of magnitude smaller than the wheel velocities normally used for single-point dressing of grinding wheels. The effect of a higher dressing feed during the grooving process on the grooving forces could also be investigated. Finally, another possible area of investigation would be the effect of coolant on the grooving forces.

4.2 Design Requirements

Several design requirements were determined for a multi-axis grinding wheel grooving device that can create a variety of groove patterns on a variety of grinding wheel profiles.

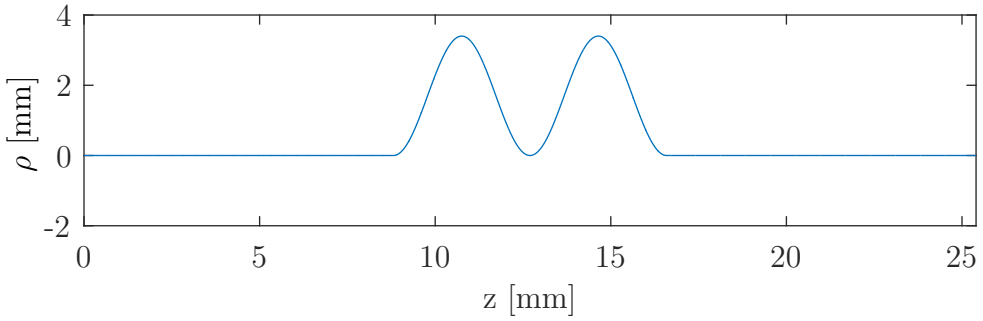

Figure 4.5: Design-case workpiece profile used to determine kinematic requirements.

4.2.1 Kinematic Requirements

The kinematic requirements were determined based on a desired profile shape that the grooving device should be able to create and groove. The profile was selected because the author had access to a roller dresser that could create this profile. The design-case profile is shown in Figure 4.5.

The profile in Figure 4.5 is a sinusoid with a peak-to-peak amplitude of 3.2 mm and a wavelength of 3.5 mm.

1. The grooving device must be capable of producing a helical groove with a constant depth on the profile given in Figure 4.5.

   The purpose of the project is to design a device that can create grooves of constant depth as it "follows" the shape of the profile. As was discussed in the literature review, the effects of groove depth on wheel performance are presently unknown, therefore the design should be able to produce the grooves at a constant depth to better control the experimental conditions during grooved profile grinding. Helical grooves are the simplest groove geometry and the most common in the literature, which is why that particular geometry was chosen. However, it would be desirable to have a device that could create other groove geometries as well, to open future avenues of grooved wheel research.

2. The device must have a stroke length (maximum displacement) of at least 3.5 mm in the vertical direction.

   The stroke length must be larger than the design profile height of 3.2 mm. A

larger stroke length in the vertical direction is desirable because it would allow for a larger variety of profile shapes.

3. The device must have a stroke length at least 30 mm in the horizontal direction.

   The horizontal stroke length must be larger than the width of the grinding wheels commonly used in the author's grinding machine (26.7 mm). Additional stroke length to accelerate and decelerate will also be necessary. A larger stroke length in the horizontal direction is desirable because it would allow for a larger variety of wheel widths.

4. The device must be capable of creating grooves with a minimum groove depth of 100 µm a maximum groove depth of 500 µm to within an accuracy of ±10 µm.

   The requirements for the groove depths were chosen based on the groove depths seen in the literature for a single-point diamond grooving device. The accuracy was selected to be one tenth of the smallest required groove depth. The device is intended to be a grooving device, *not* a profiling device. For a profiling device, the maximum positioning errors would need to meet tolerances of 1 µm or less.

5. The grooving device must be capable of producing a helical groove on the profile given in Figure 4.5 with a maximum lead of $L_g = 0.010$ m/rev and a helical groove on a flat wheel with a maximum lead of $L_g = 0.100$ m/rev.

   The grooving device must be able to achieve the desired groove geometry by cutting a wheel rotating at $\omega_s = 16.23\ \mathrm{rad\,s^{-1}}$ (150 rpm). This angular velocity is close to the value used by Mohamed *et al.* for a single-point grooving device [18]. The wheel speed, profile shape and desired groove lead can then be used to calculate the necessary actuator speeds as described in Chapter 2. Profiles with larger slopes will require higher vertical actuator velocities. That is why two different values are specified: the upper limit of groove leads for a profile wheel and the upper limit of groove leads for a flat wheel.

   The kinematics of the conditions described in the above requirement were simulated in MATLAB[1]. The code is provided in Appendix A. From the simulation it was determined that the grooving device must be able to achieve a maximum speed in the y–axis direction of 38.1 mm/s and a maximum acceleration

in the y–axis direction of 1.712 m/s^2. The device must also be able to achieve a maximum speed in the z–axis direction of 0.260 mm/s.

6. The device must be capable of re-tracing an existing groove geometry. This capability would allow grooves to be re-generated on a grinding wheel without first removing the existing grooves. It would also allow deep grooves to be cut incrementally. The re-grooving capability is one of the primary advantages of the single-point servo grooving method. Therefore, the grooving device must be designed with the appropriate instrumentation and control systems to be capable of accurately synchronizing its movement with the rotation of the grinding wheel.

4.2.2 Load Requirements

The load requirements were selected based on the forces measured in Section 4.1.

1. The vertical axis actuator must be capable of providing 360 N of force at its rated speed.

   The load requirement for the vertical actuator was chosen to be the sum of the maximum RMS and average normal forces, multiplied by a safety factor of two to account for the inertial and friction loads of the final design. The motor will be able to supply peak torques above its rated torque for short periods of time that should be able to account for the large force vibration peaks seen in the experiments in Section 4.1.

2. The horizontal axis actuator must be capable of providing 250 N of force at its rated speed.

   Similar to the vertical actuator, the load requirement for the horizontal actuator was chosen to be the sum of the maximum RMS and average axial forces, multiplied by a safety factor of two to account for the inertial and friction loads of the final design.

[1] ©The MathWorks, Inc. MATLAB and Simulink are registered trademarks of The MathWorks, Inc. See mathworks.com/trademarks for a list of additional trademarks. Other product or brand names may be trademarks or registered trademarks of their respective holders.

4.2.3 Other Requirements

Other requirements concerning the environmental conditions and space limitations inside of the grinding machine must also be taken into account.

1. The device must be capable of functioning in the presence of water/grinding lubricant mist and dust and particles from the grinding wheel.

   The inside of the grinding machine can be a harmful environment to various electrical and mechanical components. Components must be resistant to or unaffected by direct contact with the water-oil coolant mix, the coolant mist inside the machine, and metal dust or abrasive dust from the machining process. Any components that cannot withstand these conditions must be protected.

2. The grooving device must fit inside of a 400 mm $\times$ 400 mm $\times$ 200 mm volume.

   The device must fit inside of a relatively small envelope within the grinding machine so that it does not interfere with other operations. It must be possible to perform other grinding experiments while the grooving device is inside the machine.

3. The grooving device should be easily installed and removed from the grinding machine.

   An installation process that takes several hours will be considered "easily installed" while a removal process that takes less than one hour shall be considered "easily removed". The grooving device must be easily removed in case operations must be performed within the machine that cannot be performed while the grooving device is inside of the machine. This is a low priority requirement compared to the other requirements, however, it was still important to be considered during the design of the grooving device.

4.3 Final Design

A CAD model of the final design is shown in Figure 4.6. Two perpendicular linear stages driven by DC servomotors actuate a single-point diamond dressing tool within a planar workspace. The servomotor used to actuate the vertical stage drives the

stage through a timing belt and pulley system. The servomotor used to actuate the horizontal stage is directly connected to the stage. A structural tower base is used to mount the grooving device inside the grinding machine.

An acronym name was given to the device: **E**nhanced **D**ressing and **G**rooving **R**obot, or *EDGR* (pronounced "Edgar") for short. The acronym allows the device to be referred to by a shorter name than the "multi-axis grooving device". A photograph of *EDGR* is shown in Figure 4.7.

4.3.1 Mechanical Equipment

In this section the mechanical equipment selected for use in the final design of *EDGR* is presented. The specifications and the justifications for the selections are detailed for each part of the device.

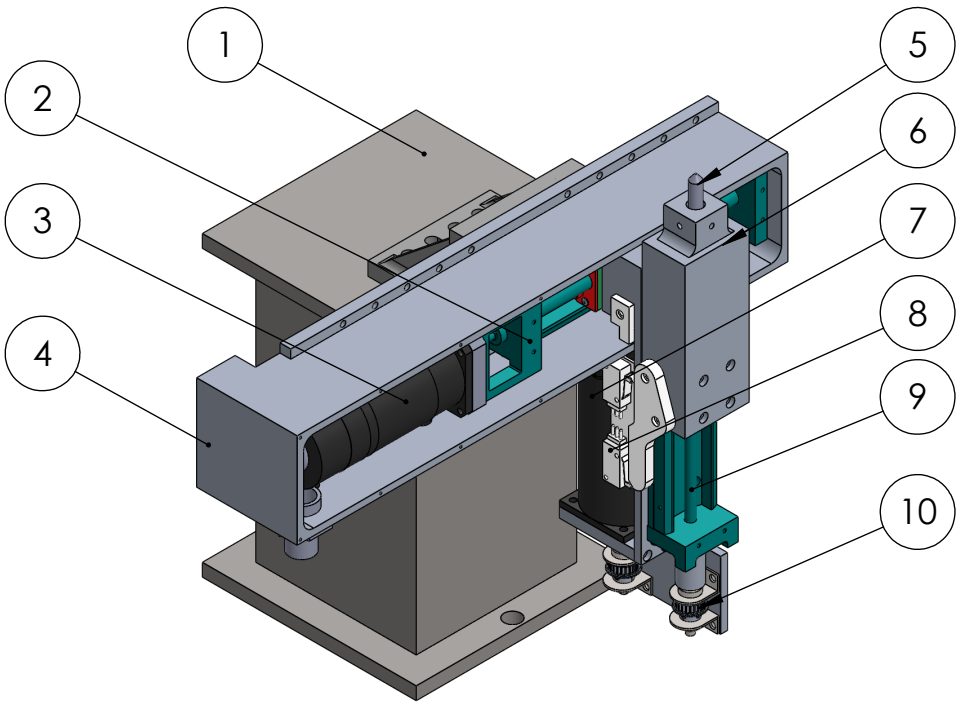

Figure 4.6: CAD model of the grooving device with colour-coded components. (1) Structural tower; (2) Horizontal stage; (3) DC Servomotor; (4) Horizontal stage enclosure; (5) Single-point diamond dressing tool; (6) Dressing tool holder; (7) Limit switches and cam; (8) DC Servomotor; (9) Vertical stage; (10) Belt and pulley system (belt not shown).

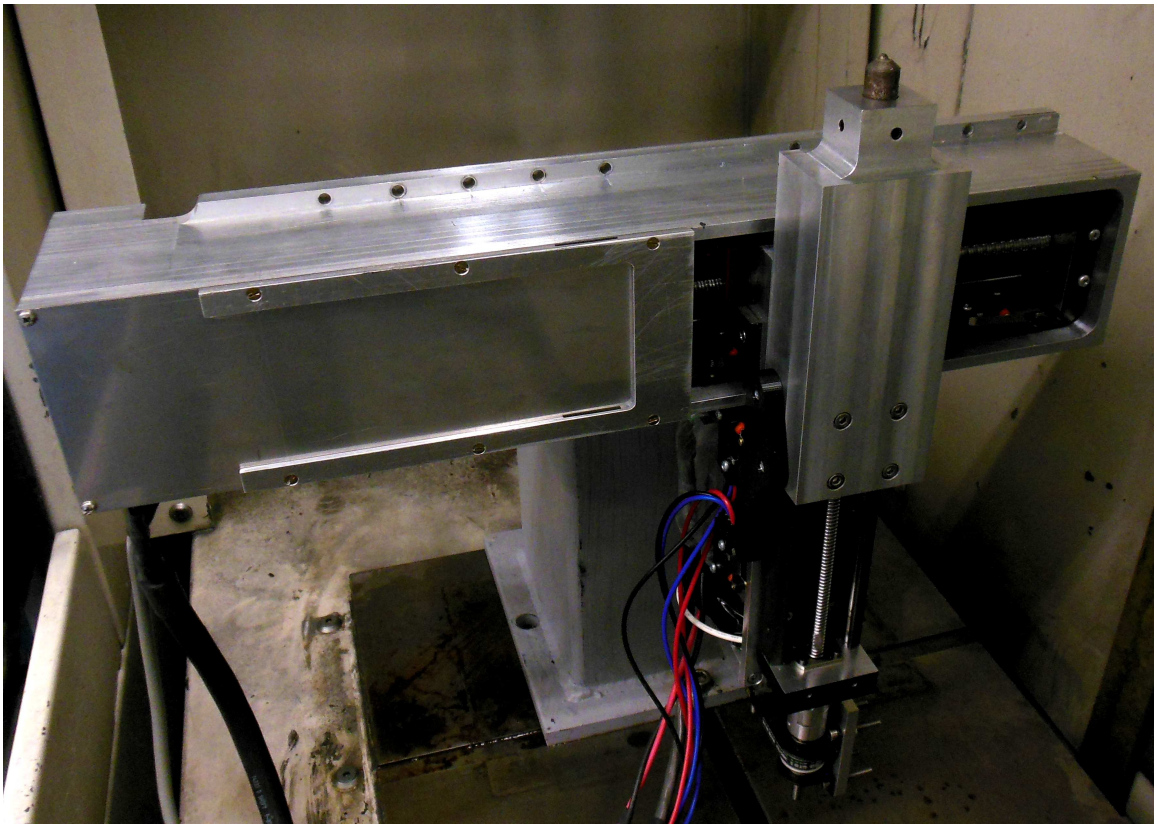

Figure 4.7: A photograph of EDGR inside the grinding machine, without its waterproof protective cover.

Linear stages

A HIWIN® KK6005P–200A1–F0 was used for the horizontal linear stage. This stage has a rail length of 150 mm and has a ballscrew with a lead of 5 mm/rev with a rated accuracy of ±3 µm. A HIWIN® KK5002P–200A1–F0 was used for the vertical linear stage. This stage has a rail length of 200 mm and has a ballscrew with a lead of 2 mm/rev with a rated accuracy of ±3 µm. Both stages have force load ratings well above the expected forces for this application. The load ratings of most concern are the moment ratings. As other components were sized, the moment loads on the stages were updated to include weight and inertial forces. These loads were verified to meet a safety factor of at least 2.

Motors, Power Supplies and Motor Controller

A brushed DC Servomotor from Dynetic Systems® (MS2215-38/GI392) with a US Digital® optical encoder (E5–1250–IE–D–E–G–3) was used to drive the horizontal linear stage. A brushed DC motor from Automation Technologies Inc.® with a US Digital® optical encoder (E5–360–250–IE–D–H–G–3) was used to drive the vertical linear stage. The specifications of the motors are given in Table 4.1.

No rated speed was provided by the manufacturer for the KL23–130–60; however, the maximum speed was 4700 rpm which exceeds the required speed by a significant enough margin that it was determined to meet the requirements. The motors were sized given the expected loads and the fact that a leadscrew is used to convert the rotary motion to linear motion. The motors were sized using a safety factor of four to account for the large peak forces during grooving.

An AnTek® PS-4N38 power supply was selected for the horizontal motor. It can

Property		Horizontal Motor	Vertical Motor
Positioning Resolution	[°]	0.288	0.25
Voltage	[V]	38.0	60.0
Rated Current	[A]	2.9	3.5
Rated Torque	[N m]	0.155	0.353
Rated Speed	[rpm]	5700	–

Table 4.1: Selected motor specifications.

supply 10.5 A at 38 V. An AnTek® PS-10N63 power supply was selected for the vertical motor. It can supply 15.9 A at 63 V.

A Dynomotion® KFLOP motion controller with a SnapAmp Multi-Purpose Amplifier was selected for the motor controller. The KFLOP is intended for use in CNC applications, can be programmed using C or G-Code programming languages and comes packaged with a custom graphical user interface, KMotion. The servo loop executes at 1100 Hz, significantly faster than should be necessary for this application.

Timing Belt Drive

Due to the maximum height requirement of the design, Motor #2 could not be directly connected to the lead screw shaft of Stage #2. Instead, a drive system had to be developed to transfer power between the two parallel shafts. Specifically, a 3 mm pitch GT®2 belt from Stock Drive Products was selected with two identical pulleys, each with 22 teeth. The purpose of the pulley system is to transmit power from the motor to the lead screw. Due to the motor size, no gear ratio was necessary.

The two pulleys are mounted on two parallel $\frac{1}{4}$ inch 416 stainless steel shafts. These shafts are mounted on two flange-mounted ball bearings. The motor shaft is connected to the first steel shaft with a rigid shaft coupling and the lead screw shaft is connected to the other steel shaft with a flexible spider coupling. The spider coupling is designed to handle misalignment between the two shafts and attenuate vibrations while having a negligible amount of backlash.

The belt system is designed to transmit a rated torque of 0.945 N m at a speed of 1200 rpm. The belt design has a rated position error of ± 0.03 mm. For the selected pulley pitch diameter of 21.01 mm and the given lead of the vertical stage, the theoretical vertical positioning error due to the timing belt is ± 1 µm.

4.3.2 Electrical System

A diagram describing the components of the electrical system is shown in Figure 4.8.

The index pulse from the spindle encoder of the grinding machine (1) is monitored by the KFLOP control board and is used to synchronize the motion of *EDGR* with the grinding wheel position. There are many sources of electromagnetic interference present during operation of the grinding machine that make the spindle encoder index

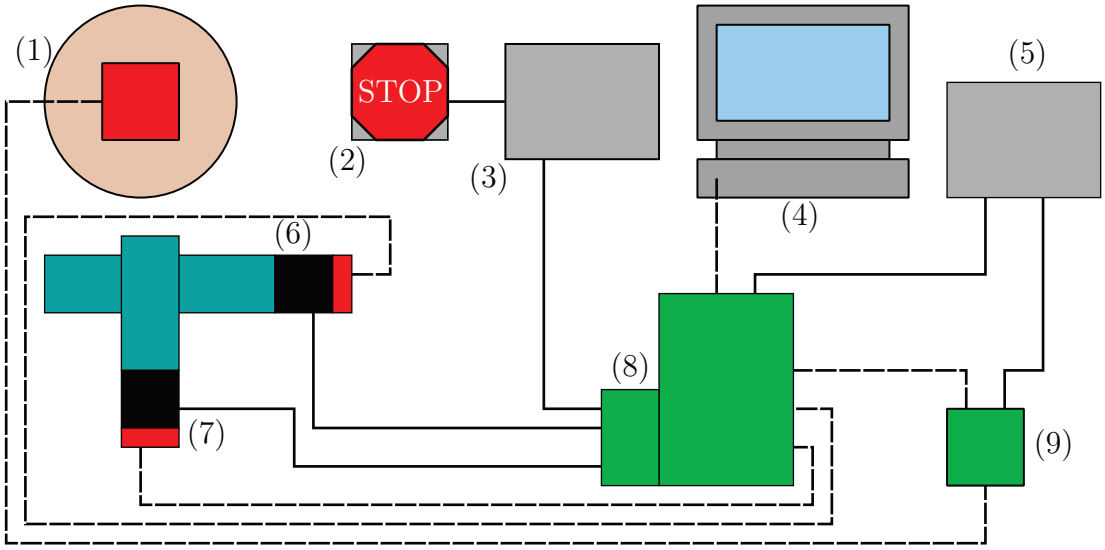

Figure 4.8: Diagram describing the electrical system of *EDGR*. (1) Grinding machine spindle encoder; (2) Emergency off switch; (3) DC Motor Power Supplies; (4) Lab computer; (5) Control board/electronics power supply; (6) Horizontal stage, motor and encoder; (7) Vertical stage, motor and encoder; (8) KFLOP control board; (9) Instrumentation amplifier.

pulse difficult to detect. A Texas Instruments INA-128P instrumentation amplifier (9) is used to reduce the common-mode noise in the wheel encoder signal such that it can be read by the KFLOP (8). An electrical safety switch with a built-in circuit breaker (2) is incorporated into the DC motor power supply enclosure (3). The KFLOP controls the current output to the servomotors (6) and (7) using pulse-width-modulation. Commands can be given to the KFLOP through the lab computer (4), or written as C or G code, then compiled and downloaded to the KFLOP for offline execution. The lab computer can also give real-time feedback on the KFLOP temperature, motor positions and power supply currents. A PC power supply (5) is used to provide power to the KFLOP and the instrumentation amplifier.

4.3.3 Control System

Each of *EDGR*'s two axes has an independent control system described by the block diagram in Figure 4.9. The block diagram describes the standard continuous-time control functionality available from the KFLOP.

For each axis there is a feed-forward and a feedback loop. KFLOP calculates the

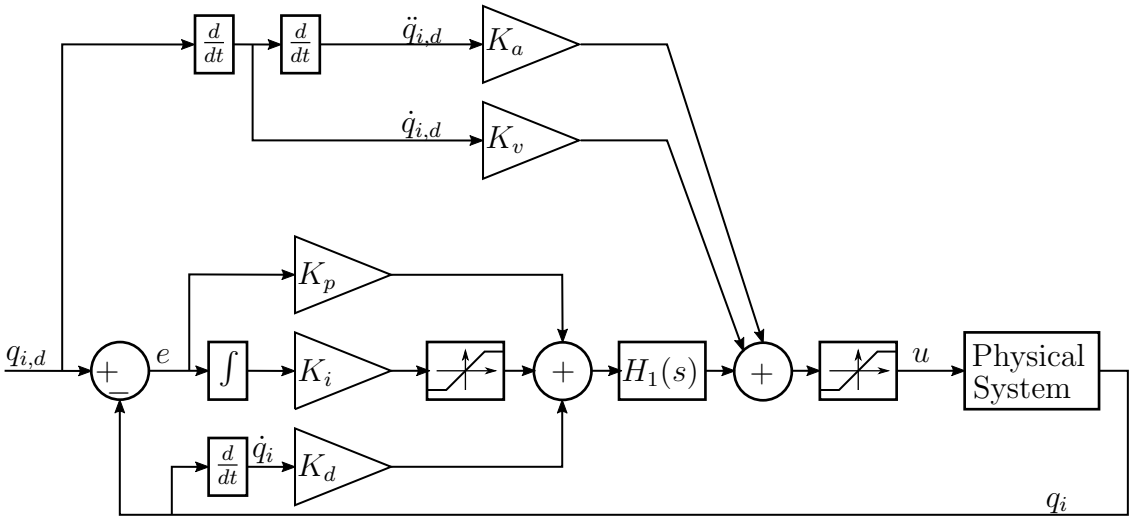

Figure 4.9: Control system block diagram of one of *EDGR*'s axes.

Property	Horizontal Axis	Vertical Axis
K_v	0.010	0.030
K_a	0.00003	0.0001
K_p	2	10
K_i	0.02	0.02
K_d	110	300
Integrator Saturation	100	100
Output Saturation	300	300
Low pass cut-off [Hz]	250	340

Table 4.2: Control system gains and other values.

error e between the calculated desired joint value in encoder counts $q_{i,d}$ and actual measured joint value q_i in encoder counts. A first-order low-pass filter $H_1(s)$ is applied to the sum of the output from the P, I and D gains before they are added to the outputs from the feed-forward loop. Saturation limits are applied to the integrator output and the total output. The output u from the system is pulse-width-modulated counts per cycle, which is proportional to the current sent to the motor. Table 4.2 provides the selected values for the control system gains, saturation limits, and filter cutoff frequencies for the horizontal and vertical axes.

The P, I and D gains were tuned manually for each axis to achieve minimum overshoot given the desired trajectories shown in Figures 4.10 and 4.11 with no-load

conditions. This trajectory was chosen because it is equivalent to a rapid move (G Code `G00`) across approximately the entire stroke for each axis, achieving maximum accelerations and velocities. These accelerations and velocities are higher than what would be expected under normal operating conditions under load. The feed-forward gains were then tuned to eliminate the steady-state error during the ramp sections of the desired trajectories and to minimize the error spikes during the periods of acceleration during the motion. The low-pass filter was necessary to filter out the noise introduced by the derivative term in the feedback loop. This noise is due to the quantization in the measured joint value signal q resulting in instances of measured near-infinite velocities. The cut-off frequencies of the filters for each axis were selected based on the maximum velocity sinusoidal trajectory that each axis could be required to perform.

Figures 4.10 and 4.11 show the unloaded performance of the horizontal and vertical axes, respectively, undergoing maximum accelerations and velocities. During the periods of maximum acceleration, the error between the desired and actual positions shows a significant spike. The peak error reaches 27 µm for the horizontal axis and 26 µm for the vertical axis. The root-mean-square error (RMSE) during the motion is 2.9 µm for the horizontal axis and 3.0 µm for the vertical axis. The required maximum peak error is ±10 µm, which is clearly exceeded during the periods of maximum acceleration. However, as was previously stated, the maximum accelerations during the tuning tests exceeded the expected accelerations during regular operation. More testing is required to verify whether *EDGR* meets its accuracy requirements.

4.4 Design Accuracy Validation

The results from the control system tuning indicated that *EDGR* failed to meet its accuracy requirement of a maximum error of ±20 µm for a given profile. However, the control system tuning was not performed under expected operating conditions. In this section several tests are described that were used to validate *EDGR*'s accuracy under expected operating conditions and loads. A novel kinematic error compensation technique is used to account for alignment errors between *EDGR* and the grinding machine. This compensation technique is described in detail in Chapter 5.

It is difficult to measure the surface of a grinding wheel precisely; therefore, these

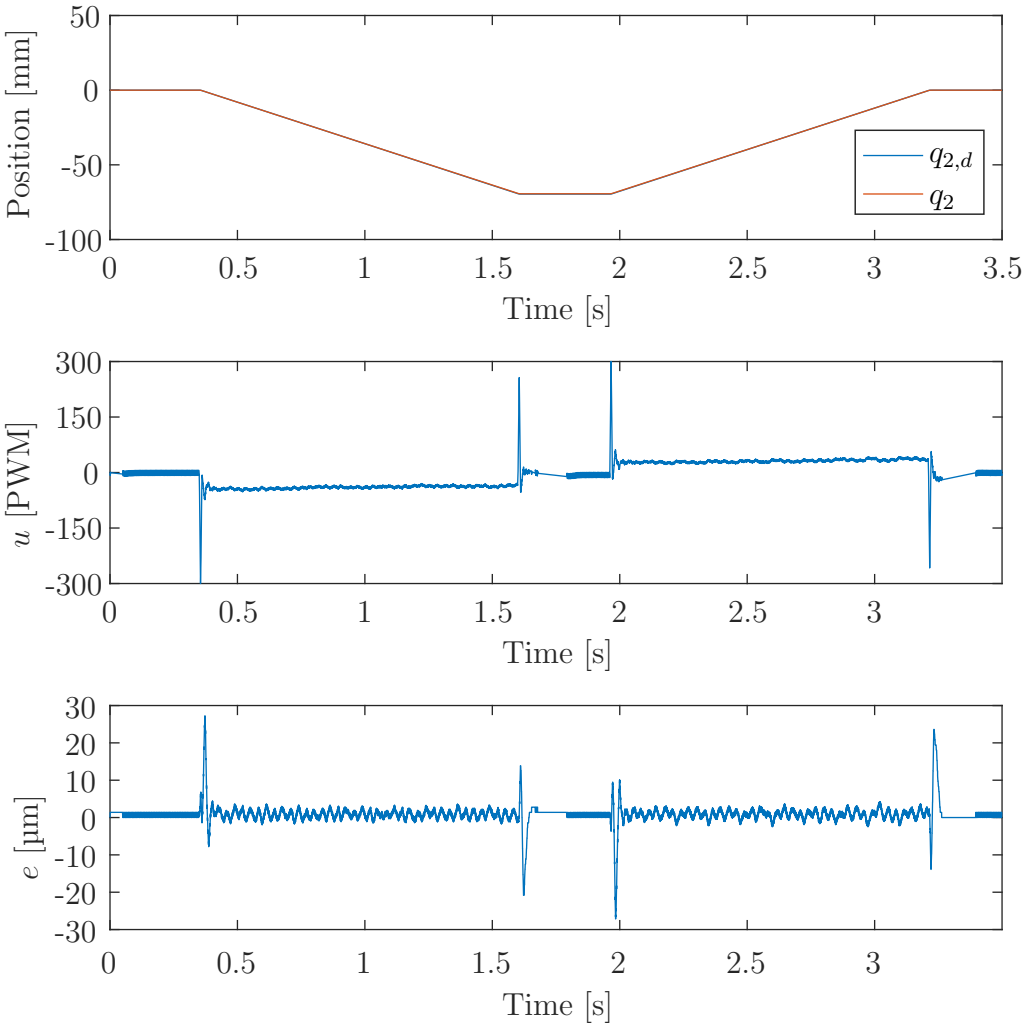

Figure 4.10: Horizontal axis, tuned control system performance.

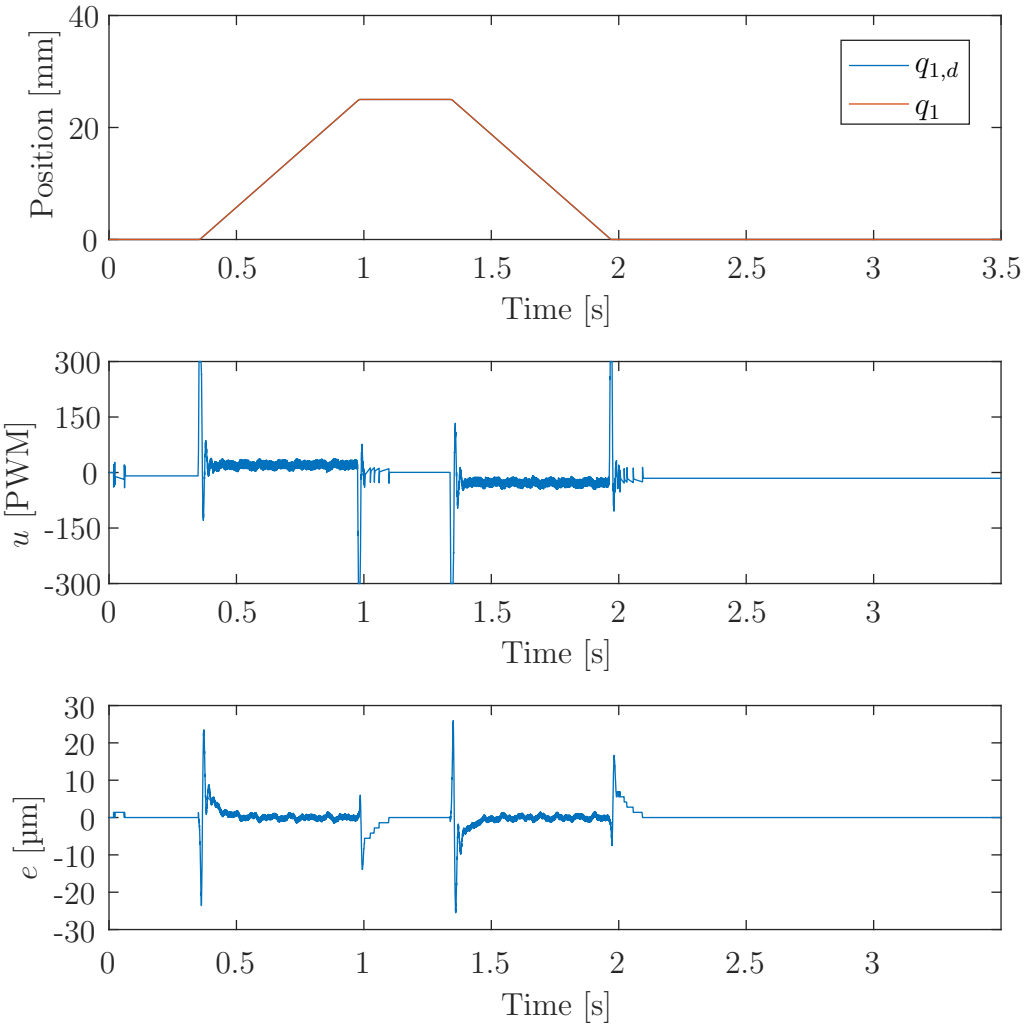

Figure 4.11: Vertical axis, tuned control system performance.

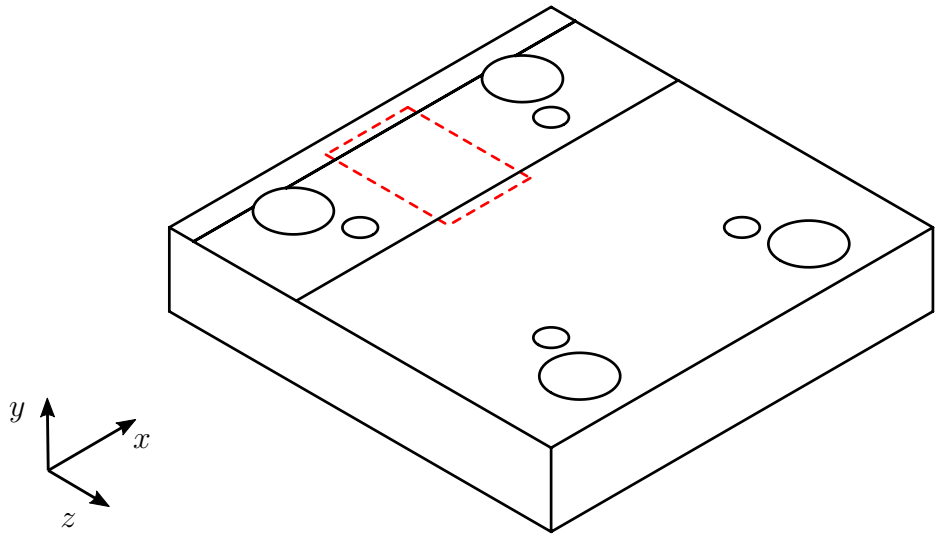

Figure 4.12: Diagram of a 1018 steel specimen showing the plunge-ground area. The grinding machine coordinate system is shown in the bottom-left corner. The dashed line indicates the scanned area.

experiments were designed to provide indirect measurements of the wheel surface by measuring a workpiece ground using the wheel. *EDGR* was used to profile the grinding wheel and then the profile of the wheel was determined by measuring the profile left on the workpiece after grinding. It is important to note that *EDGR* is not intended to be a profiling device, which would require much finer positional tolerances. However, profiling a workpiece was determined to be the most reliable way to measure *EDGR*'s positional accuracy.

4.4.1 Dressing and Truing a Flat Wheel

The first test performed to validate EDGR's performance was to dress and true a flat grinding wheel. A 1018 steel workpiece was ground flat with a grinding wheel that was dressed and trued on the regular grinding machine dressing tool. The grinding wheel was then dressed and trued using EDGR. The grinding wheel was then used to plunge-grind a single wheel-width along the workpiece as shown in Figure 4.12.

The workpiece was then removed from the grinding machine and scanned with a Nanovea CHR 150 OP 1000 Profilometer. An area of 20 mm by 35 mm was scanned with a 10 µm by 100 µm grid resolution. A 3D mesh plot of the surface scan was

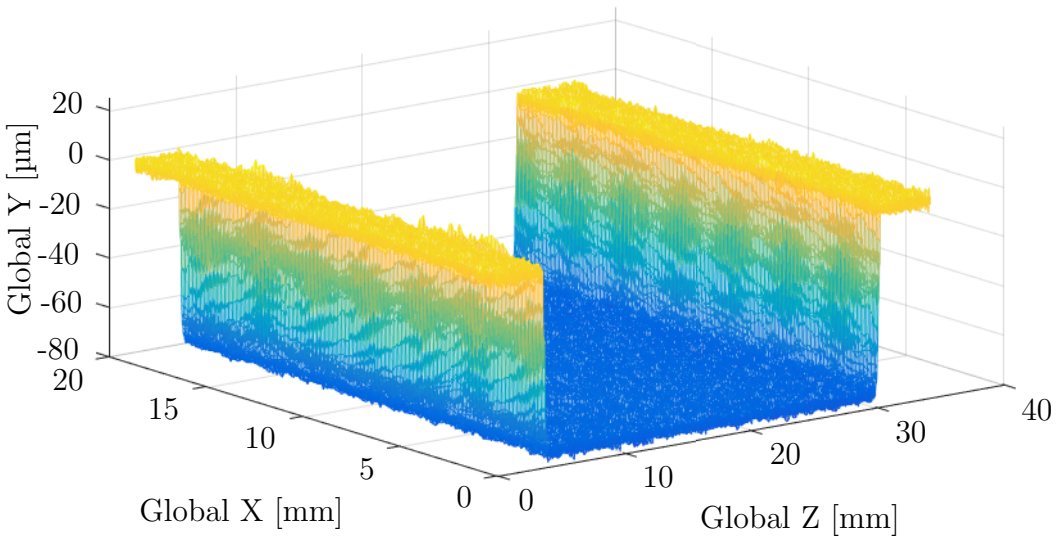

Figure 4.13: 3D profilometer scan of the flat workpiece surface.

generated and is shown in Figure 4.13.

The top flat surface (yellow in Figure 4.13) was used as a reference to calculate a flat plane of best fit for the plunge-ground surface (blue in Figure 4.13). The root-mean-squared error of the measured data from this best fit plane was 1.45 µm. The average slope of the plunge-ground surface relative to the reference surface was 0.067 $\mu m\,mm^{-1}$ (1.70 µm/in). The maximum error was ±0.89 µm over the entire profile, well within the required ±10 µm range.

4.4.2 Simple Profile

Once EDGR's capability to true a flat wheel was demonstrated, the next test was to validate its accuracy in creating a profiled wheel. A simple profile was selected to validate EDGR's performance. The profile is shown in Figure 4.14.

The wheel was profiled using EDGR. The wheel was then used to grind a workpiece with a thickness of 19.05 mm and a length of 101.6 mm. This workpiece was then scanned with the profilomter. The measurement range of the profilometer is only 1.0 mm, while the profile has a height of 5.08 mm. Therefore a custom holder was designed to allow the workpiece to be scanned with the profilometer perpendicular to the inclined surface of the profile as shown in Figure 4.15. An area of 5 mm by 20 mm was scanned with a 2 µm by 2 µm grid resolution. A 3D mesh of the scanned

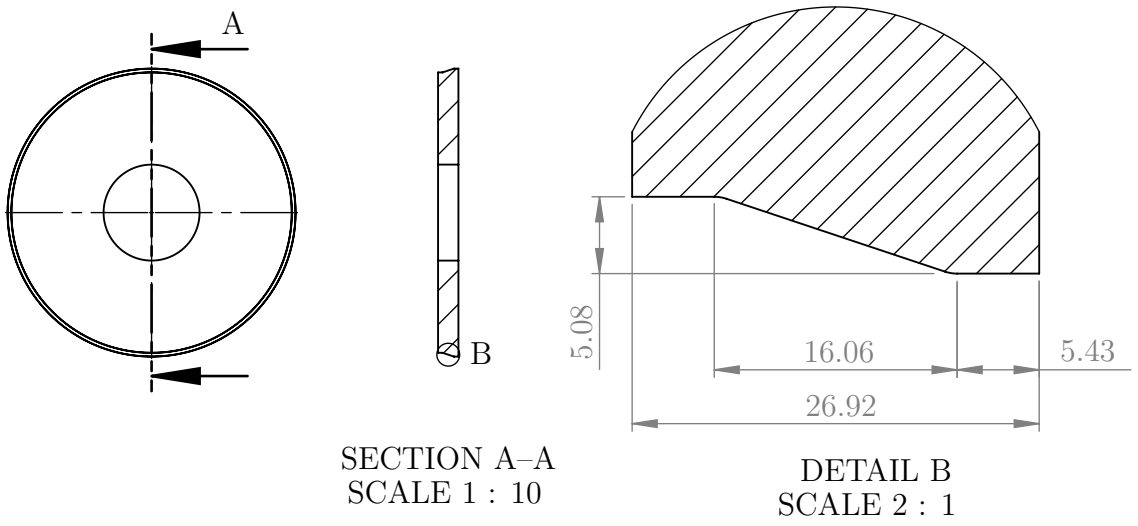

Figure 4.14: Engineering drawing of the simple wheel profile used to validate EDGR's accuracy.

surface was generated and is shown in Figure 4.16.

The scanned surface was then rotated to the actual grinding machine coordinate system and compared to the desired profile. The desired profile, the profile based on the recorded encoder counts and the actual measured profile are plotted in Figure 4.17(a). There is no visible difference between the two profiles at the given scale. Figure 4.17(b) shows the error between the measured profile and the actual profile (total error) as well as the error between the desired profile and the profile that would result from the recorded encoder counts (control system error).

Unfortunately, the maximum total measured error in Figure 4.17 exceeds the requirement of ±10 µm. The root-mean square error for the entire scanned surface from the desired profile was 4.3 µm. It is important to note that the error of the control system (encoder error) is very small, within one encoder count (approx. 1 µm). Therefore, the control system is clearly not the source of the large error peaks seen in the plot. There are multiple possible sources of this error. Firstly, there could be static deflections in the tool and in *EDGR*'s structure. As the tool makes contact with the workpiece, the tool deflects due to the cutting forces. The largest errors are present in the corners of the workpiece, where the force on the tool would be changing directions as it transitions from the flat section to the inclined section of the profile.

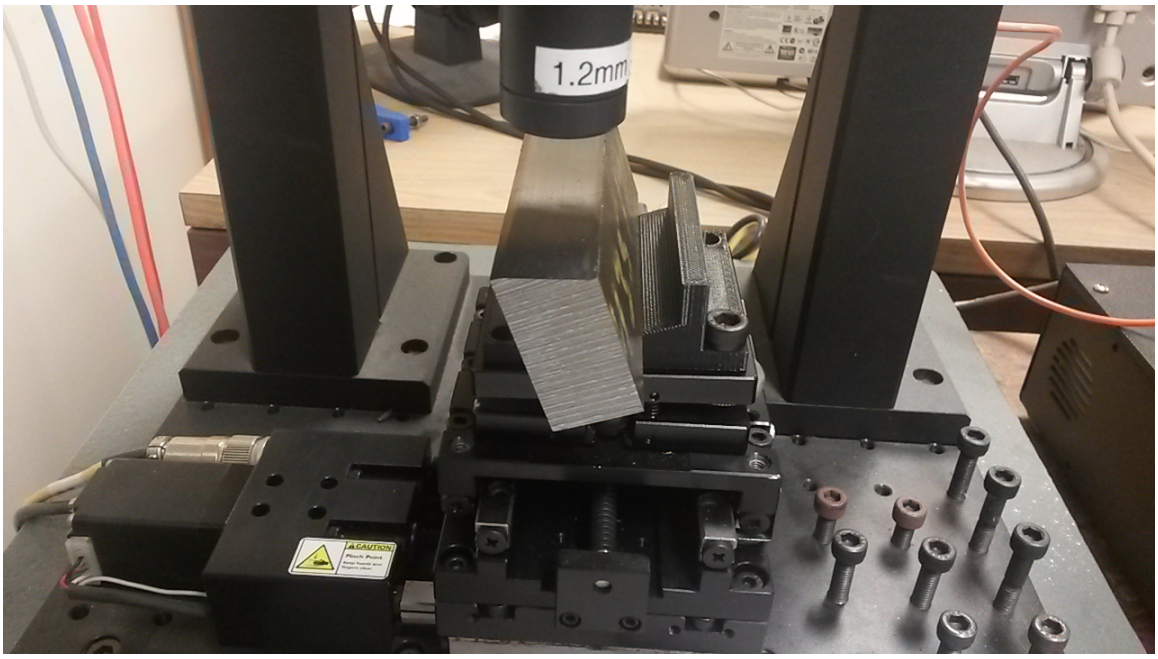

Figure 4.15: Photograph showing the custom workpiece holder used to scan the workpiece perpendicular to its inclined surface.

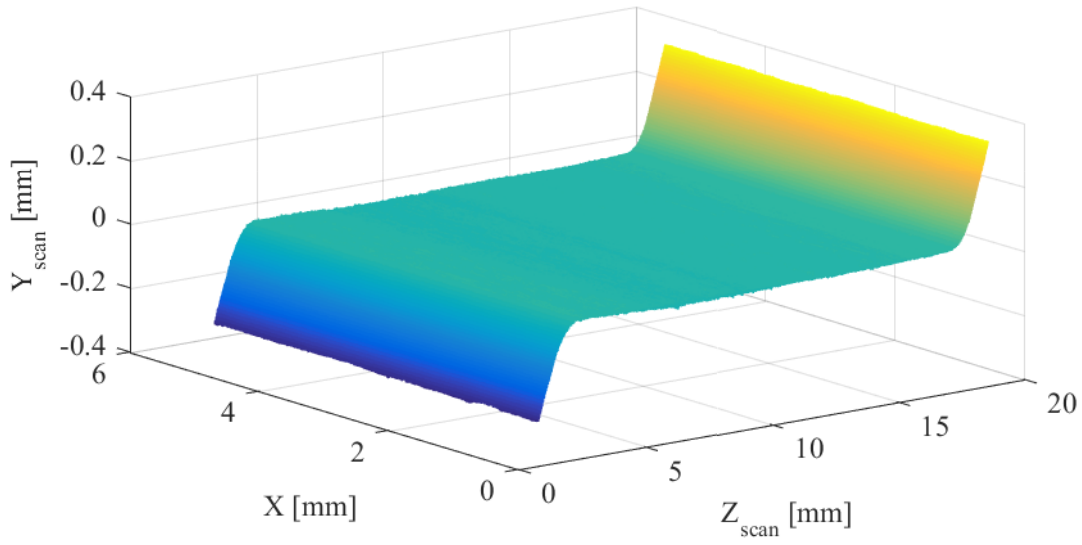

Figure 4.16: 3D Scan of the simple profile in rotated coordinates with the scan depth perpendicular to the inclined surface of the profile. Y_{scan} and Z_{scan} are rotated by approximately -18° around the X axis from the Y and Z grinding machine axes.

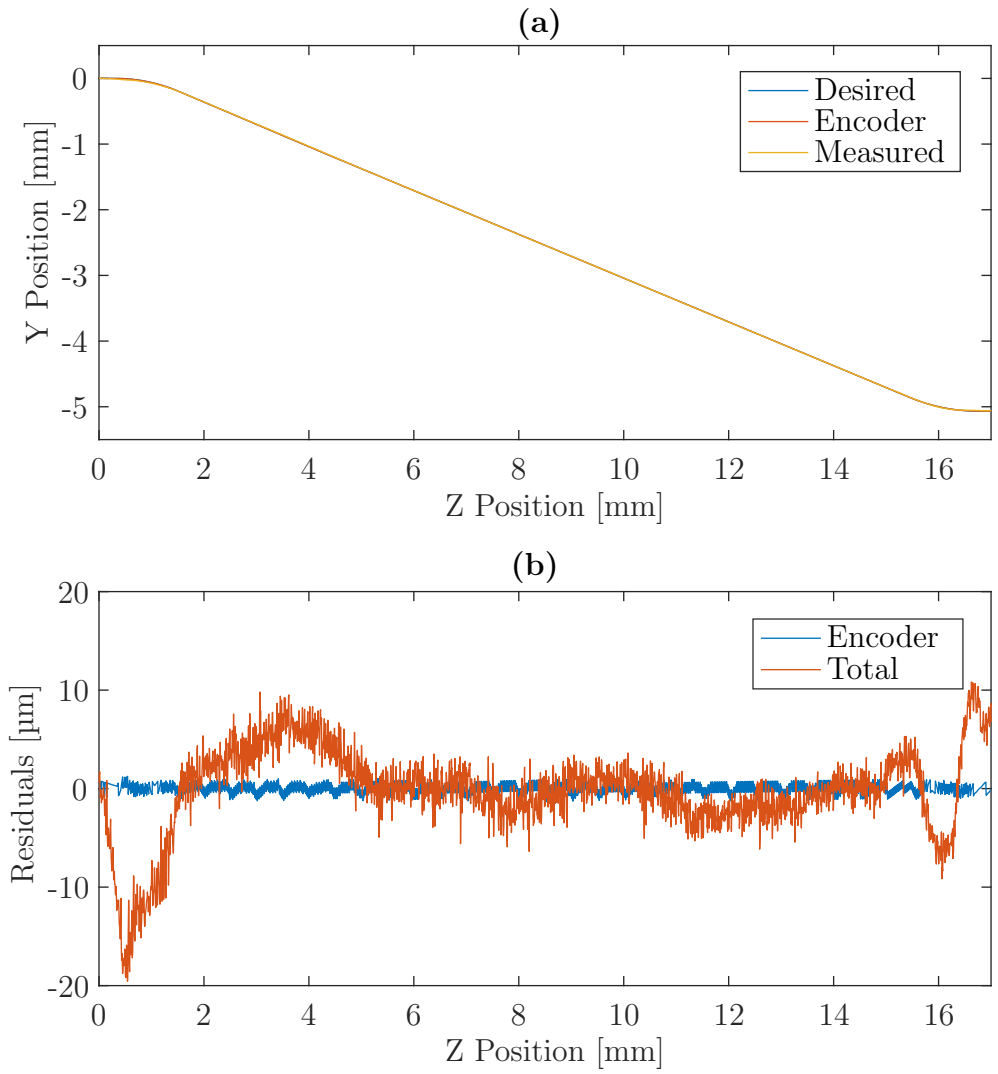

Figure 4.17: (a) Plot showing the desired profile based on the joint values commanded, the profile based on the measured encoder counts, and the actual profile based on the measured workpiece surface. (b) Figure showing the total error measured on the profile and the error that can be attributed to the encoder counts (control system error).

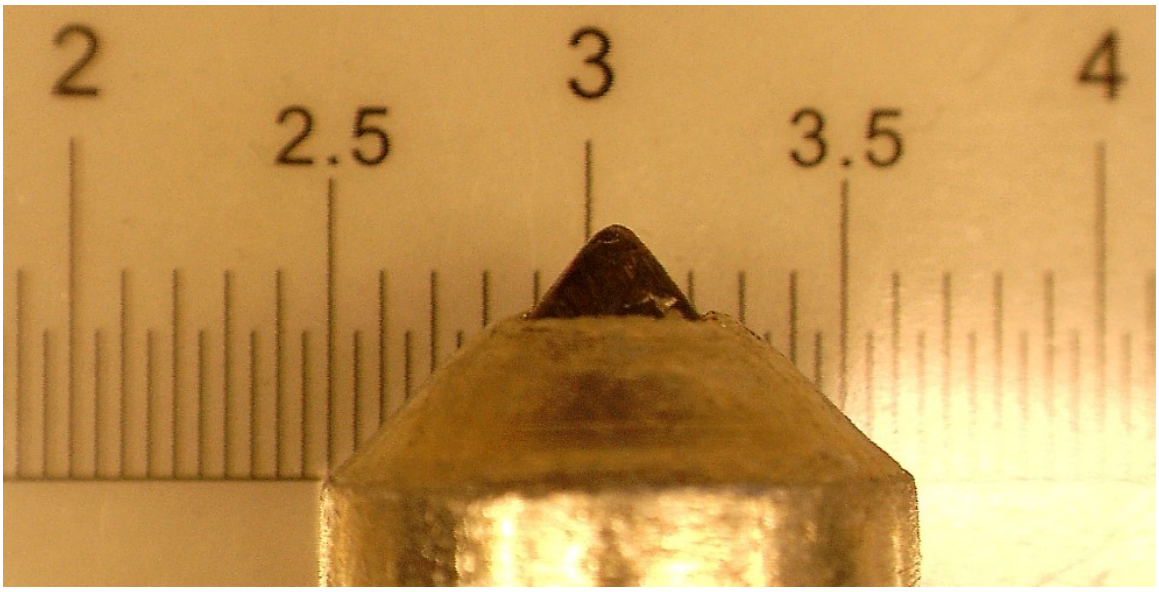

Figure 4.18: Photograph of the dressing tool used to profile the grinding wheel, before use.

Another source of error could be due to backlash or "play" in the vertical actuator system. The belt drive has minimal backlash, however, the specified value for its accuracy is ±1 µm. The accuracy of the vertical linear stage is listed as ±3 µm and the accuracy of its encoder is ±1.4 µm. If all of these errors were summed, which in practice would not be the case, there would be an upper limit error of ±5.4 µm. This conservative estimate of the theoretical error could account for the noise and some of the waviness present in the measured signal, but it does not account for the large peak errors, which far exceed 5.4 µm. The most likely source of error required some more analysis to determine. This analysis is outlined in the following paragraphs.

In Chapter 5, a kinematic error compensation algorithm is described in detail that calculates a tool path to correct for several factors, such as the alignment of *EDGR*'s axes with those of the grinding machine. One part of this algorithm compensates for the dressing tool geometry. As the dressing tool cuts the wheel the point of contact with the wheel will change depending on the slope of the profile and the shape of the tool. In order to compensate for the tool geometry, a photograph was taken of the tool with a microscope camera, shown in Figure 4.18. From this photograph, the tool shape was approximated with a parabolic segment and two straight-line segments.

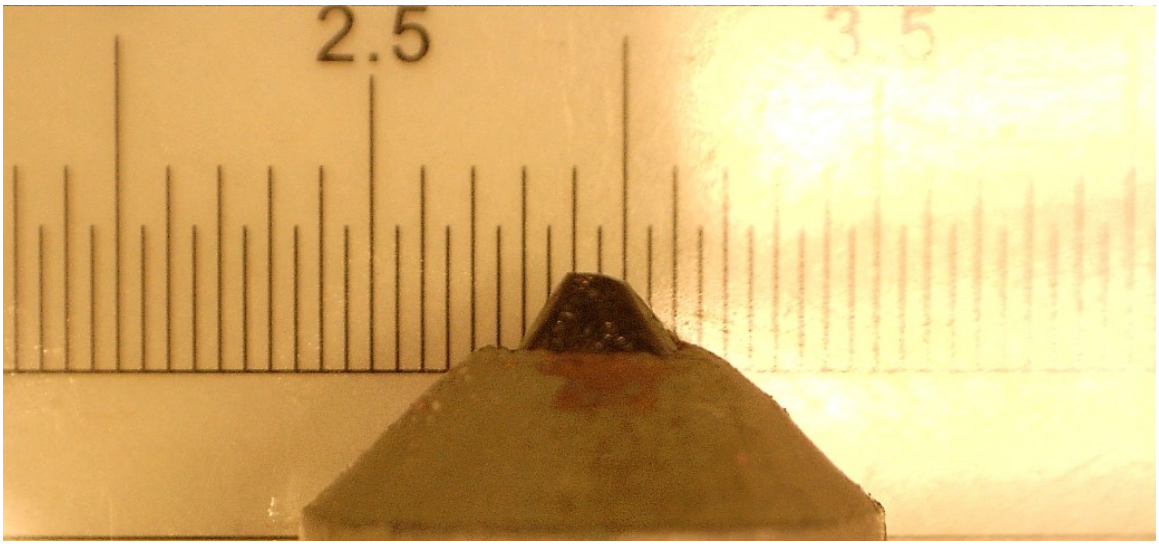

Figure 4.19: Photograph of the dressing tool used to profile the grinding wheel, after significant use.

The dressing tool pictured in Figure 4.18 was used remove large amounts of material to form the profile from a flat wheel, as well as dress the wheel between many preliminary profile grinding experiments, before it was used to create the profile used to validate *EDGR*'s accuracy. In that time, the tool wore significantly, however, the tool correction data was not updated in the kinematic error compensation algorithm. Figure 4.19 shows a photograph taken of the dressing tool after it had been used to create the validation profile.

Figure 4.20 shows the approximations of the tool geometry for the new tool and the worn tool. For the tool geometry before wear occurred, as the tool enters the corner of the profile, the point of contact between the tool and the grinding wheel gradually moves along the tool geometry as the slope of the profile changes. The changing point of contact is illustrated in Figure 4.21(a). However, for the worn tool there is a single point of contact between the wheel and the tool: at the newly worn corner as shown in Figure 4.21(b).

A possible explanation for the large profile errors seen in Figure 4.17 may be the difference in tool geometry due to tool wear. Using the recorded encoder counts from the validation experiment, the profile generated by a new tool and a worn tool were calculated. The "new tool" profile was then shifted vertically and horizontally until the sum of squared errors between the two profiles was minimized, mimicking the

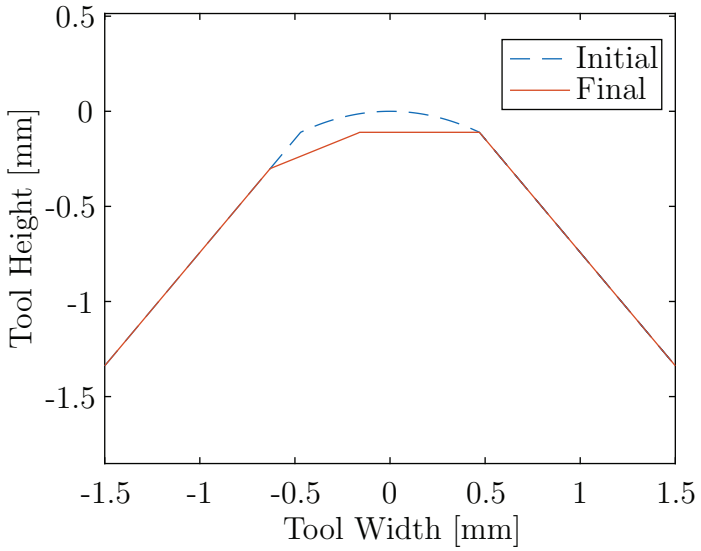

Figure 4.20: Approximate geometry of the dressing tool before (dashed line) and after (solid line) significant tool wear.

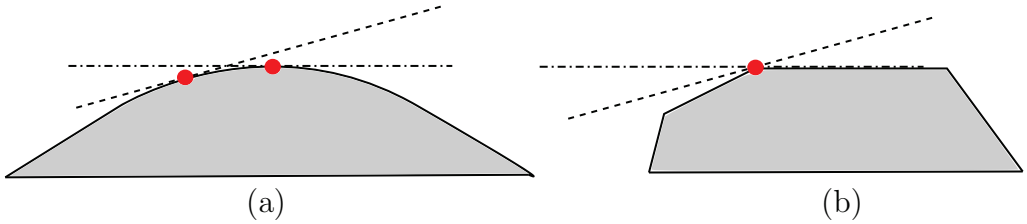

Figure 4.21: Diagram illustrating the changing point of contact for a continuous/new (a) tool and a discontinuous/worn (b) tool geometry. The dashed lines indicate two different possible grinding wheel slopes. The red dots indicate the point of contact between the tool and the grinding wheel depending on the slope of the wheel profile.

error plot given in Figure 4.17(b). The results for the new and worn tool profiles are shown in Figure 4.22.

Similar to Figure 4.17(a), there is no discernible difference between the two profiles at the macroscopic scale in Figure 4.22(a). Furthermore, the residuals in Figure 4.22(b) show similar features to the residuals plot for Figure 4.17(b). The features of interest are indicated with Roman numerals. In both plots there are error spikes in the corners of the profile, (i) and (iv). The error spikes are due to the changing point of contact for the "new" tool differing from the fixed point of contact for the "worn" tool. The peak error at (i) matches the error seen in Figure 4.17 more closely than the peak error at (ii). The first peak has a magnitude of 15.1 µm for Figure 4.22(b) compared to 19.7 µm in 4.17(b). The second peak has a magnitude of 14.9 µm in Figure 4.22(b) versus a magnitude of 9.1 µm in Figure 4.17. The difference between the actual measured workpiece error peaks and the simulated worn tool error peaks are within the ±5.4 µm theoretical error listed previously.

The first error peak is followed by a section of positive error, (ii). This error is due in part to the different contact positions between the tools, but it is caused by the G Code interpreter used by the KFLOP. It approximates points as belonging to a straight line within a certain tolerance, in this case ±3 µm, and it therefore continued the tangency from the rounded corner at a slightly shallower slope than desired. At a z position of approximately 4 mm the KFLOP corrects its trajectory to the desired slope.

The last point of interest is the relatively small error (iii) between the two error peaks. In absolute coordinates the profiles have a vertical and horizontal offset between them. However, there is no way to measure the absolute profile coordinates once the workpiece has been removed from the grinding machine. Instead the profiles were shifted in the z and y directions until the sum of squared errors between them was minimized. The same operation was performed on the data in Figure 4.17. Therefore, the offset is eliminated between the two datasets along the majority of the inclined surface of the profile, in area (iii).

Figure 4.23 shows a comparison between the measured profile error and the estimated error due to the tool wear. From this figure it is clear that the tool wear is the most likely source of the large errors of the measured profile. The difference between

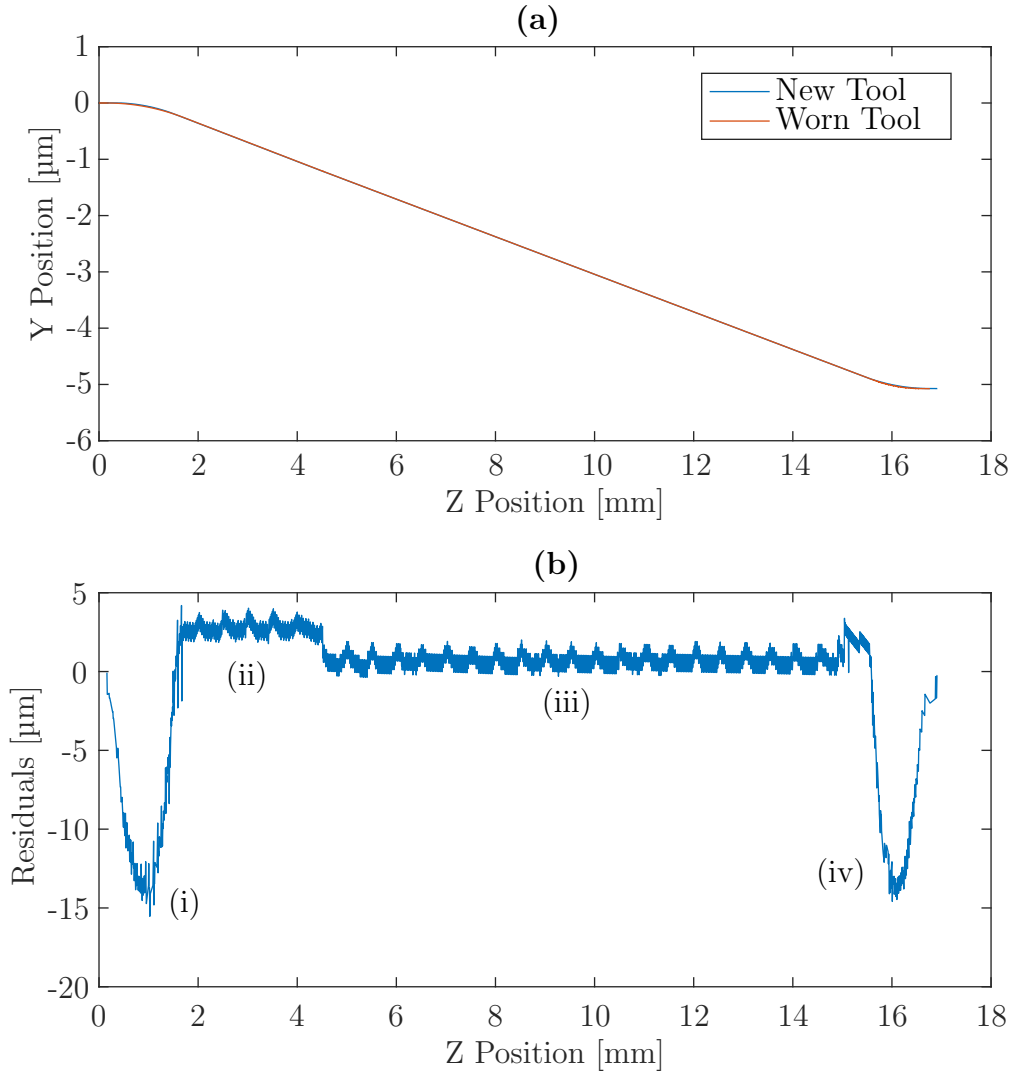

Figure 4.22: (a) Plot showing the workpiece profile based on the recorded encoder counts given a new dressing tool and a worn dressing tool. (b) Figure showing the total error between the profile cut by a new dressing tool and the profile cut by a worn dressing tool.

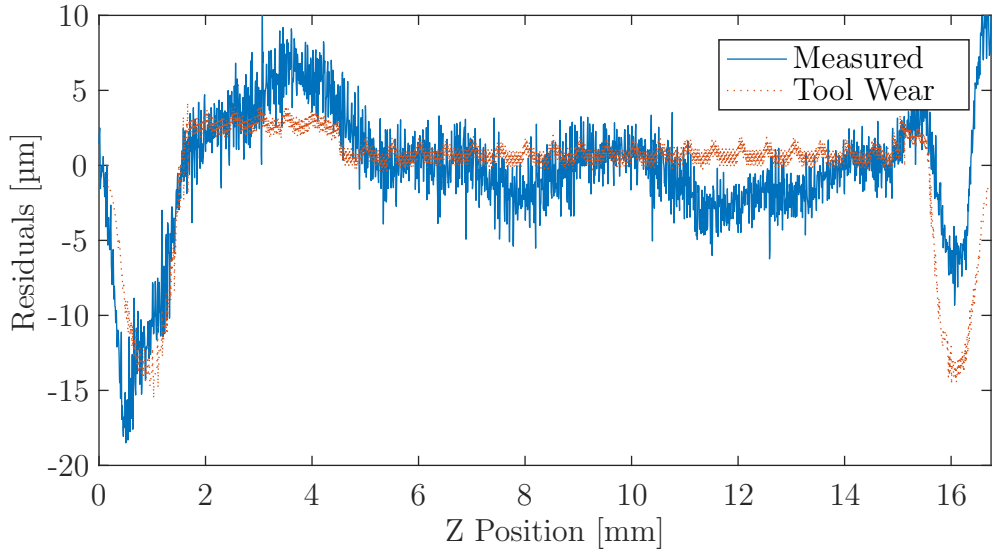

Figure 4.23: Plot comparing measured error and estimated tool wear error.

the measured profile error and the estimated tool wear error does not exceed ±10 µm, therefore it is concluded that the validation of *EDGR*'s positioning performance was successful.

4.5 Conclusions and Recommendations

In this chapter the design and validation of a multi-axis grinding wheel grooving device was presented.

A brief experimental investigation into the forces experienced by a single-point dressing tool during a grooving operation was conducted. From this investigation it was concluded that the average normal and tangential forces experienced by a single-point dressing tool increased with increasing groove depth, but the axial forces remained approximately constant. The measured force signals were highly dynamic in nature. This dynamic quality was proposed to be due to the random impacts of the tool with the randomly-distributed bond material, grains and voids inside of the grinding wheel. To account for the dynamic component of the forces, the root-mean square amplitude of the signals was also calculated. It was determined that the RMS amplitudes of the forces increased with increasing depth of cut in the normal tangential and axial directions. The average forces reached a maximum magnitude

of approximately 70 N and the RMS amplitudes reached a maximum magnitude of approximately 180 N. It was concluded that there is a significant advantage to manufacturing deep grooves using several passes at shallow depths of cut rather than taking a single deep cut.

The design requirements for a multi-axis grooving device were presented, followed by a detailed description of the final design of the prototype grooving device *EDGR*. A description of the control system was presented, along with its positioning performance under no-load conditions.

Finally *EDGR*'s positioning accuracy was validated, first by dressing and truing a flat wheel, then by profiling a grinding wheel. The flat wheel created by *EDGR* was found to have a maximum error from a flat wheel created by the grinding machine of 1.7 µm. The profile created by *EDGR* was found to have a maximum error of exceeding the requirement of ±10 µm from the ideal profile. The wear of the diamond dressing tool was identified as the largest source of error. If the wear error is eliminated from the measured error, then the error falls within the required range. This is considered to be a moderate success, however, further testing should be performed in the future with proper tool geometry compensation to ensure that it is indeed the source of the errors seen in the profile.

In conclusion a multi-axis grooving device prototype was designed and tested and was shown to be capable of meeting the design requirements.

4.5.1 Recommendations for Future Work

EDGR is a prototype grooving device. Therefore, there remain many areas in which its design could be improved.

Currently, *EDGR* meets its wheel synchronization requirements using what might be referred to as an open-loop control method. *EDGR* monitors the grinding machine spindle encoder index pulse and then executes a programmed motion after it receives the index-pulse trigger. The KFLOP has built-in spindle-synchronization capability that was not used for the *EDGR* prototype. Future iterations could attempt to incorporate this capability.

EDGR's waterproofing system consists of a simple polyethylene (PE) plastic shell that fits loosely over the entire structure combined with a high-density polyethylene

(HDPE) wrapping. The waterproofing prevents splashing of lubricant on components and has been successful in preventing chips and dust from getting into *EDGR*'s components; however, it is easily penetrated by mist and condensation. There are extra layers of protection over the more sensitive components, such as the encoders, but the entire waterproofing system could certainly be improved.

The current interface for *EDGR* requires the user to describe a desired profile in MATLAB, manually map out the trajectories, run a preprocessing software on the trajectories that compensates for kinematic errors and automatically writes a G-Code containing the trajectories, save the G-Code to a USB drive and transfer it to the lab computer, and finally run the software on the lab computer. In general the user interface could be improved to reduce the amount of time spent creating and running a trajectory with *EDGR*.

The current safety system for *EDGR* is an emergency shutdown switch that cuts the power to the power supplies and the motors. The location of the emergency shutdown in the electrical system was determined for maximum safety by immediately cutting the power to all high-voltage lines. This system was designed with operator safety and prevention of electrocution in mind. However, when the emergency switch is tripped, there remains significant amount of electrical energy in the motor power supplies, due to their large inductance. Therefore, the motors can remain in motion for a small period of time after tripping the emergency shutdown switch. It would be beneficial to introduce a second emergency switch that tells the KFLOP to cut power to the motors directly, regardless of the state of the motor power supplies. The lab computer software interface for the KFLOP has this capability, but a firmware/hardware solution would be more reliable.

EDGR's control system was designed through manual tuning. A brief analysis of *EDGR*'s dynamics found significant non-linear behaviour. It is possible that the control system performance could be improved through the design of a non-linear controller implemented directly in C code, instead of using the continuous-time linear control capability that comes packaged with the KFLOP.

The accuracy validation in this chapter showed that tool wear can cause significant errors in the grooves and profiles generated by *EDGR*. The tool is simply held

vertical in *EDGR*'s tool holder, which is not the manufacturer-recommended orientation. *EDGR*'s tool holder could be redesigned to hold the tool at the manufacturer-recommended angle of 15° from vertical. An adjustable tool holder would be a useful improvement. This would allow the tool to be rotated over the course of use and should create a more even tool wear without sharp corners.

The stage and rail selected for the vertical actuator is significantly longer than necessary. It was chosen because it met the design load requirements and positioning accuracy requirements. However, a much shorter stage could be used. Using a shorter stage could allow for a more compact design, which would leave more room in the grinding machine for other equipment.

The motor power cables are not shielded. The cables are approximately 10 m long and carry 60 V and 45 V pulse-width modulated (PWM) signals. These cables presents a significant noise issue in the lab, such that the motor power supplies must be shut down any time the operator wants to take accurate spindle power recordings. Some shielding for the high-voltage supply cables should cause a significant decrease in the noise.

Chapter 5

Kinematics of a Grinding Wheel Grooving Device

At first glance *EDGR*'s kinematics appear straightforward. However, complexity is added due to two factors: 1) *EDGR*'s workspace is a plane in Cartesian coordinates, but the "workpiece" (the grinding wheel) is cylindrical and therefore nonlinear; 2) *EDGR* is a robot operating inside of another robot (the grinding machine). These additional complexities presented a significant challenge: identifying the position of *EDGR*'s end effector (dressing tool) relative to the center of the grinding wheel in cylindrical coordinates down to a precision of only several micrometers. To overcome this challenge, a method to precisely determine *EDGR*'s workspace and a novel kinematic error compensation method were developed.

In this section the kinematics of the grinding wheel grooving device, *EDGR*, are described in detail. A novel measurement technique for determining *EDGR*'s workspace is also presented. Finally, a kinematic error compensation algorithm is described and its performance is demonstrated in practice.

5.1 Kinematics of Helical Grooves

During a grooving operation, the grinding wheel rotates at constant speed while *EDGR* moves the single point dressing tool along the wheel profile. In order to perform this operation the feed rates (velocities) of the dressing tool in the horizontal v_z and vertical v_y directions must be solved for a desired groove geometry.

The dressing tool moves across the wheel width at a speed v_z while the grinding wheel rotates at constant angular velocity ω_s. These conditions produce a groove lead L_g that can be calculated using

$$L_g = \frac{2\pi v_z}{\omega_s}\,, \tag{5.1}$$

where the units of v_z are $\mathrm{mm\,s^{-1}}$, and the units of ω_s are $\mathrm{rad\,s^{-1}}$, which gives L_g in units of $\mathrm{mm\,rev^{-1}}$.

Substituting (5.1) into (2.1) allows the groove helix angle to be calculated using

$$\alpha_g = \arctan\left(\frac{\omega_s r_s}{v_z}\right) = \arctan\left(\frac{v_s}{v_z}\right), \tag{5.2}$$

where v_s is the tangential surface speed of the grinding wheel and r_s is the radius of the grinding wheel.

Using trigonometric identities, it can be determined that

$$\cos\alpha_g = \frac{v_z}{\sqrt{(\omega_s r_s)^2 + {v_z}^2}}. \tag{5.3}$$

Inserting (5.3) into (2.12) yields an expression for the intermittent ratio η_g in terms of the wheel velocity and tool feed rate:

$$\eta_g = 1 - \frac{N_g b_g \sqrt{(\omega_s r_s)^2 + {v_z}^2}}{2\pi r_s v_z}, \tag{5.4}$$

where N_g is the number of groove starts and b_g is the width of the grooves perpendicular to the groove direction.

Rearranging for v_z yields

$$v_z = \omega_s \left(\left(\frac{2\pi(1-\eta_g)}{N_g b_g}\right)^2 - \left(\frac{1}{r_s}\right)^2\right)^{-1/2}. \tag{5.5}$$

For a flat grinding wheel with a groove of constant depth, all of the parameters on the right hand side of (5.5) are constants. For a profile grinding wheel, however, the wheel radius r_s is a function of z. Therefore the feed rate is a function of z in order to produce a helical groove on a profile grinding wheel. However, for most single-point grooves the number of grooves is equal to 1 and the groove width b_g is small (on the order of several millimeters. The wheel diameter tends to be significantly larger than the groove width: generally 300 mm or larger. Furthermore, the intermittent ratio tends to have values between 0.5 and 0.8. Given these common groove geometry values, the $1/r_s^2$ term becomes negligibly small (at least three orders of magnitude smaller) compared to the other term. By eliminating the $1/r_s^2$ term, the equation can be simplified to

$$v_z \approx \frac{N_g \omega_s b_g}{2\pi(1-\eta_g)}. \tag{5.6}$$

Assuming that the control algorithm compensates for the profile slope to ensure a constant groove width, all terms on the right-hand-side of the equation are constant.

Therefore a constant feed rate can be used to create helical grooves on a profile grinding wheel.

For the experiments performed in this work the feed rate of the grooving device v_z was held constant. However, the tool-radius compensation algorithm that was used compensated to ensure constant groove depth, not constant groove width. Therefore the grooves created were helical grooves with constant depth, but the groove width, and therefore groove factor, varied with varying wheel profile slope. Using the known tool geometry, the groove factor could be calculated for any part of the wheel using (2.14).

Once the horizontal feed rate is known, the vertical feed rate v_y of the dressing tool for a given wheel profile can be determined using

$$v_y(z) = v_z \frac{\delta\rho}{\delta z}\,, \tag{5.7}$$

where $\delta\rho/\delta z$ is the slope of the grinding wheel profile.

In conclusion, given any wheel profile and helical groove geometry, the necessary feed rates of the dressing tool in the horizontal and vertical directions can be determined.

5.2 Forward Kinematics of a Grinding Wheel Grooving Device

The forward kinematics is the solution to the problem of determining the position of the the robot end effector (dressing tool) given a set of joint values (linear stage positions).

Figure 5.1 shows *EDGR* inside the grinding machine and describes the various coordinate systems and important vectors that will be used in this section. The grinding machine Cartesian coordinate system X_G, Y_G, Z_G is shown in the bottom-left corner. The local cylindrical coordinate system of the grinding wheel ρ, φ, z is shown at the grinding wheel center.

Figure 5.2 shows *EDGR*'s basis vectors $\hat{v}$ and $\hat{w}$, defined as the unit vectors parallel to the directions of the stage lead screws.

The position of the diamond dressing tool can be described in both Cartesian and cylindrical coordinates. The origin of the local Cartesian coordinate system is defined as being located at the bottom dead centre, front wheel face of the grinding wheel.

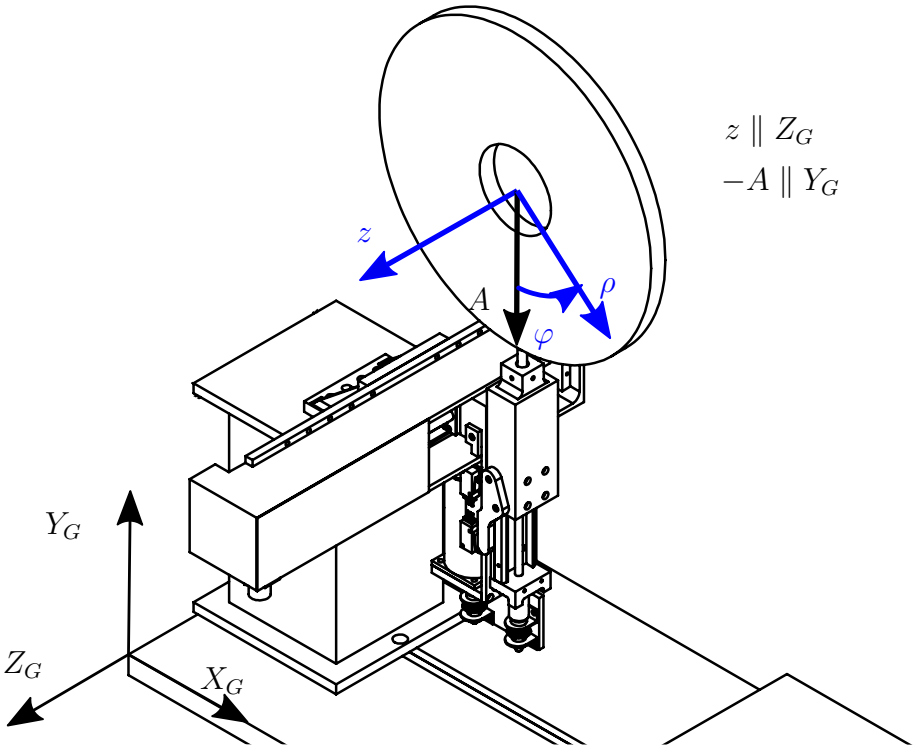

Figure 5.1: Diagram showing the coordinate systems inside the grinding machine.

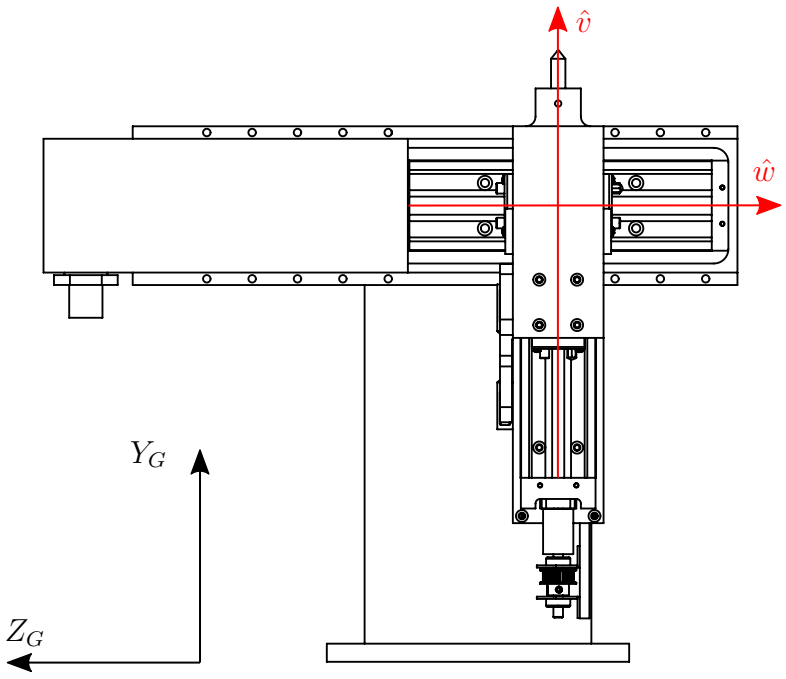

Figure 5.2: Diagram showing the directions of *EDGR*'s basis vectors $\hat{v}$ and $\hat{w}$.

The origin of the local cylindrical coordinate system is defined as being located at the center of the wheel on the front wheel face. A diagram of the local coordinate systems is shown in Figure 5.3.

Let the position of the tip of the tool in 3-dimensional Cartesian space be defined by the vector $\vec{r}_t$. Equations (5.8) and (5.9) describe the methods for converting between the two coordinate systems:

$$\vec{r}_t = \begin{bmatrix} x_t \\ y_t \\ z_t \end{bmatrix} = \begin{bmatrix} \rho_t \sin \varphi_t \\ r_s - \rho_t \cos \varphi_t \\ z_t \end{bmatrix} , \tag{5.8}$$

$$\begin{bmatrix} \rho_t \\ \varphi_t \\ z_t \end{bmatrix} = \begin{bmatrix} \sqrt{x_t^2 + (r_s - y_t)^2} \\ \arctan\left(\frac{x_t}{r_s - y_t}\right) \\ z_t \end{bmatrix} , \tag{5.9}$$

where r_s is the radial distance from the center of the grinding wheel to the origin of the Cartesian coordinate system; x_t, y_t and z_t define the position of the tool in Cartesian coordinates in the longitudinal, vertical and transverse directions, respectively; and ρ_t, φ_t and z_t define the position of the tool in cylindrical coordinates in the radial, circumferential and axial directions, respectively.

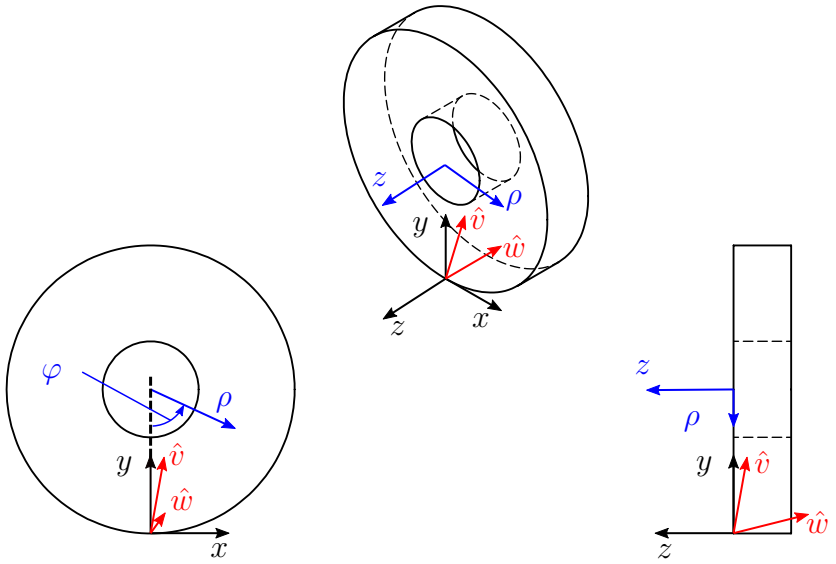

Figure 5.3: Diagram showing the local Cartesian and cylindrical coordinate systems at the grinding wheel.

For any given joint values (positions of the stages along the lead screws) of *EDGR*'s linear stages, the position of the tip of the tool can be calculated using

$$\vec{r_t} = \begin{bmatrix} \hat{v} & \hat{w} \end{bmatrix} \begin{bmatrix} q_1 \\ q_2 \end{bmatrix}, \tag{5.10}$$

where q_1 is the joint value of the vertical stage, q_2 is the joint value of the horizontal stage, $\hat{v}$ is the unit vector denoting the direction of the axis of the vertical stage in 3D space and $\hat{w}$ is the unit vector denoting the direction of the axis of the horizontal stage in 3D space.

The joint values have the following ranges:

$$0 \text{ mm} < q_1 < 40 \text{ mm},$$

$$-104 \text{ mm} < q_2 < 0 \text{ mm}.$$

Let $\mathbf{B} = \begin{bmatrix} \hat{v} & \hat{w} \end{bmatrix}$ be the basis defining the planar workspace of the groover, and $\vec{q} = \begin{bmatrix} q_1 & q_2 \end{bmatrix}^\mathsf{T}$ be the vector containing the joint values. Then *EDGR*'s forward kinematics can be defined as

$$\vec{r_t} = \mathbf{B}\vec{q}. \tag{5.11}$$

EDGR's workspace can be pictured as a plane in 3D Cartesian space passing through the origin with its orientation defined by the vectors $\hat{v}$ and $\hat{w}$. Figure 5.4 illustrates *EDGR*'s workspace with greatly exaggerated misalignment between the stage axes and the grinding machine axes.

In conclusion, given any joint values $\vec{q}$ and known basis vectors, the resulting position $\vec{r_t}$ of the grinding wheel dressing tool in cylindrical or Cartesian coordinates can be determined.

5.3 Inverse Kinematics of a Grinding Wheel Grooving Device

Inverse kinematics is the solution to the problem of determining the joint values required in order to reach a desired end effector (dressing tool) position.

EDGR's workspace is a plane within the grinding machine workspace. The workspace of the grinding machine is a rectangular volume. Therefore, *EDGR* is not capable of reaching every location within the grinding machine workspace. Due to

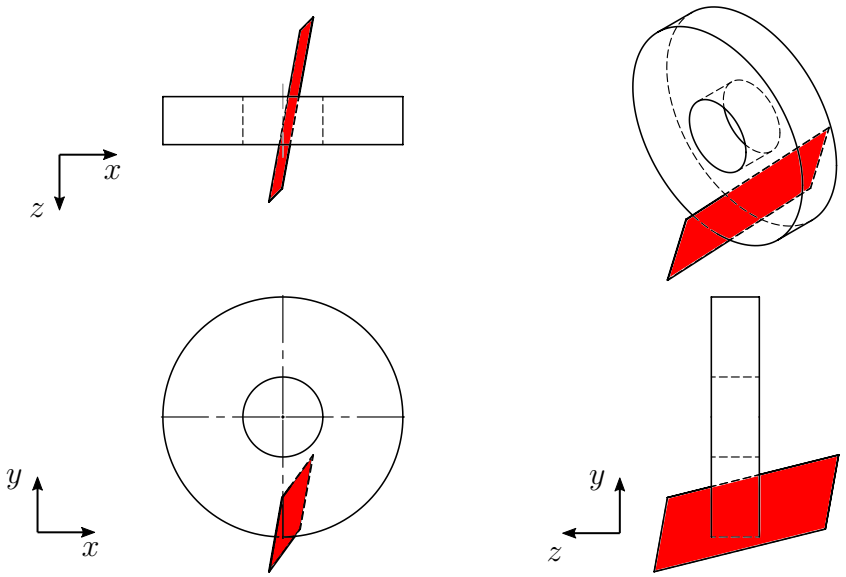

Figure 5.4: Diagram showing the groover workspace as a plane with a greatly exaggerated misalignment from the grinding machine axes.

EDGR's kinematics being linear in Cartesian coordinates, the solution to the inverse kinematics for a desired Cartesian tool position $\vec{r}_d$ can be calculated using the Moore-Penrose pseudoinverse:

$$\vec{q} = (\mathbf{B}^\mathsf{T}\mathbf{B})^{-1}\mathbf{B}^\mathsf{T}\vec{r}_d\,. \tag{5.12}$$

For desired positions that lie within *EDGR*'s workspace, (5.12) will yield the joint values that will achieve the desired tool position exactly. However, if a desired position does not lie within *EDGR*'s workspace, (5.12) minimizes the sum of squared errors in the Cartesian space, that is, it yields the joint values $\vec{q}$ that minimize the absolute distance between the desired tool position and the resulting tool position:

$$\underset{\vec{q}}{\operatorname{argmin}} \left(\varepsilon_{xyz}^\mathsf{T}\varepsilon_{xyz}\right) = (\mathbf{B}^\mathsf{T}\mathbf{B})^{-1}\mathbf{B}^\mathsf{T}\vec{r}_d\,, \tag{5.13}$$

where ε_{xyz} is the error between the resulting tool position $\vec{r}_t$ and the desired tool position $\vec{r}_d$ in Cartesian coordinates:

$$\varepsilon_{xyz} = \begin{bmatrix}\varepsilon_x\\ \varepsilon_y\\ \varepsilon_z\end{bmatrix} = \vec{r}_t - \vec{r}_d = \begin{bmatrix}x_t - x_d\\ y_t - y_d\\ z_t - z_d\end{bmatrix}\,. \tag{5.14}$$

However, what is critical for a wheel grooving or profiling operation is not the absolute distance error in Cartesian space, but the errors in the cylindrical geometry of the grinding wheel produced by a given trajectory. Let the error in cylindrical coordinates be defined as

$$\varepsilon_{\rho\varphi z} = \begin{bmatrix} \varepsilon_\rho \\ \varepsilon_\varphi \\ \varepsilon_z \end{bmatrix} = \begin{bmatrix} \rho_t - \rho_d \\ \varphi_t - \varphi_d \\ z_t - z_d \end{bmatrix}, \tag{5.15}$$

where ε_ρ, ε_φ, and ε_z are the differences in the ρ, φ and z coordinates between the two positions.

The relationship between the joint values $\vec{q}$ and a desired position in cylindrical coordinates $\vec{r}_t$ is not linear; therefore, the Moore-Penrose pseudoinverse does not minimize the error in cylindrical coordinates. Furthermore, minimizing the sum of the squared errors in cylindrical coordinates is not necessarily desired. For a profiling operation, the angular position of the tool is irrelevant; therefore, ε_φ can be any value but the ε_ρ and ε_z errors should be minimized.

For a grooving operation, the radial error ε_ρ is responsible for the error in the groove width and depth and should be minimized. The axial error ε_z and angular error ε_φ both affect the error in the groove trajectory in the φ-z space. However, *EDGR*'s workspace is approximately aligned with the radial and axial directions of the wheel and therefore the angular errors, regardless of the joint values $\vec{q}$, are minimal. Assuming a wheel diameter of 300 mm, a desired angular position of $\varphi = 0°$ and given the measured values for $\hat{v}$ and $\hat{w}$ given later in the chapter, the maximum angular error within the entire joint space is $\varepsilon_{\varphi,\max} = 0.97°$.

The angular error would present itself as an error in the lead (or helix angle) of a helical groove. In this case, the maximum error occurs on a wheel with a radius that starts at 300 mm at $z = 0$ mm and tapers to 260 mm at $z = 104$ mm. If a groove with a constant lead of 2.0 mm rev^{-1} was desired, then after 104 mm the groove should have wound around the wheel 52 times or $52 \times 360° = 18720°$. However, due to the angular error, it would only have wound around the wheel $18720° - 0.97° = 18719.03°$. The actual lead would therefore be 1.99990 mm rev^{-1} which is a completely negligible difference from the desired lead. Even if the desired groove lead was the maximum lead that *EDGR* is capable of, 100 mm rev^{-1}, the resulting groove lead would be

99.73 mm rev^{-1} *at worst*. For a combination of the worst-case wheel geometry and the worst-case groove lead, the error is less than 0.5%. Therefore the angular error can be ignored and effort should be made instead to minimize the radial and axial error.

In conclusion, the solution to *EDGR*'s inverse kinematics is a linear-least-squares fit in Cartesian coordinates. However, this solution does not properly minimize the errors that would be created on the grinding wheel in cylindrical coordinates.

5.4 Kinematic Error Compensation

Ideally the direction vectors of the linear stages, $\hat{v}$ and $\hat{w}$, would be parallel to the Y and Z axes of the grinding machine. However, significant misalignment is introduced when *EDGR* is assembled in the grinding machine. The misalignment creates what is sometimes referred to as "kinematic error": the error introduced to the tool path by the kinematics of the machine. There are two ways of dealing with the kinematic errors. Firstly, greater care could be taken during assembly to ensure that the axes are properly aligned. This method would require many hours of work with metal shim stock and precise measurements every time *EDGR* is reinstalled in the grinding machine. The second method is "kinematic error compensation". As long as the vectors $\hat{v}$ and $\hat{w}$ are known to within a reasonable accuracy, the kinematic errors can be eliminated by accounting for the kinematics in the control system. This method requires significantly less time during installation of *EDGR*.

The kinematic error compensation for *EDGR* is slightly more complicated than solving the inverse kinematics because it is not possible to simultaneously eliminate ε_ρ, ε_φ, and ε_z. From the previous analysis it was determined that the angular error ε_φ in the groove geometry due to the alignment between *EDGR*'s axes and the grinding machine axes can be safely ignored. Building from this conclusion, a method was developed to eliminate the theoretical errors in the ρ and z position of the grooving device.

The desired position defined by ρ_d and z_d forms a circle in Cartesian space on the x–y plane with its center located at $(x = 0, y = r_s)$, at a z position of z_d. In order to reach the desired ρ_d and z_d position, the point of intersection $\vec{r}_d$ in Cartesian coordinates between this circle and *EDGR*'s workspace must be calculated. This

concept is illustrated in Figure 5.5.

The intersection point can be calculated as follows. If a point lies within *EDGR*'s workspace then the vector to that point $\vec{r}_d$ is orthogonal to the normal vector of the basis formed by $\hat{v}$ and $\hat{w}$. That is, if the point defined by the vector $\vec{r}_d$ lies within the planar workspace, then:

$$\vec{r}_d \cdot \hat{v} \times \hat{w} = 0 \tag{5.16}$$

Let $\vec{n} = \hat{v} \times \hat{w}$.

$$\vec{n} = \begin{bmatrix} n_1 \\ n_2 \\ n_3 \end{bmatrix} = \begin{bmatrix} v_2 w_3 - v_3 w_2 \\ v_1 w_3 - v_3 w_1 \\ v_1 w_2 - v_2 w_1 \end{bmatrix} \tag{5.17}$$

Inserting the conversion between Cartesian and cylindrical coordinates and (5.17) into (5.16) yields:

$$\begin{bmatrix} \rho_d \sin \varphi_e \\ r_s - \rho_d \cos \varphi_e \\ z_d \end{bmatrix} \cdot \begin{bmatrix} n_1 \\ n_2 \\ n_3 \end{bmatrix} = 0$$

where φ_e is the angular location of the intersection between the workspace and the desired ρ_d circle. Rearranging yields:

$$n_1 \rho_d \sin \varphi_e + n_2 r_s - n_2 \rho_d \cos \varphi_e + n_3 z_d = 0$$

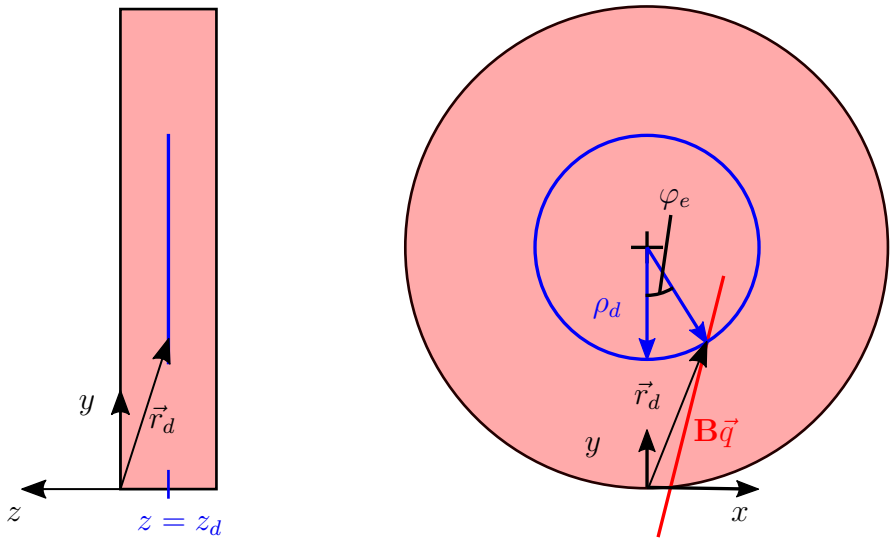

Figure 5.5: Solving for the intersection point $\vec{r}_d$ between the desired ρ_d circle at a position of z_d and the groover workspace $\mathbf{B}\vec{q}$.

$$n_1 \sin\varphi_e - n_2 \cos\varphi_e + \frac{n_2 r_s + n_3 z_d}{\rho_d} = 0$$

Using the trigonometric identity $a\sin x + b\cos x = \sqrt{a^2+b^2}\sin\left(x + \arctan\left(b/a\right)\right)$ and solving for φ_e:

$$\sqrt{n_1^2+n_2^2}\sin\left(\varphi_e + \arctan\left(\frac{-n_2}{n_1}\right)\right) = \frac{-\left(n_2 r_s + n_3 z_d\right)}{\rho_d}$$

$$\varphi_e = \arcsin\left(\frac{-\left(n_2 r_s + n_3 z_d\right)}{\rho_d\sqrt{n_1^2+n_2^2}}\right) - \arctan\left(\frac{-n_2}{n_1}\right) \tag{5.18}$$

For a given ρ_d and z_d the value of φ_e can be determined using equation 5.18. Once the cylindrical coordinates of the intersection point are known, they can be used to find the necessary joint values to reach the desired location:

$$\vec{q} = \left(\mathbf{B}^\mathsf{T}\mathbf{B}\right)^{-1}\mathbf{B}^\mathsf{T}\begin{bmatrix}\rho_d\sin\varphi_e \\ r_s - \rho_d\cos\varphi_e \\ z_d\end{bmatrix} \tag{5.19}$$

Equation 5.18 can be simplified using the small angle identities $\sin\theta \approx \theta$ and $\cos\theta \approx 1 - 0.5\theta^2$.

$$\varphi_e = -\frac{n_1}{n_2} - \sqrt{\left(\frac{n_1}{n_2}\right)^2 - \frac{2z_t}{\rho_t}\left(\frac{n_3}{n_2}\right) + \frac{2\left(r_s-\rho_t\right)}{\rho_t}} \tag{5.20}$$

Equation 5.20 takes 66% as much time to solve as equation 5.18 when implemented in MATLAB and produces results that are negligibly different.

In conclusion, a method of eliminating the radial and axial errors caused by misalignment between the grinding machine and *EDGR* has been developed.

5.4.1 Identifying the Basis Vectors

The previous sections described the solutions to the forward and inverse kinematics, and a kinematic error compensation method for when the direction vectors of the linear stages $\hat{v}$ and $\hat{w}$ are known. However, determining those vectors at the accuracy needed is not a trivial problem. In this section the method used to determine the direction vectors of the linear stages is described.

The main challenge that must be overcome in measuring the alignment of the linear stages is the lack of a 3-dimensional measurement device that could be used

inside of the grinding machine. Alignment measurements in 3-dimensional space had to be made with a 1-dimensional dial gauge attached to the grinding machine, pictured in Figure 5.6. The dial gauge was used as a 1-dimensional touch probe to determine when the grinding machine was a consistent distance from one of *EDGR*'s faces. The grinding machine spindle position could then be read from the grinding machine controller screen to determine the location of the point being touched in relative 3-dimensional coordinates to within an accuracy of ±1.25 µm.

The problem arises when measurements need to be taken on several perpendicular surfaces. In Figure 5.6 the dial gauge is shown in a configuration for measuring the top surface of *EDGR*'s tool holder. If measurements needed to be made of a different surface, such as the front-facing surface, the entire setup had to be re-configured. Reconfiguring the measurement setup required manually turning and repositioning the setup, thereby losing absolute position information. Therefore, any points measured on a front-facing surface cannot be related in absolute coordinates to points measured on a top-facing or right-facing surface. The lack of an ability to take absolute measurements from multiple angles is a problem because the most accurate way to measure the alignment vector of the stage is to take multiple orthogonal

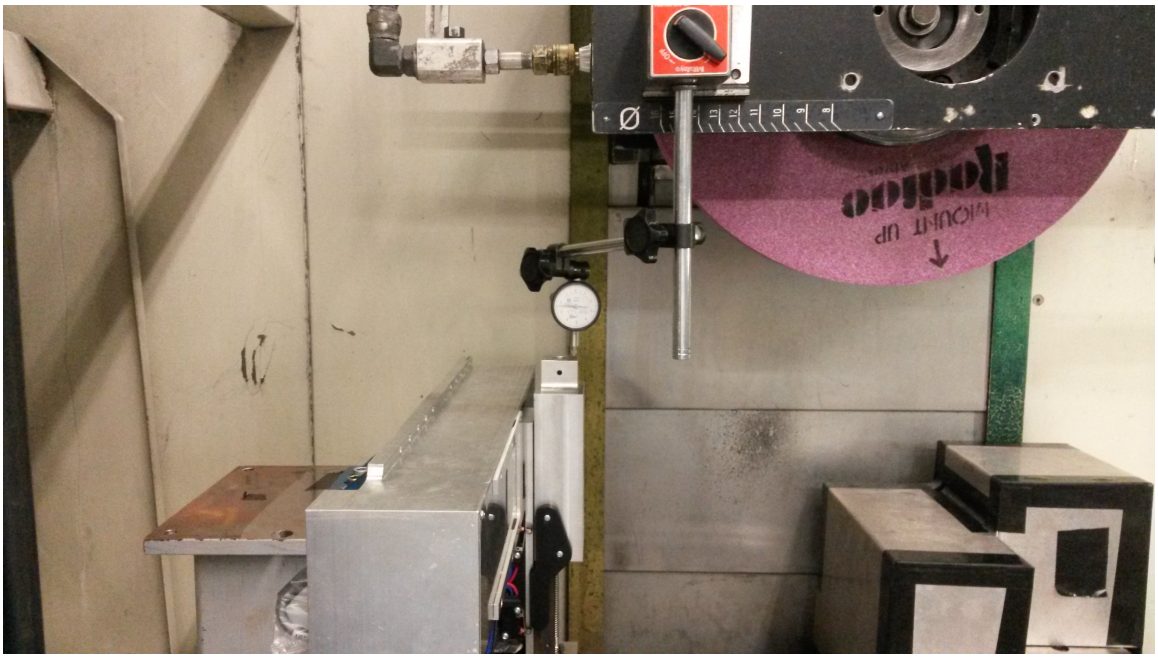

Figure 5.6: Top-facing surface measurement configuration of the alignment measurement setup.

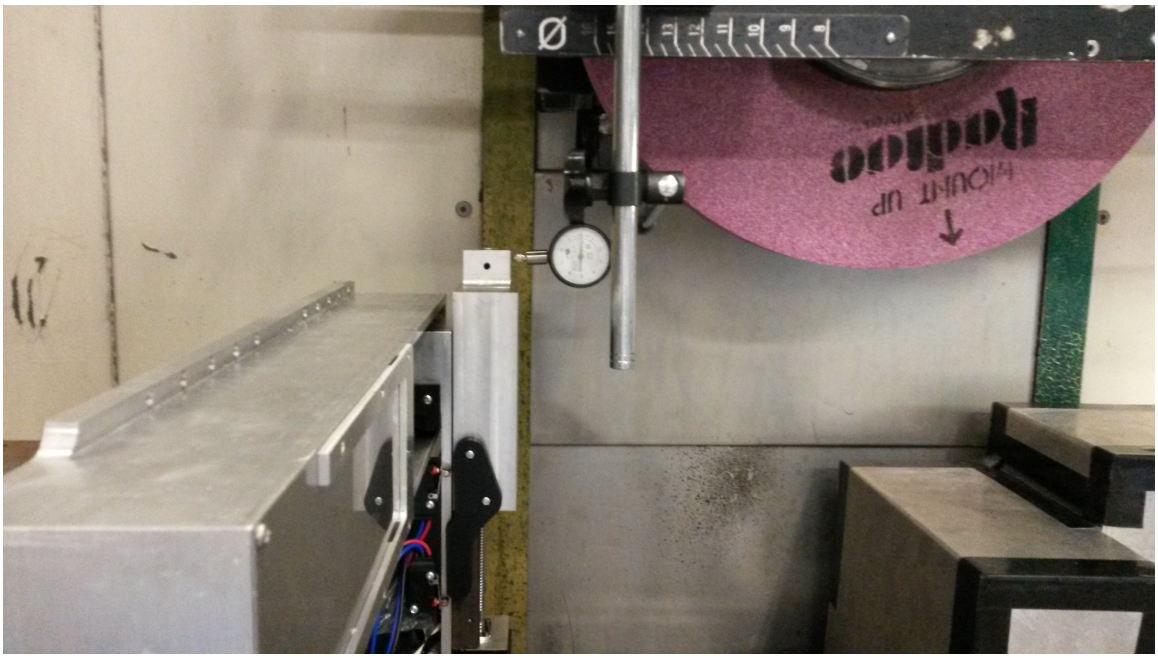

Figure 5.7: Front-facing surface measurement configuration of the alignment measurement setup.

measurements.

The following method was developed to overcome the challenges posed by the measurement setup. The method assumes that there is no rotation of the faces of the tool holder due to bow or curvature in the stages.

1. The vertical stage was locked in position.
2. A series of top-facing surface measurements were taken.
   (a) The measurement setup was configured to measure top-facing surfaces.
   (b) The horizontal stage was moved to a joint value of $q_2 = 0$ mm.
   (c) Four points $P_{H1,T1\text{–}4}$ were measured on the top-facing surface of the tool holder.
   (d) The horizontal stage was moved to a joint value of $q_2 = -100$ mm.
   (e) Four new points $P_{H2,T1\text{–}4}$ were measured on the top-facing surface of the tool holder.
3. A series of front-facing surface measurements were taken.

(a) The measurement setup was configured to measure front-facing surfaces.

(b) Four points $P_{H2,F1\text{–}4}$ were measured on the front-facing surface of the tool holder.

(c) The horizontal stage was moved to a joint value of $q_2 = 0$ mm.

(d) Four new points $P_{H1,F1\text{–}4}$ were measured on the front-facing surface of the tool holder.

4. A series of right-facing surface measurements were taken.

(a) The measurement setup was configured to measure right-facing surfaces.

(b) Four points $P_{H1,R1\text{–}4}$ were measured on the right-facing surface of the tool holder.

(c) The horizontal stage was moved to a joint value of $q_2 = 100$ mm.

(d) Four new points $P_{H2,R1\text{–}4}$ were measured on the right-facing surface of the tool holder.

5. All previous steps were repeated for the vertical axis moving from position V_1 to position V_2 with the horizontal axis locked in position.

The measurement method is illustrated in Figure 5.8.

Once these points were measured, the orientation of the surfaces were determined by calculating a plane of best fit for each set of eight points. The planes of best fit were calculated using the singular value decomposition of each set of eight points. This method is described for the top-facing plane by the following steps:

1. The centroid $\bar{p}_{H1T}$ of the points at position H_1 was calculated and then subtracted from the points so that the centroid of the data is now the origin (0,0,0).

2. The centroid $\bar{p}_{H2T}$ of the points at position H_2 was calculated and then subtracted from the points so that the centroid of the data is now the origin (0,0,0).

3. A 3×8 matrix $\mathbf{M}_T$ was created where the $[x, y, z]$ coordinates of each of the eight points form the columns.

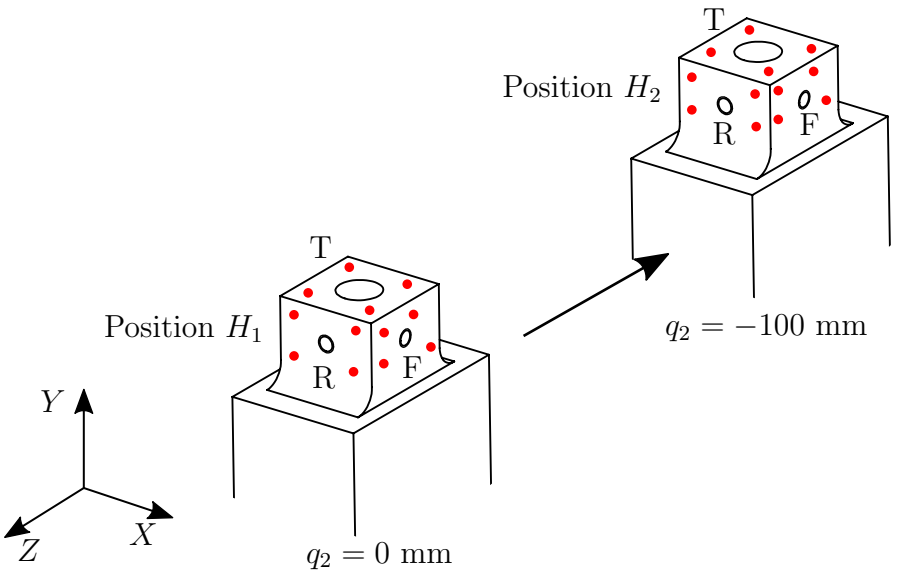

Figure 5.8: Several points (red dots) were measured on the top (T), front (F) and right (R) planes of the dressing tool holder in two different positions.

4. The singular value decomposition of $\mathbf{M}_T$ was calculated using the `svd` command in MATLAB:

$$\mathbf{M}_T = \mathbf{U}_T \mathbf{\Sigma}_T \mathbf{V}_T^* \tag{5.21}$$

The columns of $\mathbf{U}_T$ are called the "left-singular vectors" of $\mathbf{M}_T$. The diagonal values of $\mathbf{\Sigma}_T$ are called the "singular values" of $\mathbf{M}_T$. The column of $\mathbf{U}_T$ that corresponds to the minimum singular value in $\mathbf{\Sigma}_T$ is the normal vector $\vec{n}_T$ of the best-fitting plane to the dataset. [38]

5. The unit normal vector to the plane of best fit $\hat{n}_T$ was calculated:

$$\hat{n}_T = \frac{\vec{n}_T}{\|\vec{n}_T\|} = \begin{bmatrix} a_T \\ b_T \\ c_T \end{bmatrix} \tag{5.22}$$

Where a_T, b_T and c_T are the coefficients of the equation of the plane:

$$a_T x + b_T y + c_T z = d$$

6. The unit normal vector was then used to calculate the shortest distance d_{H1T} between the plane of best fit containing the H_1 centroid $\bar{p}_{H1T}$ and the origin:

$$d_{H1T} = \hat{n}_T \cdot \bar{p}_{H1T} \tag{5.23}$$

which fully defines the equation of the top surface plane for the H_1 position:

$$a_T x + b_T y + c_T z = d_{H1T} \tag{5.24}$$

7. Similarly, the unit normal vector was used to calculate the shortest distance d_{H2T} between the plane of best fit containing the H_2 centroid $\bar{p}_{H2T}$ and the origin.

8. Steps 1–7 were repeated for the front- and right-facing surfaces to get $\hat{n}_F$, $\hat{n}_R$, d_{H1F}, d_{H2F}, d_{H1R}, and d_{H2R}.

9. Steps 1–8 were repeated for the vertical positions V_1 and V_2.

Once the equations of all six planes were determined, the intersection points between the three planes at each position, H_1, H_2, V_1 and V_2 were calculated.

$$p_{H1,\text{int}} = \left(\begin{bmatrix} \hat{n}_T & \hat{n}_F & \hat{n}_R \end{bmatrix}^\mathsf{T} \right)^{-1} \begin{bmatrix} d_{H1T} \\ d_{H1F} \\ d_{H1R} \end{bmatrix} \tag{5.25}$$

$$p_{H2,\text{int}} = \left(\begin{bmatrix} \hat{n}_T & \hat{n}_F & \hat{n}_R \end{bmatrix}^\mathsf{T} \right)^{-1} \begin{bmatrix} d_{H2T} \\ d_{H2F} \\ d_{H2R} \end{bmatrix} \tag{5.26}$$

$$p_{V1,\text{int}} = \left(\begin{bmatrix} \hat{n}_T & \hat{n}_F & \hat{n}_R \end{bmatrix}^\mathsf{T} \right)^{-1} \begin{bmatrix} d_{V1T} \\ d_{V1F} \\ d_{V1R} \end{bmatrix} \tag{5.27}$$

$$p_{V2,\text{int}} = \left(\begin{bmatrix} \hat{n}_T & \hat{n}_F & \hat{n}_R \end{bmatrix}^\mathsf{T} \right)^{-1} \begin{bmatrix} d_{V2T} \\ d_{V2F} \\ d_{V2R} \end{bmatrix} \tag{5.28}$$

Finally, the unit alignment vector of the horizontal stage $\hat{w}$ is the unit vector pointing from $p_{H1,\text{int}}$ to $p_{H2,\text{int}}$.

$$\hat{w} = \frac{p_{H2,\text{int}} - p_{H1,\text{int}}}{\| p_{H2,\text{int}} - p_{H1,\text{int}} \|} \tag{5.29}$$

Similarly the unit alignment vector of the vertical stage $\hat{v}$ was calculated.

$$\hat{v} = \frac{p_{V2,\text{int}} - p_{V1,\text{int}}}{\| p_{V2,\text{int}} - p_{V1,\text{int}} \|} \tag{5.30}$$

In conclusion, a novel method was developed to measure the alignment between *EDGR*'s linear stages and the global axes of the grinding machine.

5.4.2 Results of the Kinematic Error Compensation

Using the method described above, the unit direction vectors of the vertical and horizontal axes were determined. The values of these vectors are reported below:

$$\hat{v} = \begin{bmatrix} -0.0045 \\ 1.0000 \\ -0.0012 \end{bmatrix}$$

$$\hat{w} = \begin{bmatrix} -0.0205 \\ 0.0018 \\ 0.9998 \end{bmatrix}$$

The performance of the kinematic error compensation algorithm was validated by truing a flat grinding wheel. First the flat grinding wheel was trued using *EDGR* without kinematic error compensation, with the joint values determined as if *EDGR*'s stages were perfectly aligned with the y- and z-axes of the grinding machine. The grinding wheel was then used to grind a single pass on a 1018 steel workpiece. A photograph of the workpiece is shown in Figure 5.9. The workpiece had previously been ground flat by a grinding wheel trued on the grinding machine to provide a reference surface to which the new wheel cut could be compared. The grinding wheel was then trued using *EDGR* with kinematic error compensation and the wheel was used to make a second cut on the same workpiece. The workpiece was then removed from the grinding machine and scanned using a Nanovea CHR150 profilometer. A scan of the uncompensated cut is shown in Figure 5.10. A scan of the compensated cut is shown in Figure 5.11. These results were already partly reported in Chapter 4 as a part of the design validation.

In Figure 5.10, there is clearly a slope to the bottom of the grinding wheel in the y-z plane. The slope was measured relative to the top reference surface and was found to be 1.48 µm mm^{-1}. Therefore, over a wheel width of 26.7 mm, the wheel profile would have a maximum radial error of $\varepsilon_\rho = \pm 19.8$ µm from a perfect flat grinding wheel. This is larger than the accuracy requirement given in Chapter 4 of

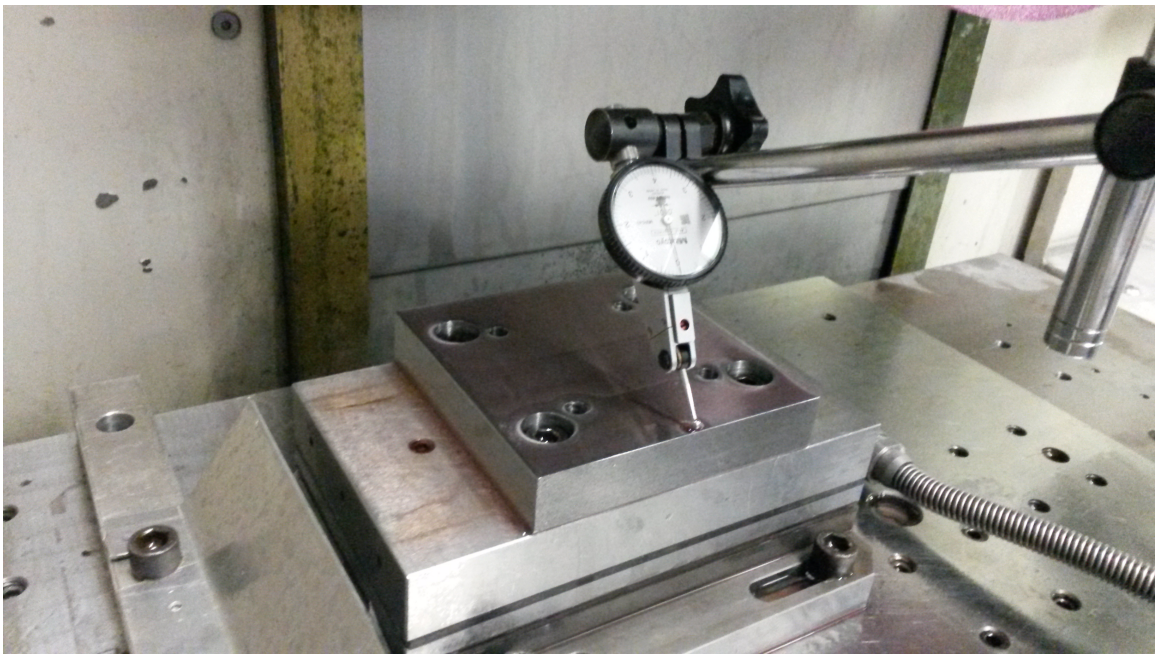

Figure 5.9: Steel specimen for kinematic error compensation validation inside the grinding machine, mounted to the force dynamometer.

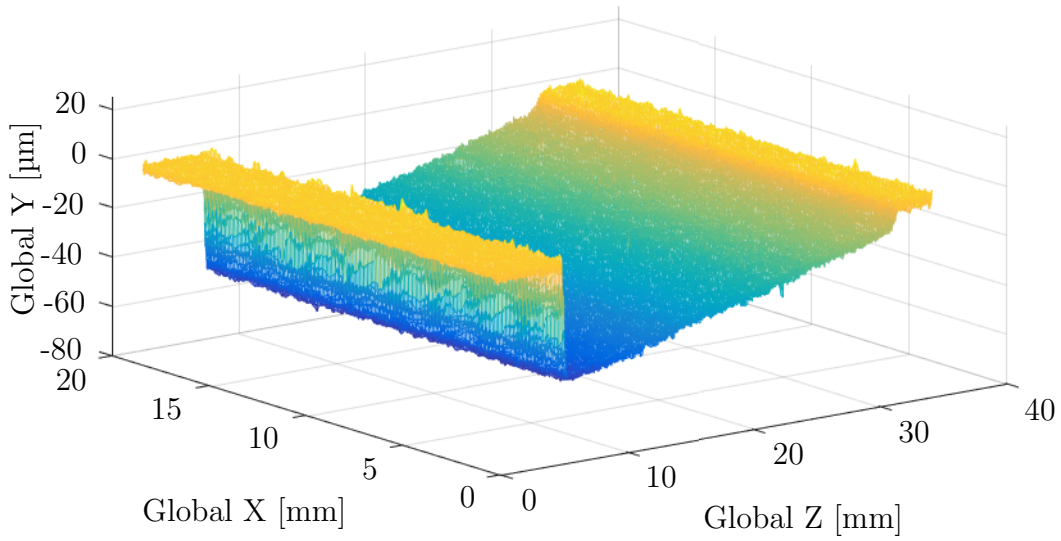

Figure 5.10: Uncompensated workpiece surface scan.

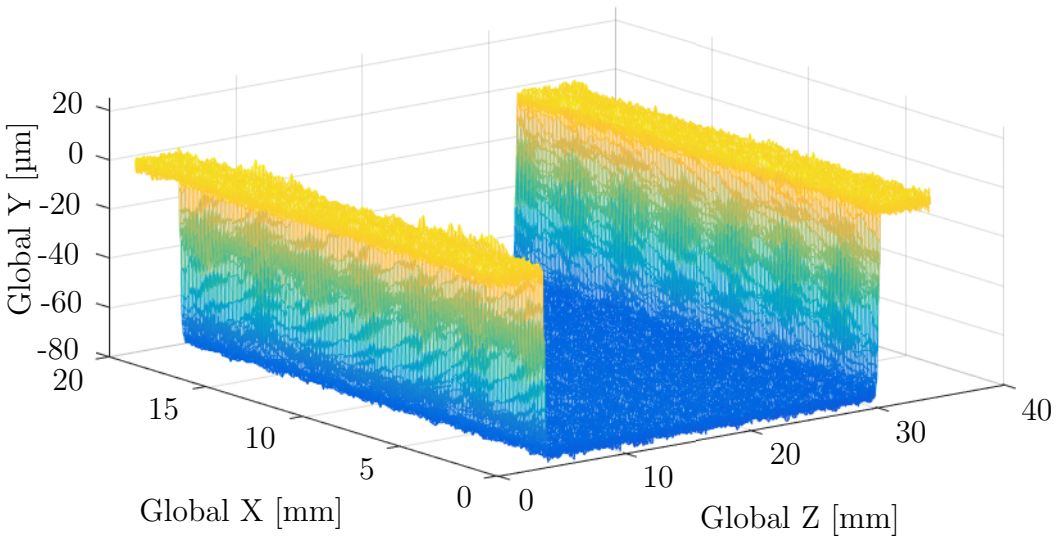

Figure 5.11: Compensated workpiece surface scan.

±10 µm, which shows that the kinematic error compensation is necessary to achieve the desired accuracy.

Figure 5.11 shows the surface cut by a grinding wheel trued with kinematic error compensation. The surface appears reasonably flat by inspection and was found to have a slope of 0.067 µm mm^{-1}. Therefore, over a wheel width of 26.7 mm, the wheel profile would have a maximum radial error of $\varepsilon_\rho = \pm 0.89$ µm from a perfect flat grinding wheel. This error is less than the resolution of the vertical stage encoder: 1.4 µm. The wheel had therefore been trued to within *EDGR*'s minimum theoretical accuracy.

Based on these results, it was concluded that the kinematic error compensation algorithm was implemented successfully. Validation of *EDGR*'s accuracy with kinematic error compensation for a profile grinding wheel was shown in Chapter 4. The results were not as successful as for the flat wheel case, although most of the errors were accounted for by errors in the tool geometry. The additional errors for a profile wheel compared to a flat wheel are understandable because many more sources of error exist for truing a profile grinding wheel, such as the tool geometry and the changing direction of the force applied to the tool tip.

5.5 Conclusions

In this section the kinematics of grinding wheel grooving were presented.

First, the kinematics of grooving a profile grinding wheel were discussed. Several equations were developed by the present author to analytically determine the feed rates necessary to groove a profile grinding wheel. It was concluded that a constant feed rate in the z direction can be used to create helical grooves for profile grinding wheels with radii above 300 mm and intermittent ratios greater than or equal to 0.5.

Next, the forward kinematics of *EDGR* were presented. Equations were developed to determine the position of the dressing tool given a set of joint values (stage positions).

The inverse kinematics were presented. A linear least-squares method was used to minimize position errors in Cartesian coordinates. The flaws in this method were discussed and the motivations for a kinematic error compensation algorithm were described.

A novel kinematic error compensation algorithm was developed to eliminate the radial and axial errors introduced by the misalignments between the grooving device and the grinding machine. A method of measuring the alignment of the grooving device axes with respect to the grinding machine axes was developed and described. Finally, the kinematic error compensation method was tested by truing a flat grinding wheel. It was found that, without kinematic error compensation, the grooving device produced unacceptable errors. However, when kinematic error compensation was applied, the grooving device could true a wheel to within its minimum theoretical accuracy.

Chapter 6

Performance of a Grooved Profiled Grinding Wheel

6.1 Introduction

The objective of the following experimental investigation is to determine the effects of helical grooves on a profile grinding process. To date, helical grooves have only ever been applied to flat grinding wheels. In this chapter, the performance of grooved and non-grooved profile grinding wheels is pushed to the limit until the grinding process reaches a failure point. The failure of the grinding process can happen in one of two ways: either the grinding wheel fails in what is referred to as "wheel breakdown" or the workpiece fails thermally in what is called "workpiece burn".

In wheel breakdown, the wheel structure fails and the grains are pulled out of the wheel, reducing its effective diameter and subsequently the depth of cut. The breakdown can be triggered by high forces, wheel temperatures, or wheel wear and is usually characterized by a decrease in forces and power and an increase in workpiece surface roughness. [1]

During grinding processes significant heat is generated by the cutting, ploughing and rubbing contact between the abrasive grains of the grinding wheel and the workpiece. The heat is generated at the contact zone between the wheel and workpiece and is dissipated into several locations: the workpiece, the environment (mostly to coolant), the chips removed from the workpiece, and the grinding wheel. The heat flow into the workpiece causes the workpiece temperature to rise. For steel workpieces, once a critical temperature is reached a phenomenon known as "workpiece burn" occurs where the physical properties of the workpiece change. The burn can be observed as visible discolorations on the workpiece surface or a change in workpiece hardness. Workpiece burn is one of the factors limiting the material removal rates of a grinding process. [39]

The benefits of grooves have been demonstrated for flat grinding wheels; however, their application has not yet been extended to profile grinding wheels. The mechanics

of profile grinding processes differ from flat grinding processes in several ways. Profile grinding wheels have a larger contact area with the workpiece compared to flat grinding wheels, which means a higher heat generation. Furthermore the geometry of the profile can affect the temperature distribution in the workpiece. Internal corners on the wheel (external corners on the workpiece) tend to experience higher temperatures than the surrounding workpiece. The forces during a profile grinding operation also differ from a flat grinding operation if the profile is not symmetrical. For asymmetrical profiles, an axial force is present between the wheel and the workpiece that can contribute to static deflection errors in the workpiece. [4]

6.2 Methods

The following experimental investigation was performed using a Blohm Planomat 408 grinding machine, pictured in Figure 6.1.

For these experiments a Radiac Abrasives WR-A-60-J-5-V aluminum oxide grinding wheel was formed to the profile shown in Figure 6.2. The profile selected for these experiments was asymmetrical to ensure that measurable axial forces would be present during the profile grinding process.

Figure 6.1: Blohm Planomat 408 grinding machine.

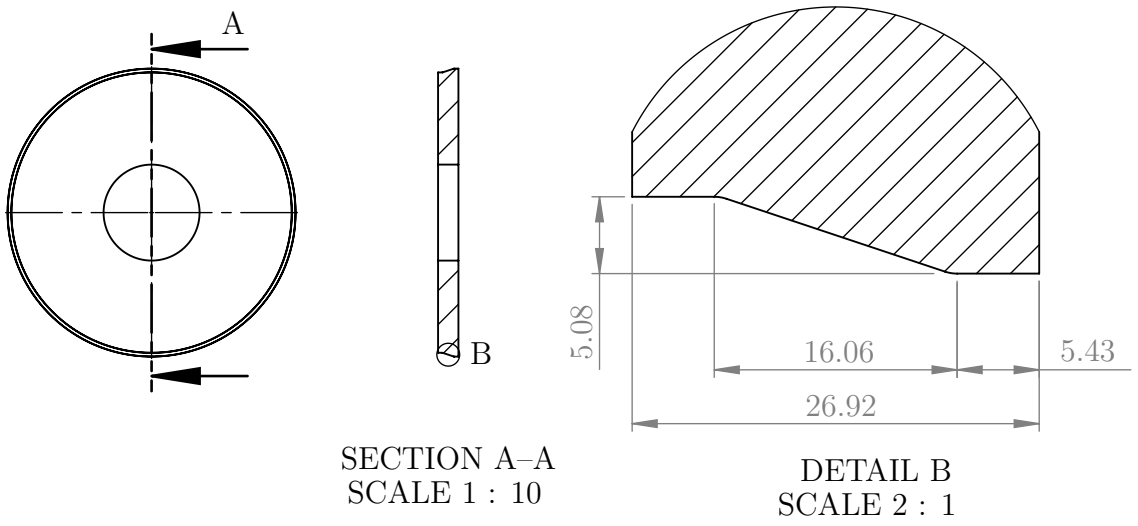

Figure 6.2: Engineering drawing of the simple wheel profile used for the experimental investigation. Units are millimeters.

The workpiece was a 1018 steel plate 19.05 mm wide and 101.6 mm long, mounted on a Kistler 9257B Multicomponent Dynamometer. The signals from the Dynamometer were amplified using a Kistler 5019B Charge Amplifier and the amplified signals were measured by a National Instruments PCI-MIO-16XE-10 data acquisition board at 250 Hz. A photograph of the experimental setup is shown in Figure 6.3.

The experimental conditions are summarized in Table 6.1. Each test consisted of a single grinding pass at a constant depth of cut, with a feed rate of 101.6 mm/min, and an average wheel surface speed of 20.4 m/s. Due to the diameter of the profiled wheel varying across its width, the surface speed at the largest radius of the wheel was approximately 20.55 m/s and the surface speed at smallest radius of the wheel was approximately 20.25 m/s.

The desired groove lead used for the grooved set of tests was $L_g = 1920\ \mu\text{m}\,\text{rev}^{-1}$ which gives a groove helix angle of $\alpha_g = 89.9°$. The groove depth was $a_g = 100\ \mu\text{m}$ and it was cut by grooving the grinding wheel in eight, 12.5 µm increments. The depth was chosen based on the smallest groove depth seen in the literature for the single-point grooving method. The groove width varied depending on the slope of the grinding wheel profile, due to the dressing tool geometry. The maximum groove width of $a_g = 820\ \mu\text{m}$ was present on the flat sections of the wheel profile and the

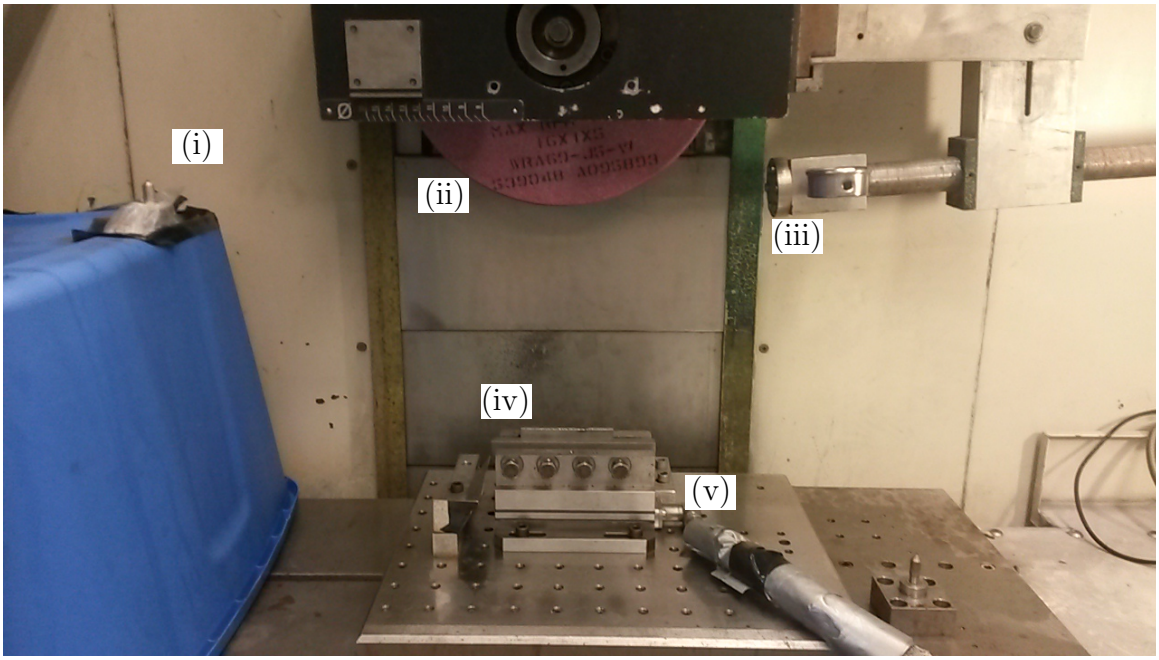

Figure 6.3: Experimental setup for the profile grinding experimental investigation showing (i) *EDGR* inside of its protective shell, (ii) the grinding wheel mounted on the grinding machine spindle, (iii) the coolant jet nozzle, and (iv) the workpiece mounted on top of (v) the dynamometer.

Property	Value	
Min. Wheel Surf. Speed	20.55	$\mathrm{m\,s^{-1}}$
Avg. Wheel Surf. Speed	20.40	$\mathrm{m\,s^{-1}}$
Max. Wheel Surf. Speed	20.25	$\mathrm{m\,s^{-1}}$
Feed Rate	101.6	$\mathrm{mm\,min^{-1}}$
Min. Avg. Wheel Dia.	357.2	mm
Max. Avg. Wheel Dia.	362.8	mm
Groove Depth	100	µm
Min. Groove Width	390	µm
Max. Groove Width	820	µm
Groove Lead	1920	$\mathrm{\mu m\,rev^{-1}}$
Number of Starts	1	
Dressing Tool Radius	230	µm
Dressing Overlap Ratio	3.0	

Table 6.1: Summary of experimental conditions used for the profile grinding experiments.

minimum groove width of $a_g = 390$ µm was present on the inclined section of the wheel profile. These conditions were chosen so that the groove factor of the inclined section of the profile was $\eta_g = 80\%$ and the groove factor on the flat sections of the profile was $\eta_g = 57\%$. This groove geometry is similar to the geometry used by Mohamed *et al.* [17], although the groove factor selected is higher (less groove area) than the groove factors selected by those authors. A photograph of the grooved profile grinding wheel surface is shown in Figure 6.4. The groove lead was measured on the grinding wheel and was found to be $L_g = 1.99 \pm 0.08$ mm rev^{-1}.

The coolant used was a 5.1% mixture of CIMTECH 310 in water. The concentration of the coolant was monitored between tests and coolant was added to maintain a consistent concentration for all tests. Before the tests were conducted the workpiece

Figure 6.4: Photograph of a grooved profile grinding wheel.

was profiled to ensure that the contact between the grinding wheel and the workpiece was consistent for every test. Before each test the workpiece was ground lightly with several sparkout passes to ensure that the depth of cut for each test was accurate. Between each test the grinding wheel was dressed and trued, removing 0.05 mm in 0.0125 mm increments using a dressing tool with a nose radius of 0.227 mm and an overlap ratio of 3. For tests using a grooved wheel, the wheel was re-grooved between each test to ensure a consistent groove width and depth for each test.

During each test the forces on the workpiece and the spindle power were recorded. After each test the workpiece surface arithmetic average roughness R_a was measured using a Mahr Federal PocketSurf portable surface roughness tester. The roughness measurements were made on the inclined face of the workpiece with the roughness profiles taken along the z-direction with a cut-off length of 5 mm. Three R_a roughness measurements were taken: at the start, middle and end of the workpiece. These measurements were then averaged to obtain the average R_a for the entire workpiece.

6.3 Results and Discussion

Two sets of tests were performed: one for a conventional profiled wheel and one for a grooved profiled wheel. For each set, the depth of cut was increased until evidence of workpiece damage or wheel breakdown was detected. The depths of cut and feed rate used in these tests would be considered creep-feed grinding. A summary of the cutting conditions for each test is given in Table 6.2. In this table, the workpiece for each test is also indicated. The workpiece used for the conventional grinding experiments (W1 in Table 6.2) was kept for further analysis and a new workpiece of the same material (W2 in Table 6.2) was used for the grooved grinding tests; however, the grooved grinding tests exceeded expectations in terms of workpiece material removal and could not be completed with a single workpiece. Therefore the last three tests were performed using a third and final workpiece of the same material (W3 in Table 6.2).

The results of both sets of tests are shown in Figures 6.5, 6.6, and 6.7. Each plot shows various performance parameters plotted against the material removal rate (MRR) The markers in these figures that are indicated with an "X" are the trials in which process failure was detected. The trend lines plotted for each dataset do not

Test	Workpiece [mm]	Depth of Cut [mm]	MRR [$mm^3\,min^{-1}$]	Wheel Dia.
C1	W1	0.05	97	362.8
C2	W1	0.10	194	362.4
C3	W1	0.15	290	362.3
C4	W1	0.20	387	362.2
C5	W1	0.25	484	362.1
C6	W1	0.30	581	362.0
C7	W1	0.35	677	361.8
C8	W1	0.40	774	361.7
G1	W2	0.10	194	358.7
G2	W2	0.20	387	358.6
G3	W2	0.30	581	358.5
G4	W2	0.40	774	358.4
G5	W2	0.50	968	358.3
G6	W2	0.60	1161	358.2
G7	W2	0.70	1355	358.1
G8	W2	0.80	1548	357.0
G9	W2	0.90	1742	357.9
G10	W3	1.00	1936	357.6
G11	W3	1.10	2129	357.5
G12	W3	1.20	2322	357.2

Table 6.2: Summary of experimental depths of cut and wheel diameters. C# tests indicate conventional wheel tests white G# tests indicate grooved wheel tests.

include the trials marked with an "X".

The first, most obvious conclusion from the data presented in the following four figures is that the grooved wheel allowed a depth of cut approximately three times deeper than the conventional wheel before workpiece damage occurred. This result is similar to the results in Mohamed *et al.* [17], where the grooved flat grinding wheel allowed twice the depth of cut compared to a conventional flat grinding wheel.

Figure 6.5 shows the maximum forces experienced by the workpiece versus the material removal rate of each test. The process forces for a grooved wheel are clearly significantly lower than the process forces for a conventional wheel. Conventional versus grooved grinding experiments for flat grinding wheels by other authors have shown reduced normal and tangential forces, so this result is not surprising. The interesting result, which has not yet been reported in the literature, is that the axial forces are also significantly lower for a profile grinding wheel. The reasons for the decreased axial forces are likely the same reasons for the decreased normal and tangential forces: an increase in uncut chip thickness and improved coolant flow to the contact zone for grooved grinding wheels.

Figure 6.6(a), shows the maximum spindle power and Figure 6.6(b) shows the specific energy.

From Figure 6.6(a), it can be seen that the grooved grinding wheel reaches a higher spindle power before process failure occurs. The maximum spindle power measured for the grooved grinding wheel was 30% larger than the maximum spindle power measured for the conventional grinding wheel. The workpiece burn is dependent on the amount of heat transferred to the workpiece, therefore, a grooved profile grinding wheel transfers at a maximum $1/1.30 = 77\%$ as much heat to the workpiece as a conventional profile grinding wheel. The heat transfer to the workpiece could be even lower; however, the grooved grinding wheel experienced wheel breakdown before workpiece burn could be achieved.

The specific energy is a measure of the efficiency of the grinding process. It is defined as the amount of energy required to remove a unit volume of material from the workpiece. Lower specific energy indicates a more efficient grinding process. From Figure 6.6(b) it is clear that the specific energy for the grooved profile grinding wheel is approximately 50% as large as the specific energy for the conventional profile grinding

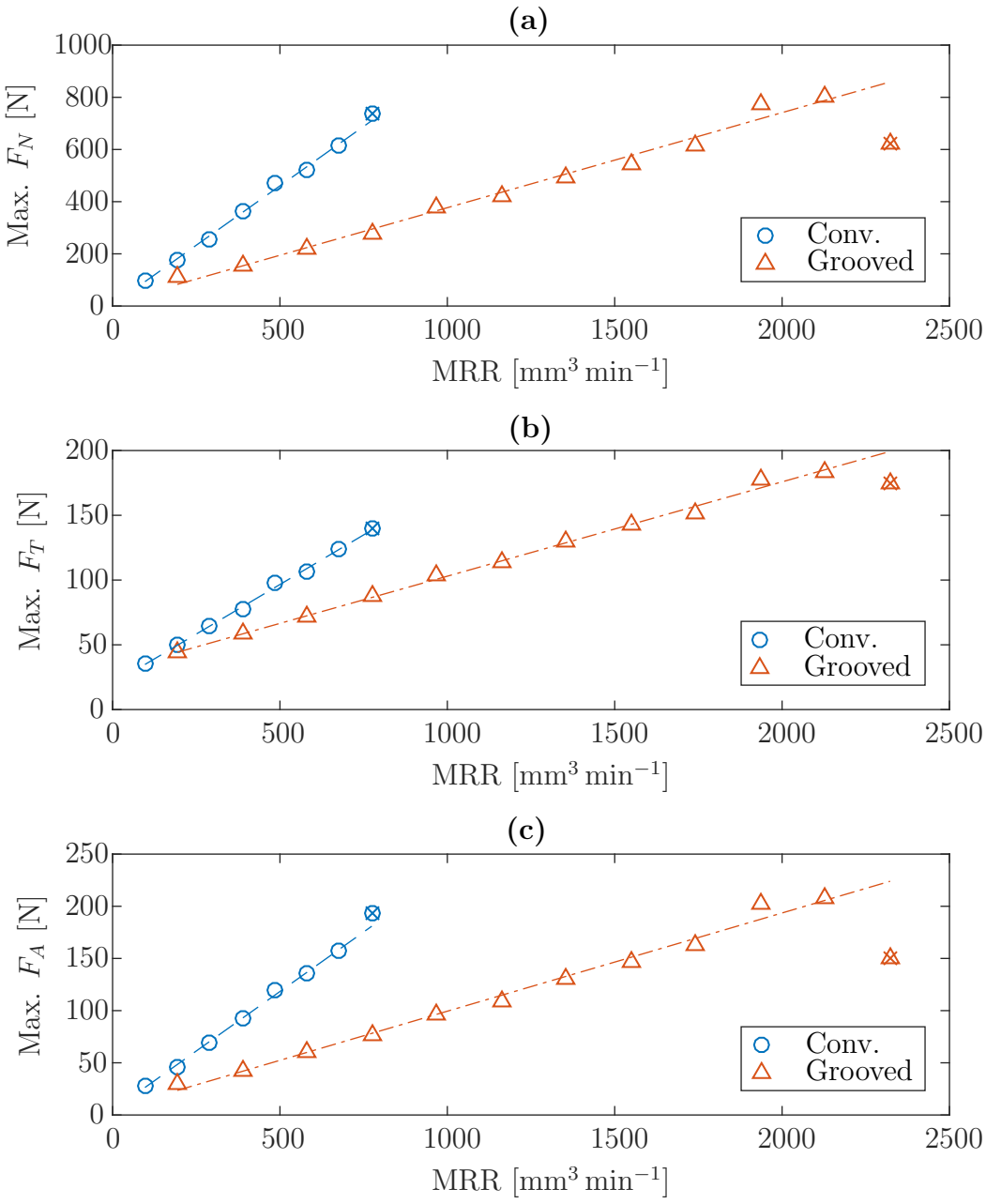

Figure 6.5: Maximum forces measured during profile creep-feed grinding with conventional and grooved profile grinding wheels in the (a) normal, (b) tangential and (c) axial directions.

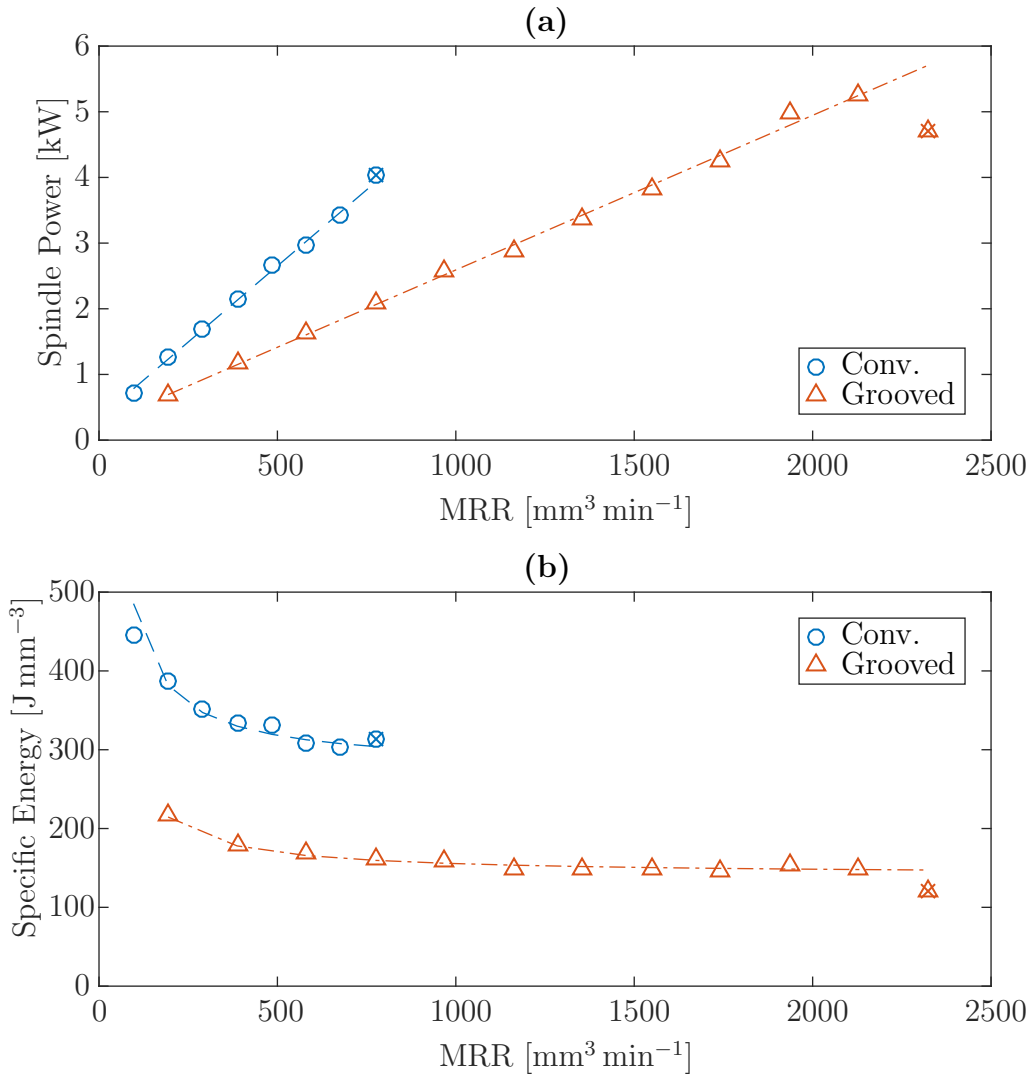

Figure 6.6: (a) Maximum spindle power during profile creep-feed grinding with conventional and grooved grinding wheels. (b) Specific energy of the grinding process, which is calculated by dividing the spindle power in (a) by the material removal rate.

wheel. Furthermore, the grooved grinding wheel appears to reach an asymptote in its specific energy. For a grooved profile grinding wheel the efficiency becomes practically independent of the material removal rate between 1000 $\mathrm{mm^3\,min^{-1}}$ and 2300 $\mathrm{mm^3\,min^{-1}}$ (after which workpiece damage occurs). Conversely, the conventional workpiece causes workpiece damage before it reaches a similar asymptote. The critical specific energy, or the specific energy before failure occurred, was 313 $\mathrm{J\,mm^{-3}}$ for the conventional profile grinding wheel and 148 $\mathrm{J\,mm^{-3}}$ for the grooved profile grinding wheel.

Figure 6.7 shows the workpiece arithmetic average surface roughness R_a, which is defined as the average of the absolute deviations from the mean surface.

From Figure 6.7 it can be seen that the surface roughness for the conventional profile grinding wheel is within the limit for what would be considered a "fine" grinding surface finish. The workpiece surface roughness generated by a grooved profile grinding wheel is just above the limit for a "fine" surface finish. This increased surface roughness might be explained by the surface texture introduced by the grooves. Using equations from Mohamed *et al.* [13] the height of the workpiece surface texture was calculated as $R_{t,g} = 0.003$ µm which should result in an additional R_a of approximately 0.0008 µm. The resolution of the PocketSurf is 0.01 µm; therefore,

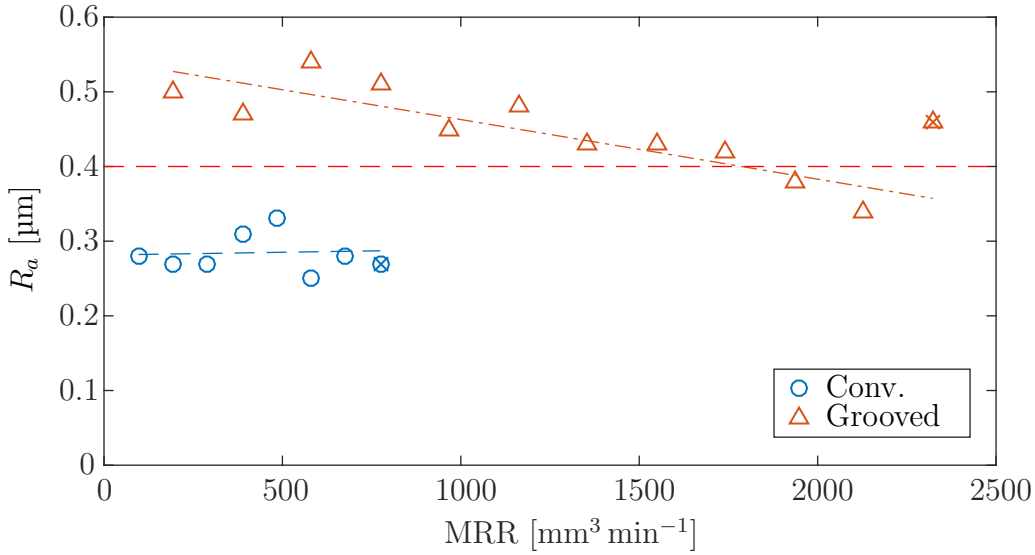

Figure 6.7: Plot showing the average workpiece absolute roughness after grinding. The dashed line indicates the limit for a "fine" grinding surface roughness.

the additional roughness due to the groove texture is negligibly small. Therefore, the groove texture does not account for the approximately 0.20 µm difference seen in Figure 6.7. The increase in roughness could also be attributed to the wear of the dressing tool which would decrease its nose radius and, therefore, reduce the dressing overlap ratio. However, if that were the case it would be expected that there would be a slowly increasing trend in the surface roughness for all trials regardless of a grooved or conventional wheel being used. The most likely explanation for the better surface roughness for the non-grooved wheel is that the non-grooved has more cutting edges, with multiple edges running over the same location on the workpiece multiple times.

The workpiece surface roughness for a grooved grinding wheel shows a decreasing trend with increasing material removal rate. The first four data points show a relatively flat trend, but a decreasing trend becomes clear after a material removal rate of approximately 950 $\mathrm{mm^3\,min^{-1}}$. Interestingly, this is also the point at which the specific energy curve for the grooved grinding wheel reaches an asymptote. The decreasing trend could be explained by increased grinding wheel wear at higher material removal rates. The increase in attritious wear would create duller grits that would produce a finer surface finish.

More information towards identifying the causes of the workpiece surface roughness behaviour could be obtained via scans of the workpiece surface. Surface scans would reveal whether the roughness has a periodic nature to it, which would suggest either the groove geometry or possibly chatter to be at fault for the higher surface roughness for the grooved grinding wheel. However, that work has not been completed in time to be included in this manuscript.

One further observation can be made about the differing performance of the grooved and conventional profile grinding wheels: not only did the grooved profile grinding wheel show evidence of failure at a much higher material removal rate, but it also experienced a completely different type of failure in a completely different location. To examine the nature of the process failure, photographs were taken of the ground surfaces of both workpieces. Figure 6.8 shows a photograph taken of the workpiece after it was burned by a conventional profile grinding wheel.

Figure 6.8 shows that the workpiece burn occurred in the corners of the workpiece profile, as was hypothesized. The damage also occurred towards the end of the

workpiece. The damage appears clearly as discolourations on the workpiece surface. The point of failure can be seen in the plot of the grinding power versus time shown in Figure 6.9.

Figure 6.9 shows the spindle power versus time for a conventional profile grinding

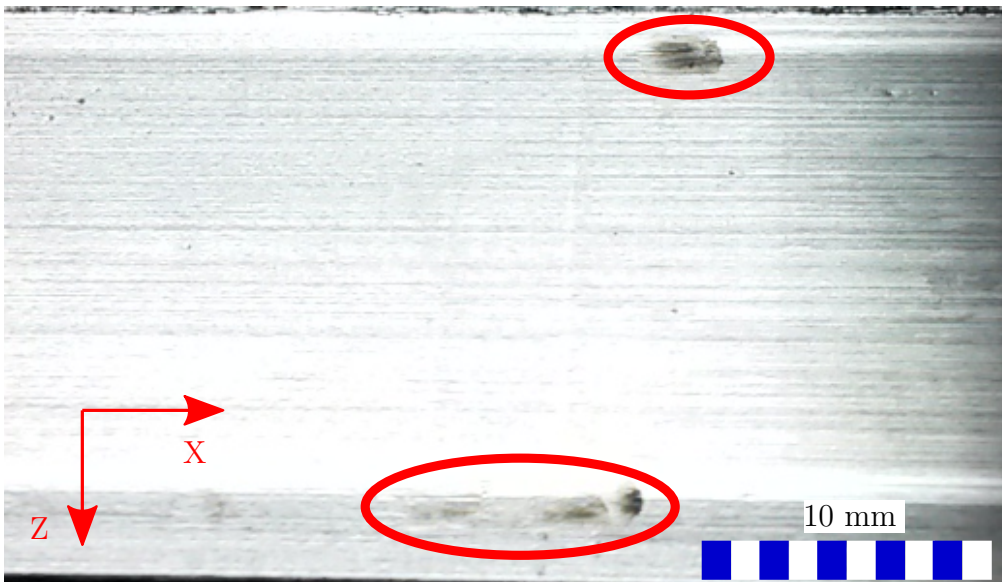

Figure 6.8: Photograph of a burned workpiece ground by a conventional profile grinding wheel. The damaged areas are circled. The absolute coordinates of the grinding machine are shown in the bottom-left corner.

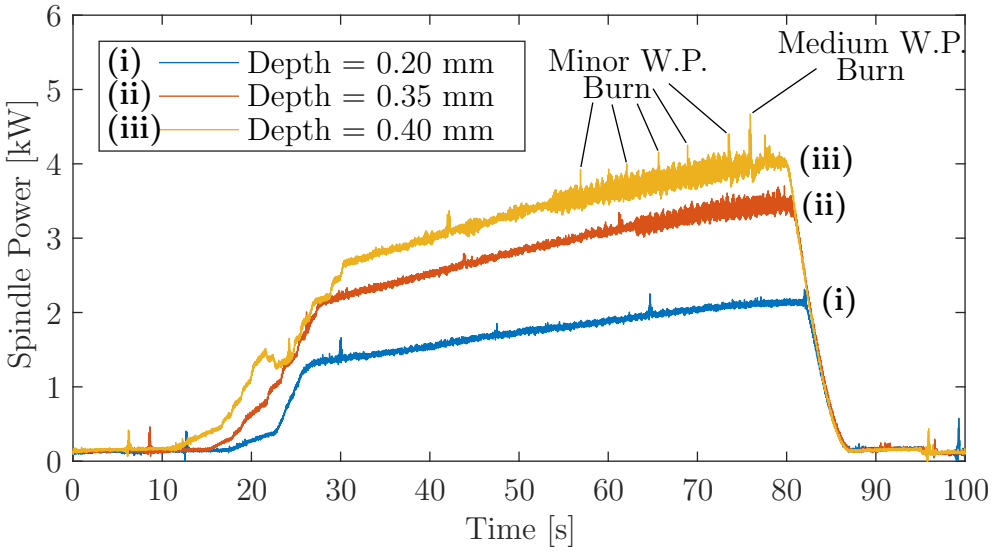

Figure 6.9: Plot of raw power vs. time for a conventional profile grinding wheel for three different depths of cut.

wheel at three different depths of cut: 0.40 mm, where visible workpiece burn occurred; 0.35 mm, where there was no visible workpiece damage; and 0.20 mm where there was no evidence of workpiece damage. In the figure, for all depths of cut the power increases from the no-load power as the wheel makes contact with the workpiece. After the wheel makes full contact with the workpiece the power continues to slowly increase. The slow increase in power over time is due to the attritious wear of the grinding wheel grains as they cut the workpiece, causing increased rubbing and ploughing. The deeper depths of cut show a higher rate of power increase which indicates that the wear is occurring more quickly. Finally the spindle power drops as the wheel leaves contact with the workpiece.

From Figure 6.9 it can be seen that the noise in the spindle power signal increases towards the end of the cut for the 0.35 mm and 0.40 mm depths of cut. The increase in noise could be due to hardening of the workpiece causing chatter, which may not necessarily appear as visible workpiece damage. Both depths of cut begin to show increased spindle power noise at around 3.1 kW. The similar point of noise increase suggests that 3.1 kW may be a critical power over which workpiece hardening begins; however, hardness tests would be necessary to confirm this hypothesis.

Workpiece burn can often be identified by sudden spikes in the spindle power. There is some environmental noise that appears in all of the signals as 0.3 kW spikes approximately every 18 seconds, even when the wheel is not contacting the workpiece; therefore, these regularly occuring small spikes can be ignored. The only non-negligible power spikes can be seen for the 0.40 mm depth of cut. The unexplained power spikes are indicated in Figure 6.9. However, the only the last two burn spikes correspond to the burn marks at the top and bottom profile corners that were seen in Figure 6.8. There was no visible workpiece damage closer to the start of the workpiece that might correspond with the other power spikes.

The workpiece burn occurs towards the end of the workpiece. The reason for the location of the burn is likely the placement of the coolant jet. The coolant jet is targeted at the grinding zone so that it is approximately half on the wheel, half on the workpiece at the bottom dead center of the wheel, as shown in Figure 6.10.

While the wheel cuts in the middle of the workpiece, the part of the coolant jet that “intersects” the workpiece is directed into the grinding zone by the top face of

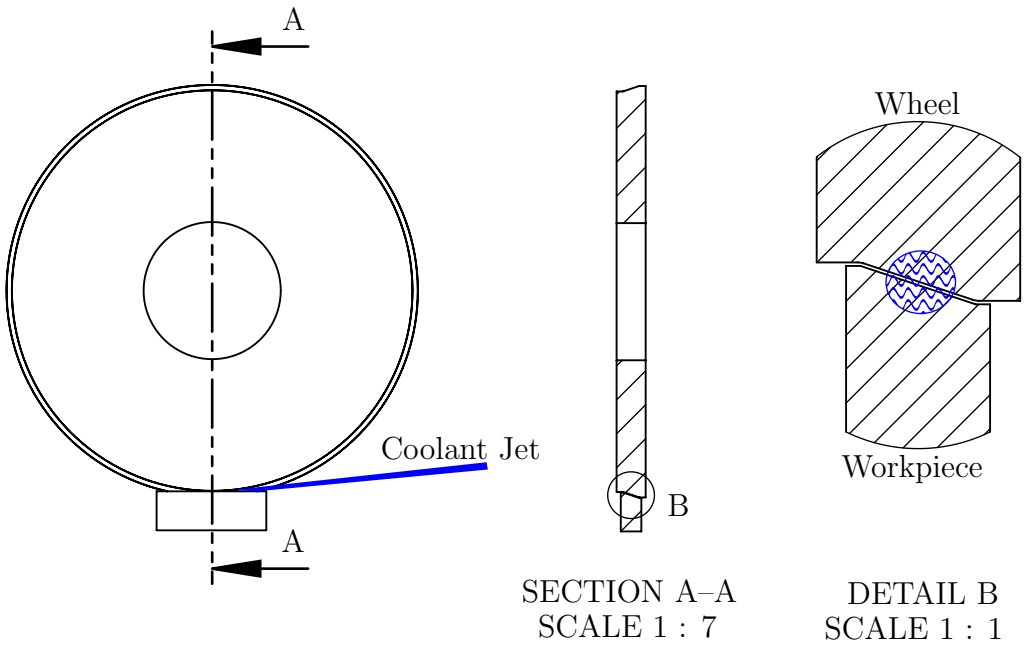

Figure 6.10: Diagram of coolant jet placement.

the workpiece. However, as the grinding wheel reaches the end of the workpiece, the coolant jet starts to collide with the end face of the workpiece and is directed away from the grinding zone. Now less coolant volume is entering the grinding zone, which reduces the amount of heat that can be transferred away from the grinding zone and increases the amount of heat being absorbed by the workpiece, potentially causing burn.

Interestingly, the grooved wheel experienced process failure in a completely different location. Figure 6.11 shows the spindle power for the grooved grinding wheel at three different depts of cut.

There are a few interesting features in Figure 6.11 that differ from Figure 6.9. Firstly, the noise in the test with a depth of cut of 1.20 mm increases dramatically shortly after the grinding wheel makes full contact with the workpiece. Secondly, after the increase in noise, the spindle power levels off compared to the previous test at a depth of 1.10 mm finishing at a lower maximum power. In fact, there was a significant drop in the maximum forces compared to previous tests as well, which

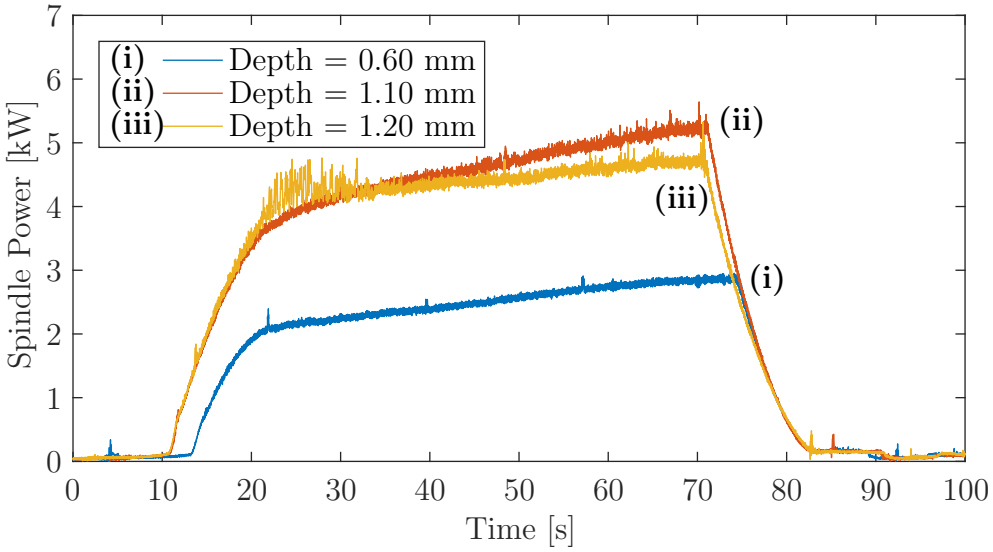

Figure 6.11: Plot of raw power vs. time for a grooved profile grinding wheel for three different depths of cut.

can be seen in Figure 6.5. Furthermore, this drop in forces was accompanied by an sudden increase in the surface roughness compared to previous tests, as can be seen in Figure 6.7.

The most likely explanation for the drop in forces and increase in roughness would be wheel breakdown. In the case of the grooved grinding wheel tests shown in Figure 6.11, the wheel breakdown occurs after or during the increase in spindle power noise. Mohamed *et al.* [40] showed that the workpiece can experience a spike in temperature when the grinding wheel begins to contact the workpiece. The temperature spike could have initiated the wheel breakdown. The initial temperature spike would explain why the forces and spindle power where the wheel breakdown occurred were smaller than the forces and spindle power reached by the previous trial. The breakdown might have also been the cause of the chatter (noise) visible in Figure 6.11. The grinding wheel structure is relatively brittle; therefore, impact loads are more destructive than static loads which might have further accelerated the wheel breakdown. This conclusion is supported by evidence of chatter on the wheel surface, pictured in Figure 6.12.

In Figure 6.12, there are scale-like marks in the workpiece at the start of the workpiece where the increased spindle power noise was measured. The marks are very

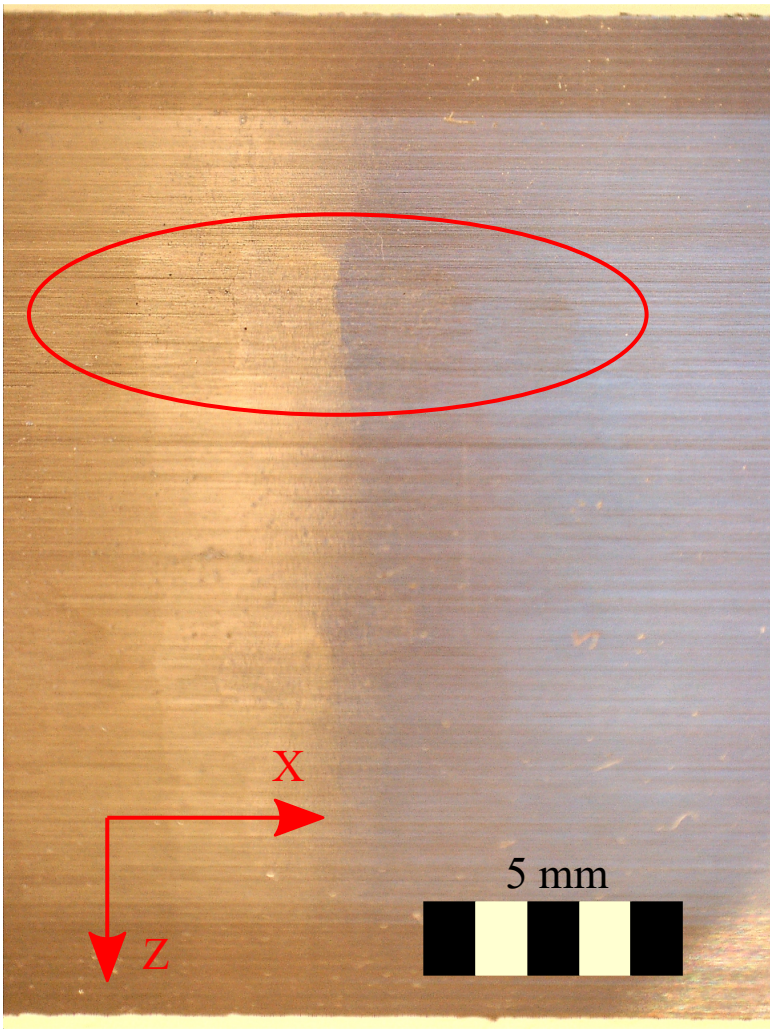

Figure 6.12: Photograph of the workpiece surface for test G12. Scale-like marks are indicated with a red circle, possible evidence of chatter.

fine so it was difficult to capture them photographically on the near-polished surface of the workpiece due to its high reflectivity. There are no visible discolourations to indicate the occurrence of workpiece burn.

6.4 Conclusions and Recommendations

In this chapter an experimental investigation into the effects of helical grooves on a profile grinding process was presented. Several conclusions can be drawn from this investigation, as well as some areas of future improvement.

The grooved profile grinding wheel was capable of much deeper depths of cut before process failure occurred compared to a conventional profile grinding wheel. The grooved grinding wheel was capable of reaching a depth of cut of 1.20 mm, whereas the conventional grinding wheel was only capable of reaching a depth of cut of 0.40 mm before workpiece burn occurred.

The grooved profile grinding wheel produced much lower process forces and spindle power compared to the conventional profile grinding wheel. Furthermore, the grooved grinding wheel supported 30–40% larger forces and a 50% larger spindle power before process failure occurred. The higher forces before failure indicate that not only does the grooved wheel generate less heat, but it also transfers less heat to the workpiece compared to a conventional grinding wheel.

The specific energy of the grooved profile grinding process was found to be 50% of the magnitude of the specific energy for a conventional profile grinding process. The smaller specific energy indicates a more efficient grinding process.

The grooved grinding wheel was also found to produce a higher surface roughness than the conventional grinding wheel. The conventional grinding wheel was capable of producing a fine surface finish, while the grooved wheel produced a surface finish just above the limit for a fine grinding surface finish.

The grooved profile grinding wheel and the conventional profile grinding wheel failed in different ways in different locations. The conventional grinding wheel caused workpiece burn towards the end of the workpiece. The grooved grinding wheel experienced wheel breakdown before workpiece burn was observed. The wheel breakdown occurred at the start of the workpiece and is believed to be caused by chatter.

6.4.1 Recommendations and Future Areas of Investigation

The experimental investigation presented in this chapter could be improved in several ways.

Firstly, the experimental results would greatly benefit from repeatability testing. At least three sets of tests to failure should be conducted for the conventional grinding wheel and grooved grinding wheel. Repeated tests would show whether the process failure observed in this investigation occur at consistent forces and temperatures.

Secondly, the grooved tests had to be performed on two separate workpieces due to more workpiece material being removed than was anticipated. It would be better to perform each set of tests on a single workpiece, to eliminate the possible effects of material property variations between workpieces.

Another improvement would be to perform workpiece scans with a profilometer. There was an unexplained increase in surface roughness for the grooved profile grinding wheel. Workpiece scans could shed some light on the reason for the increase in surface roughness.

The profile that was used in this investigation was a simple profile that was not based on a particular industrial application. It would be more interesting to demonstrate improvements for a more complicated profile with a specific industrial application, such as the profile of a turbine blade root or the races of a ball bearing.

It would be interesting to investigate whether the groove geometry can control the failure mode of the grinding process. For example, the groove factor could be decreased until workpiece burn was observed. Or it could be investigated whether grooves are only needed in the corners of the workpiece profile, where the burn occurred for the conventional profile grinding wheel. Or an investigation could be performed to see if the direction of the groove helix has any effect on the forces, power or process failure. On a flat wheel the direction of the groove should not make a difference because there is no variation in workpiece geometry across the wheel width. However, with an asymmetrical profile the workpiece does have a varying geometry across the wheel width. Therefore the direction of the groove might have an effect.

Chapter 7

Conclusion

The main objectives of this work have been completed.

The first objective was to conduct a review of the state-of-the-art of grinding wheel grooving methods. In Chapter 3 a comprehensive review of state-of-the-art grinding wheel grooving methods and the performance of grooved vitrified bond grinding wheels was presented. Several conclusions were drawn in this chapter. Firstly, grooved grinding wheels have been applied to a variety of grinding processes and workpiece materials. A variety of groove geometries have also been tested, with the vast majority of authors investigating grinding wheels with low helix angles and large numbers of grooves. Grooved grinding wheels have been conclusively shown to reduce process forces, process temperatures and specific energies; however, the exact relationships between groove geometry and resulting performance remain largely unknown.

The second objective was to design, build and validate a grooving device capable of producing helical grooves on a profile grinding wheel. Chapter 4 described the design, construction and validation of a grinding wheel grooving device capable of producing helical grooves on a profile grinding wheel. A brief experimental investigation into the forces experienced by a single-point dressing tool during grooving was conducted in order to determine the sizing requirements of the actuators of the grooving device. The largest measured forces were in the tangential and normal directions to the wheel, which reached an average force of approximately 70 N. The average force in the axial direction of the wheel was found to be relatively small, reaching a maximum of approximately 10 N. There was a significant dynamic noise component in all of the force signals that increased with increasing depth of cut. The RMS amplitudes of the dynamic component of the forces reached a maximum of approximately 180 N. From this investigation it was concluded that there was a significant advantage to grooving devices that can produce deep grooves in multiple shallow cuts instead of taking a single deep grooving pass. The design of the grooving device was presented

and its positional accuracy was validated by truing a flat grinding wheel and forming a profile grinding wheel. The grooving device was found to meet the requirements for its positional accuracy of ±10 µm, but only after the wear of the dressing tool was accounted for.

In Chapter 5, the solution to the grooving devices forward and inverse kinematics was presented, along with a kinematic error compensation method. It was concluded that for grinding wheels with diameters exceeding 300 mm, helical grooves could be produced by moving the dressing tool along the axis of the wheel at a constant speed because the resulting variation in helix angle with wheel radius was small enough to be ignored. A kinematic error compensation method was created to reduce the ideal positioning errors of the grooving device along the radial and axial directions of the grinding wheel to zero. In addition, a method of measuring the alignment errors was developed. The kinematic error compensation method was tested as a part of the design validation and was shown to reduce errors in the tool position to within the design accuracy requirements. It was demonstrated that without the kinematic error compensation the grooving device would not have been capable of meeting the accuracy requirements.

The third and final objective was to demonstrate the performance of a grooved profile grinding wheel and compare it to the performance of a non-grooved profile grinding wheel. In Chapter 6 an experimental investigation was conducted to compare the performance of a grooved grinding wheel to a non-grooved profile grinding wheel by profile grinding a workpiece at increasing depths of cut until process failure occurred. The grooved grinding wheel was found to be capable of taking a depth of cut three times larger than the non-grooved grinding wheel before process failure occurred. Furthermore, the non-grooved profile grinding process failed due to workpiece burn, while the grooved profile grinding process failed due to wheel breakdown. The grooved grinding wheel showed significantly lower process forces and spindle power compared to the conventional grinding wheel. Furthermore, the grooved grinding wheel supported forces that were 30%–40% higher and spindle power that was 50% larger than the conventional profile grinding wheel before failure occurred. The higher forces and power before failure indicate that the grooved grinding wheel transfers less heat to the workpiece in addition to generating less heat than a conventional grinding

wheel. The specific energy of the grooved grinding wheel was found to be 50% lower than the conventional grinding wheel. The grooved grinding wheel was found to produce a worse workpiece surface roughness than the non-grooved grinding wheel. The grooved grinding wheel produced a surface roughness between 0.35 µm and 0.55 µm whereas the non-grooved wheel produced a surface roughness between 0.25 µm and 0.35 µm.

The contributions of this work were as follows:

- A comprehensive review of groove production methods and grooved grinding performance using parts from Chapter 2 and Chapter 3 was published as a survey paper in the *International Journal of Advanced Manufacturing Technology*.

- A novel grooving device was designed and built to produce helical grooves on a profile grinding wheel. It is the first grooving method/device capable of creating helical grooves on a profile grinding wheel in the world. A conference paper on the design of the device was presented at the *26th Canadian Congress of Applied Mechanics*.

- A novel kinematic error compensation method was designed and implemented. The method was shown to be successful in compensating for the misalignment between the grooving device and the grinding machine.

- An experimental investigation was conducted comparing the performance of grooved profile grinding and non-grooved profile grinding.

7.1 Recommendations for Future Work

Many areas of future investigation were identified in this work. A list of these future areas of investigation is presented here.

- Investigate the economics of implementing grooving processes in an industrial setting (process times, tool wear, materials consumed, energy consumed).

- Investigate the relative importance of each element of the groove geometry (helix angle, width, depth, groove factor).

- Improve the design of the prototype profile grooving device, according to the recommendations made in Chapter 4.
- Perform more profile grinding experiments with the same conditions presented in Chapter 6 to establish the repeatability of the grooved wheel performance compared to the non-grooved wheel performance.
- Perform grooved profile grinding experiments with a profile that is industrially relevant.
- Perform scans of profile ground workpieces from both grooved and non-grooved grinding processes.
- Investigate whether groove geometry can be "tuned" to select the process failure mode (either wheel breakdown or workpiece burn).

Bibliography

[1] M. Groover, *Fundamentals of Modern Manufacturing: Materials, Processes and Systems*. John Wiley & Sons Inc., 5th ed., 2013.

[2] J. Oliveira, E. Silva, C. Guo, and F. Hashimoto, "Industrial challenges in grinding," *CIRP Annals – Manufacturing Technology*, vol. 58, no. 2, pp. 663–680, 2009.

[3] C. Forbrigger, R. Bauer, and A. Warkentin, "A review of state-of-the-art vitrified bond grinding wheel grooving processes," *The International Journal of Advanced Manufacturing Technology*, vol. 90, no. 5–8, pp. 2207–2216, 2017.

[4] E. Saljé, H.-H. Damlos, and H. Teiwes, "Problems in profile grinding – angular plunge grinding and surface grinding," *CIRP Annals – Manufacturing Technology*, vol. 30, no. 1, pp. 219–222, 1981.

[5] D. Anderson, A. Warkentin, and R. Bauer, "Experimental and numerical investigations of single abrasive-grain cutting," *International Journal of Machine Tools and Manufacture*, vol. 51, no. 12, pp. 898–910, 2011.

[6] "Gas turbine blade with details." `https://commons.wikimedia.org/wiki/File%3AGas_turbine_blade_with_details.jpg`. Accessed: 2017-05-21.

[7] B. Denkena, L. de Leon, and B. Wang, "Grinding of microstructured functional surfaces: a novel strategy for dressing of microprofiles," *Production Engineering*, vol. 3, no. 1, pp. 41–48, 2009.

[8] H. N. Li and D. Axinte, "Textured grinding wheels: A review," *International Journal of Machine Tools and Manufacture*, vol. 109, pp. 8–35, 2016.

[9] C. Forbrigger, A. Warkentin, and R. Bauer, "Development of a multi-axis CNC grinding wheel grooving device," *Proceedings of the 26th Canadian Congress of Applied Machining*, p. 022, 2017.

[10] J. F. G. Oliveira, A. C. Bottene, and T. V. França, "A novel dressing technique for texturing of ground surfaces," *CIRP Annals – Manufacturing Technology*, vol. 59, no. 1, pp. 361–364, 2010.

[11] U. Çiftçi, "A generalization of Lancret's theorem," *Journal of Geometry and Physics*, vol. 59, no. 12, pp. 1597–1603, 2009.

[12] J. Verkerk, "Slotted wheels to avoid cracks in precision grinding," in *Abrasive Engineering Society Conference*, pp. 75–81, 1979.

[13] A.-M. Mohamed, A. Warkentin, and R. Bauer, "Prediction of workpiece surface texture using circumferentially grooved grinding wheels," *The International Journal of Advanced Manufacturing Technology*, vol. 89, no. 1–4, pp. 1149–1160, 2017.

[14] D. Aslan and E. Budak, "Surface roughness and thermo-mechanical force modeling for grinding operations with regular and circumferentially grooved wheels," *Journal of Materials Processing Technology*, vol. 223, pp. 75–90, 2015.

[15] T. Suto, T. Waida, H. Noguchi, and H. Inoue, "High performance creep feed grinding of difficult-to-machine materials with new-type wheels," *Bulletin of the Japan Society of Precision Engineering*, vol. 24, no. 1, pp. 39–44, 1990.

[16] J.-D. Kim, Y.-H. Kang, D.-X. Jin, and Y.-S. Lee, "Development of discontinuous grinding wheel with multi–porous grooves," *International Journal of Machine Tools and Manufacture*, vol. 37, no. 11, pp. 1611–1624, 1997.

[17] A.-M. O. Mohamed, R. Bauer, and A. Warkentin, "Application of shallow circumferential grooved wheels to creep-feed grinding," *Journal of Materials Processing Technology*, vol. 213, no. 5, pp. 700–706, 2013.

[18] A.-M. Mohamed, R. Bauer, and A. Warkentin, "A novel method for grooving and re-grooving aluminum oxide grinding wheels," *The International Journal of Advanced Manufacturing Technology*, vol. 73, no. 5–8, pp. 715–725, 2014.

[19] K. Nakayama, J. Takagi, and T. Abe, "Grinding wheel with helical grooves - an attempt to improve the grinding performance," *CIRP Annals – Manufacturing Technology*, vol. 26, no. 1, pp. 133–138, 1977.

[20] A. Scrivener, "Means for shaping the operative surfaces of grinding wheels," November 1 1938. US Patent 2135202.

[21] N. R. Babu and V. Radhakrishnan, "Investigations on laser dressing of grinding wheels–Part II: Grinding performance of a laser dressed aluminum oxide wheel," *Journal of Engineering for Industry*, vol. 111, no. 3, pp. 253–261, 1989.

[22] V. Phanindranath and N. R. Babu, "A theoretical model for prediction of groove geometry on laser dressed grinding wheel surface," *International Journal of Machine Tools and Manufacture*, vol. 36, no. 1, pp. 1–16, 1996.

[23] K. Wegener, H.-W. Hoffmeister, B. Karpuschewski, F. Kuster, W.-C. Hahmann, and M. Rabiey, "Conditioning and monitoring of grinding wheels," *CIRP Annals – Manufacturing Technology*, vol. 60, no. 2, pp. 757 – 777, 2011.

[24] J.-S. Kwak and M.-K. Ha, "Force modeling and machining characteristics of the intermittent grinding wheels," *KSME International Journal*, vol. 15, no. 3, pp. 351–356, 2001.

[25] U. Köklü, "Grinding with helically grooved wheels," *Proceedings of the Institution of Mechanical Engineers, Part E: Journal of Process Mechanical Engineering*, vol. 228, no. 1, pp. 33–42, 2012.

[26] E. Uhlmann and L. Hochschild, "Tool optimization for high speed grinding," *Production Engineering*, vol. 7, no. 2, pp. 185–193, 2013.

[27] T. Waida, H. Noguchi, M. Rezaei, and T. Suto, "Creep feed grinding of ceramics and ceramic-matrix composites with slotted and perforated wheels," *Journal of the Japan Society of Precision Engineering*, vol. 57, no. 2, pp. 324–329, 1991.

[28] T. Waida, T. Suto, H. Noguchi, and H. Inoue, "Development of slotted & perforated wheels for creep feed grinding and their grinding performance," *Journal of the Japan Society of Precision Engineering*, vol. 57, no. 7, pp. 1223–1228, 1991.

[29] T. Nguyen and L. C. Zhang, "The coolant penetration in grinding with segmented wheels–Part 1: mechanism and comparison with conventional wheels," *International Journal of Machine Tools and Manufacture*, vol. 45, no. 1213, pp. 1412–1420, 2005.

[30] T. Nguyen and L. C. Zhang, "Modelling of the mist formation in a segmented grinding wheel system," *International Journal of Machine Tools and Manufacture*, vol. 45, no. 1, pp. 21–28, 2005.

[31] T. Nguyen and L. C. Zhang, "The coolant penetration in grinding with a segmented wheel–Part 2: Quantitative analysis," *International Journal of Machine Tools and Manufacture*, vol. 46, no. 2, pp. 114–121, 2006.

[32] T. Nguyen and L. C. Zhang, "Performance of a new segmented grinding wheel system," *International Journal of Machine Tools and Manufacture*, vol. 49, no. 34, pp. 291–296, 2009.

[33] H. E. Sherk, "Slotted abrasive wheel," August 4 1936. US Patent 2049874.

[34] Y. C. Fu, H. J. Xu, and J. H. Xu, "Optimization design of grinding wheel topography for high efficiency grinding," *Journal of Materials Processing Technology*, vol. 129, no. 13, pp. 118–122, 2002.

[35] A.-M. Mohamed, R. Bauer, and A. Warkentin, "Uncut chip thickness and coolant delivery effects on the performance of circumferentially grooved grinding wheels," *The International Journal of Advanced Manufacturing Technology*, vol. 85, no. 5–8, pp. 1429–1438, 2016.

[36] N. R. Babu, V. Radhakrishnan, and Y. V. G. S. Murti, "Investigations on laser dressing of grinding wheels–Part I: Preliminary study," *Journal of Engineering for Industry*, vol. 111, no. 3, pp. 244–252, 1989.

[37] T. Tawakoli and A. Daneshi, "New kinematic in dressing of grinding wheels," *ASME 2013 International Mechanical Engineering Congress and Exposition*, vol. 2B: Advanced Manufacturing, p. V02BT02A076, 2013.

[38] L. Trefethen and D. Bau, *Numerical Linear Algebra*. Society for Industrial and Applied Mathematics, 1997.

[39] C. Guo and S. Malkin, "Energy partition and cooling during grinding," *Journal of Manufacturing Processes*, vol. 2, no. 3, pp. 152–157, 2000.

[40] A.-M. O. Mohamed, A. Warkentin, and R. Bauer, "Variable heat flux in numerical simulation of grinding temperatures," *International Journal of Advanced Manufacturing Technology*, vol. 63, no. 5–8, pp. 549–554, 2012.

Appendix A

MATLAB Code

A.1 Kinematic Requirements Code

```
%% Header
% Groover Kinematic Simulator v1.5
% Cameron Forbrigger
% Last Edited: Jan. 28th, 2016
% Revision Notes
% - 1.4 Changed program to accept a given set of profile
   points.
%% Parameter Definition
clear variables
close all
% Groove design
% Groove width
b_g = 0.00108; %m
% Number of starts
S = 1;
% Groove lead
L = 0.005; %m/rev
% Process
% Wheel angular velocity
w_s = 150; %rpm
w_s = w_s/60*2*pi; %rad/s
% Wheel geometry
% Mean wheel diameter
d_s = 15; %in
d_s = d_s*0.0254; %m
```

```
% Wheel width
b_s = 1.0; %in
b_s = b_s*0.0254; %m
% Groove helix angle
alpha = atan(pi*d_s/L)*180/pi; %deg
% Wheel profile
% filename = 'datum.dat';
% [z,y] = import_dat_file(filename);
z = 0:0.000001:b_s;
% Sinusoid period
l = 0.0035; %m
% Sinusoid amplitude
h = 0.0017; %m
for i=1:size(z,2)
    if z(i) < b_s/2-l || z(i) > b_s/2+l
        y(i) = 0; %m
    else
        y(i) = -h*cos(2*pi*(z(i)-b_s/2)/l) + h; %m
    end
end
% Calculating the maximum slope of the profile
max_slope = 2*pi*h/l;
%y = -0.0017*cos(2*pi*z/0.0035)+0.0017;
r = y + d_s/2-mean(y); %m
%% Calculation
% Groove factor
gf = (1-b_g*S/L)*100;
% Wheel surface velocity as a function of z
v_s = w_s*r; %m/s
% Groover velocity in the z-direction
v_gz = L*w_s/(2*pi); %m/s
% Calculating time vector
```

```
t = z/v_gz; %s
% Groover velocity in the y-direction
v = (r(2:end)-r(1:end-1))./(t(2:end)-t(1:end-1)); %m/s
% Groover acceleration in the y-direction
a = (v(2:end)-v(1:end-1))./(t(2:end-1)-t(1:end-2)); %m/s^2
%% Plotting
% Wheel profile
figure()
plot(z*1000,y*1000)
xlabel('z (mm)')
ylabel('y (mm)')
title('Wheel Profile')
axis([0 b_s*1000 -b_s/2*1000 b_s/2*1000])
% Groover y-position vs. time
figure()
plot(t,y);
xlabel('t (s)');
ylabel('y (m)');
title('Groover Vertical Position vs. Time')
% Groover y-velocity vs. time
figure()
plot(t(1:end-1),v)
xlabel('t (s)');
ylabel('v_y (m/s)');
title('Groover Vertical Velocity vs. Time');
% Groover y-acceleration vs. time
figure()
plot(t(1:end-2),a);
xlabel('t (s)');
ylabel('a_y (m/s^2)')
title('Groover Vertical Acceleration vs. Time');
% Groover z-position vs. time
```

```
89
90 % Groover z-velocity vs. time
91 figure()
92 plot(t,v_gz);
93 xlabel('t [s]');
94 ylabel('v_z [m/s]');
95 title('Groover Horizontal Velocity vs. Time');
96 % Print results to command line
97 fprintf('                Groove factor:     %.1f %%\n',gf)
   ;
98 fprintf('    Maximum vertical velocity:     %.1f mm/s\n',
   max(abs(v))*1000);
99 fprintf('Maximum vertical acceleration:    %.1f mm/s^2\n',
   max(abs(a))*1000);
```

A.2 Forward and Inverse Kinematics Solver

```
1 function result = groover_kinematics(dir,varargin)
2 %groover_kinematics CUSTOM FUNCTION Calculate joint values
    given
3 %desired wheel geometry or calculate wheel geometry given
   joint values
4 %   C. Forbrigger, May 9th, 2017
5 %   Q = groover_kinematics('inverse',R_DS,R_S) returns the
    y-stage and
6 %   z-stage positions for the 2-axis groover, Q, given a
   set of cylindrical
7 %   coordinates from the grinding wheel center, R_DS, and
   the radius of the
8 %   grinding wheel, R_S.
9 %
```

```
10 %   The desired cylindrical coordinates should be given as a 3x1 vector of
11 %   the form R_DS = [rho;phi;z] in units of [inches; radians;inches] or a
12 %   matrix composed of 3x1 column vectors. The wheel radius R_S should
13 %   given as a scalar value in inches.
14 %
15 %   The function will return the desired y-stage and z-stage positions as a
16 %   2x1 vector Q = [YC;ZC], in inches, or a matrix of 2x1 column vectos.
17 %   The stage positions are given starting from a workpiece zero at the
18 %   bottom-dead-centre, front wheel face of the grinding wheel.
19 %
20 %   Q = groover_kinematics('inverse',R_DS,R_S,R_N) incorporates dressing
21 %   tool nose radius compensation for a given nose radius in inches, R_N,
22 %   using forward, backward and middle difference equations to calculate
23 %   the slope between the coordinates given when R_DS is a matrix. If R_DS
24 %   is a vector, the function assumes the slope is zero.
25 %
26 %   R_TS = groover_kinematics('forward',Q,R_S) returns the tool position in
27 %   cylindrical coordinates from the grinding wheel center, R_TS, given the
```

```
28 %   y-stage and z-stage positions of the 2-axis groover,
   and the radius of
29 %   the grinding wheel.
30 %
31 %   R_TS = groover_kinematics('forward',Q,R_S,R_N)
   incorporates dressing
32 %   tool nose radius compensation for a given nose radius
   in inches, R_N,
33 %   using forward, backward and middle difference
   equations to calculate
34 %   the slope between the coordinates given when Q is a
   matrix. If Q
35 %   is a vector, the function assumes the slope is zero.
36
37 % Unit vector describing the direction of Axis #1 (z-axis)
38 w_hat = [-0.0205
39           0.0018
40           0.9998];
41 % Unit vector describing the direction of Axis #2 (y-axis)
42 v_hat = [-0.0045
43           1.0000
44          -0.0012];
45 % Basis for the planar workspace
46 B = [v_hat w_hat];
47 % Normal vector to basis
48 n = cross(v_hat,w_hat);
49
50 switch dir
51     case 'forward'
52         q = varargin{1};
53         r_s = varargin{2};
54         r_t = B*q;
```

```
55          r_ts = cart2cyl_groover(r_t,r_s);
56          % Check if nose radius is given
57          if nargin > 3
58              r_n = varargin{3};
59              q_d = varargin{4};
60              r_d = B*q_d;
61              r_ds = cart2cyl_groover(r_d,r_s);
62              if size(r_ts,2) > 1
63                  % Initializing the y_m and z_m
                        compensation vectors
64                  y_m = zeros(1,size(r_ts,2));
65                  z_m = y_m;
66                  % Calculating the first slope with a
                        forward-difference approx.
67                  m = (r_ds(1,2) - r_ds(1,1))/(r_ds(3,2) -
                        r_ds(3,1)); %[in/in]
68                  % Calculating the dressing tool shape in
                        rotated
69                  % coordinates
70                  r_n_prime = (1/sqrt(m^2+1))*[1 m;-m 1]*r_n
                        ;
71                  % Finding the largest value of y'
72                  [~,I] = max(r_n_prime(1,:));
73                  y_m(1) = r_n(1,I);
74                  z_m(1) = r_n(2,I);
75                  for i = 2:size(r_ds,2)
76                      % Calculating interior slopes with
                            backward-difference approx.
77                      m = (r_ds(1,i) - r_ds(1,i-1))/(r_ds(3,
                            i) - r_ds(3,i-1)); %[in/in]
78                      % Calculating the dressing tool shape
                            in rotated
```

```
79                      % coordinates
80                      r_n_prime = (1/sqrt(m^2+1))*[1 m;-m
                           1]*r_n;
81                      % Finding the largest value of y'
82                      [~,I] = max(r_n_prime(1,:));
83                      y_m(i) = r_n(1,I);
84                      z_m(i) = r_n(2,I);
85                  end
86                  % Subtracting tool radius compensation
                       from the measured coordinates
87                  r_ts(1,:) = r_ts(1,:) - y_m;
88                  r_ts(3,:) = r_ts(3,:) + z_m;
89              end
90          end
91          result = r_ts;
92      case 'inverse'
93          r_ds = varargin{1};
94          r_s = varargin{2};
95          % Tool radius compensation
96          % Check if nose radius is given
97          if nargin == 4
98              r_n = varargin{3};
99              if size(r_ds,2) > 1
100                 % Initializing the y_m and z_m
                       compensation vectors
101                 y_m = zeros(1,size(r_ds,2));
102                 z_m = y_m;
103                 % Calculating the first slope with a
                       forward-difference approx.
104                 m = (r_ds(1,2) - r_ds(1,1))/(r_ds(3,2) -
                       r_ds(3,1)); %[in/in]
```

```
105                 % Calculating the dressing tool shape in
                        rotated
106                 % coordinates
107                 r_n_prime = (1/sqrt(m^2+1))*[1 m;-m 1]*r_n
                        ;
108                 % Finding the largest value of y'
109                 [~,I] = max(r_n_prime(1,:));
110                 y_m(1) = r_n(1,I);
111                 z_m(1) = r_n(2,I);
112                 for i = 2:size(r_ds,2)
113                     % Calculating interior slopes with
                            backward-difference approx.
114                     m = (r_ds(1,i) - r_ds(1,i-1))/(r_ds(3,
                            i) - r_ds(3,i-1)); %[in/in]
115                     % Calculating the dressing tool shape
                            in rotated
116                     % coordinates
117                     r_n_prime = (1/sqrt(m^2+1))*[1 m;-m
                            1]*r_n;
118                     % Finding the largest value of y'
119                     [~,I] = max(r_n_prime(1,:));
120                     y_m(i) = r_n(1,I);
121                     z_m(i) = r_n(2,I);
122                 end
123                 % Adding tool radius compensation to the
                        target coordinates
124                 r_ds(1,:) = r_ds(1,:) + y_m;
125                 r_ds(3,:) = r_ds(3,:) - z_m;
126             end
127         end
128         % Calculating reachable positions near the desired
                positions using the
```

```
129         % small angle approximations for sin and cos
130         % sinx ~ x       cosx ~ 1 - 0.5*x^2
131         sig = sqrt((n(1)/n(2))^2 - 2*r_ds(3,:)./r_ds(1,:)
               *(n(3)/n(2)) + 2*(r_s-r_ds(1,:))./r_ds(1,:));
132         phi_t = -n(1)/n(2) + sign(n(1)/n(2))*sig; % [rad]
133         r_ts = [r_ds(1,:);phi_t;r_ds(3,:)];
134         % Calculating reachable positions in cartesian
               coords
135         r_t = cyl2cart_groover(r_ts,r_s); %[in]
136         % Calculating the necessary stage targets using
               the Moore-Penrose
137         % Pseudoinverse of the workspace basis
138         q = B'*B\B'*r_t; %[in]
139         % Return q
140         result = q;
141     otherwise
142         error('Specify direction for groover_kinematics (
               type "help groover_kinematics" for more info)')
               ;
143 end
144
145 end
```